An Improved 2DOF Elastokinematic Surrogate Model for Continuous Motion Prediction and Visualisation of Forearm Pro-and Supination for Surgical Planning

Von der Fakultät für Ingenieurwissenschaften,
Abteilung Maschinenbau und Verfahrenstechnik der
Universität Duisburg-Essen
zur Erlangung des akademischen Grades
einer
Doktorin der Ingenieurwissenschaften
Dr.-Ing.

genehmigte Dissertation

von
Jing Xu
aus
Beijing, China

Gutachter: Prof. Dr.-Ing. Andres Kecskeméthy
Gutachterin: Prof. Dr. med. Annelie Weinberg
Gutachter: Prof. Dr.-Ing. Wojciech Kowalczyk

Tag der Mündlichen Prüfung: 28.Feb.2013

Abstract

Forearm rotation (pro-/supination) involves a non-trivial combination of rotation and translation of two bones, namely, radius and ulna, relatively to each other. Early works regarded this relative motion as a rotation about a fixed (skew) axis. However, this assumption turns out not to be exact. This thesis regards a spatial-loop surrogate mechanism involving two degrees of freedom with an elastic coupling for better forearm motion prediction. In addition, the influence of the bone morphology and position of elbow on kinematics are also considered. The model parameters are not measured directly from the anatomical components, but are fitted by reducing the errors between predicted and measured values in an optimization loop. For non-invasive measurement of bone position, magnetic resonance imaging (MRI) is employed. We present a method to self-calibrate the arm position in the MRI scanning tube and to fit the model parameters from a few, coarse MRI scans. Results show a good concordance between measurement and simulation. Moreover, the minimum distance changing between bones during forearm rotation is elucidated, which is not yet proved in anatomical and clinical literatures. The minimum distance is calculated by searching for the global shortest distance between bone contours on ulna and radius by a two-level selection and a following multidimensional Newton-Raphson algorithm. To this end, the methodology is extended from healthy bones to deformed arms and an angulated forearm model is developed. The 3D angulated bone geometry is obtained by manually separating the bone structure at the broken position, and the minimum distance and the range of motion of fractured forearms are analyzed. As shown for a single case validation, simulated results show very small deviations from anatomical data. Furthermore, the simulations discussed above are visualized using interactive interfaces, which facilitates the application of the model in clinical planning.

Zusammenfassung

Die Unterarmrotation beinhaltet eine nicht triviale Kombination einer Rotation und Translokation zweier Knochen, Radius und Ulna relativ zu einander. Frühere Arbeiten betrachteten diese relative Bewegung als eine Rotation um eine fixierte Achse. Allerdings scheint diese Annahme ungenau zu sein. Diese Arbeit betrachtet ein Spatial-Loop Surrogat Mechanismus unter Berücksichtigung von zwei Freiheitsgraden mit einer elastischen Gelenkverbindung für eine bessere Prognose der Unterarm-Bewegung. Zusätzlich wird der Einfluss der Knochenmorphologie und die Position des Ellenbogens auf die Kinematik berücksichtig. Die Modellparameter werden nicht direkt von den anatomischen Komponenten bestimmt, sondern unter Berücksichtigung der Abweichung von Annahme und Messung. Zur nicht invasiven Messung der Knochenposition wird die Methode der Magnetresonanztomographie (MRT) angewendet. Wir stellen hier eine Methode um die Arm-Position in das MRI Scan-Rohr selbst zu kalibrieren und die Modellparameter aus einige grobe MRT-Aufnahmen zu passen. Die simulierten Ergebnisse zeigen sehr kleine Abweichungen von anatomischen Daten. Eine minimale Änderung der Distanz zwischen den Knochen während der Unterarmrotation wird beleuchte, die bisher nicht in der anatomischen und klinischen Literatur beschrieben ist. Die Berechnung der minimalen Distanz erfolgt über die Ermittlung der gesamt kürzesten Distanz. Zu diesem Zweck wird die Methodik von gesunden Knochen auf deformiere Arme und ein angewinkeltes Unterarmmodel entwickelt. Die 3D gewinkelte Knochen-Geometrie ergibt sich aus der Knochenstruktur an der gebrochener Position manuell zu trennen, und darauf werden der Mindestabstand und der Bereich der Bewegung von dem gebrochenen Unterarm analysiert. Wie dies bei einer einzelnen Fall Validierung, zeigen die simulierten Ergebnisse sehr kleine Abweichungen von anatomischen Daten. Darüber hinaus werden die oben beschrieben Simulationen mit interaktiven Benutzeroberflächen visualisiert, welche die Anwendung des Modells in der klinischen Planung erleichtert.

Danksagung

Die vorliegende Arbeit entstand während meiner Zeit als Doktorandin am Lehrstuhl für Mechanik und Robotik für Ingenieurswissenschaften der Universität Duisburg-Essen. Ich danke all jenen, die zur Entstehung dieser Arbeit beigetragen haben.

Zunächst möchte ich Herrn Professor Andrés Kecskeméthy, Leiter des Lehrstuhls für Mechanik und Robotik an der Universität Duisburg-Essen für seine hervorragende Betreuung und die Übernahme des Referats der vorliegenden Arbeit danken. Ohne seinen fachlichen Rat, welchen ich in jeder Situation suchen konnte, wäre diese Arbeit nicht möglich gewesen.

Mein Dank gebührt ebenfalls Frau Prof. Dr. med. Annelie Weinberg sowie Herrn Prof. Dr.-Ing. Wojciech Kowalczyk für die Übernahme der Gutachten und für die erteilten wertvollen Ratschläge in der Vervollständigung dieser Arbeit.

Des weiteren danke ich allen meinen Kolleginnen und Kollegen des Lehrstuhls für Mechanik und Robotik für die gute und freundschaftliche Zusammenarbeit. Insbesondere den Kollegen M. Tändl und F. Geu für die freundliche Aufnahme in ihren Kreis und den fachlichen Austausch.

Abschließend danke ich meiner Familie und meinen Freunden, die stets an das Gelingen der Arbeit geglaubt haben und mich in allen Phasen unterstützt haben.

Vielen Dank euch allen!

Contents

List of Figures

List of Tables

Chapter 1

Introduction

Lately the number of surgical operations is growing rapidly and the quality of the standards is being improved as well. The demand for a tool to help surgeons and prosthesis designers to optimize their actions, enhance rehabilitative techniques and minimize the treatment risks for patients, is progressively increasing [1], [2]. Consequently, as effective methods to predict the effect of the medical treatment, computer simulations and physical devices are being used more and more often in diagnosis [3], [4]. With the growth of the forearm fracture treatment in modern surgical treatment, many computer-aided biomechanical investigation have been developed in the last years to understand the axial rotation of the forearm, i.e. the motion of forearm from supination (palm up) to pronation (palm down).

1.1 Problem statement

The forearm is the distal region of the upper limb, between the elbow and the wrist. It includes two bones, ulna and radius. The forearm motion is a complex movement, in which the radius, the ulna, the distal and proximal radioulnar joint, the interosseous membrane and the forearm rotator muscles are all involved. The rotational motion brings the hand from the position of supination to pronation around the longitudinal axis, and vice versa. This investigation on the forearm movement is particularly interesting because it is a key functional motion of the upper extremity in the daily life, such as turning a door handle, and also due to the growing need of surgical treatment on forearm fracture in last years.

The benchmark procedure for the treatment of forearm fractures in adults is via open reduction in order to prevent malunion, but it is with the risk of postoperative infection, non-union, delayed union, or failure of fixation. In children the treatment is often by closed reduction and immobilization due to the fact that their bone healings in less than anatomic position are still compatible with later unrestricted function as the result of their corrective potentials during skeletal growth. The maximum acceptable displacement in children depends on the age, the fracture level, and the type of displacement and remains controversial [5], [6]. Of course the unstable fracture by children is also necessary to be treated surgically.

The criteria to evaluate the degree of success in the treatment mainly refer to: (1) union of the fracture, and (2) restoration of function. As has been demonstraed by cadaver and retrospective studies, the function loss in pronation or supination results from the axial or rotational misalignment or encroachment of the interosseous space.

Currently the contralateral healthy side is used as a reference in the clinical treatment, but it is not satisfying due to the existence of side to side variability in the healthy population [7], [8]. Since computer-based planning is not essentially dependent on the healthy side, it is attracting a great clinical interest with the effort to improve the surgical reliability and the outcome [9]. In the forearm clinical treatment, such kind of computer-aided simulation could help to predict on the correlation of the degree of possible misalignment between the bone fragment axes after healing to pro-/supination function limitations. Thus, it would be a powerful tool to help decide whether a corrective surgery is required. In case the correction is necessary, it would give a clue on how to minimize the correction in order to reduce the risk of the occurrence of impairment of function as much as possible. Therefore, doctors, technicians and biomechanics are demanding the computer-aided tool to assist them planning the treatment and predicting the consequence even prior to the treatment.

Since even small positioning errors, misalignments or misfits can result in the failure of the treatment, the accuracy of the computer-aided modeling is very critical. There exists substantial research concerning the significance of accuracy of human upper limb modeling on the prediction of the success of prosthetic device or the protocols of rehabilitations [1], [2], [10]. In biomechanics, an optimal model for developing an accurate computer-aided tool for forearm treatment shall include all the elements and the interrelationship among bones, joints and ligaments. It is capable as well to reduce the interrelationship to a few characteristic motion quantities and thus simulate the motion sufficiently and precisely.

1.2 State of art

In last decade much research has been done to understand the human forearm mobility and to simulate the pro- and supination motion in both normal and abnormal motion.

Forearm kinematics has been studied in various settings from in vitro to in vivo. Fick proposed the first kinematic model in 1904. In this model he described the forearm motion in a way that the forearm rotated around the ulna as a constant axis of rotation [11] (Fig. 2.10a). As a quite simplified model it has an unrealistic strong tilting at the maximal pronation (Fig. 2.10b).

In the following work, the mechanical axis of the forearm has been investigated by using mechanical axis locaters [12], radiography [13], sonic digitzers [14], computed tomography (CT) [15], and magnetic resonance imaging [13]. Hollister et al. described a fixed axis extending from the center of the radial head proximally to the ulnar styloid distally [12]. Youm et al. also noted a single axis that extended from the center of the capitellum to the distal ulna [14]. Hagert showed a single axis extending from the center of the radial head to the center of the ulnar head distally [16]. Robbin reported in a study that the axis of rotation is a variable screw axis [17]. All the above studies indicate that axis of rotation of the ulna changes its position during forearm pro- and supination motion, and thus that forearm motion cannot be recognized as a simple rotation about a fixed axis. The reason for the discrepancy is that most of the previous studies are performed in-vitro, which makes the investigations lacking of physiological muscle loading, passive simulation of forearm rotation, and artificial fixation of the ulna. The argument is that absence of these parameters may very possibly lead to deviations [18].

More comprehensive kinematic models including ulna's motion were developed recently based on MRI technology. Kapandji [19], Nakamura et al. [20], [21], and Weinberg [22] revealed the forearm rotational motion is not around a constant axis, but is a complex motion comprising rotation and translation of radius relative to ulna. Due to this effect, the carpus is allowed to remain perpendicular to the forearm. Fig. 2.10c depicts the evasive and lateral swaying motion of ulna, which ensures the parallelism of the hand to the elbow.

A surrogate mechanism was presented by Kasten and Weinberg et al. for the pro- and supination. In this mechanism the joints were considered by a simplified mechanical analogy [3], [23]. They fitted the kinematics to the patient-specific anatomy by manually measuring geometric properties from radiographs, e.g. bone lengths.

In a later study Kecskeméthy and Weinberg introduced a two-degree-freedom surrogate mechanism into model mentioned above. This updated model contains virtual springs to incorporate elastic components, for instance ligaments [24]. It is featured by an elastokinematic coupling between axial displacement and lateral swaying of the humero-ulna (elbow) articulation. The lateral swaying motion predicted by this model has been proved [25]. Recently this mechanism is being applied in investigations including the design of external surrogate mechanism [26], simulation of forearm motion for pre-operative planning [27], [28], trajectory generation of CPM device to control forearm pro-/supination [29] and elbow joint [30] for post-operative treatment, and development of robot-assisted hand rehabilitation [31], [32].

Concerning on the absence of physiological parameters, complex musculoskeletal models of the upper limb have been developed. In these models soft tissues were simulated [33] [34]. However, the usability of these models is limited by their inherent insufficiencies: the swaying angle of the ulna was neglected in the simulation of the pro-/supination [34]; patient-specific anatomy cannot easily be incorporated in [33].

The other series of work are dedicated to the shape analysis. Burdin et al. investigated a collision technique which can be used to deduce the influence of the bone morphology on the magnitude of the pro- and supination motion [35]. Fürnstahl et al. introduced a motion model of the forearm which was based on a patient's joint morphology. He presented the morphology of the articulations by 3-dimensional splines and expressed the gliding motion in the distal radioulnar joint and the evasive ulna movement in a closed-form [28].

With the development of 3D (three-dimensional) CT registration techniques, several studies based on these techniques have been recently performed. Tay et al. found the proximal-distal translation of the radius with respect to the ulna during the forearm rotation, and proposed that distal forearm kinematics may be affected by the position of elbow [36]. Fu et al. verified that the influence of elbow position on the kinematics of the distal radioular joint (DRUJ), which is predominately affected by the forearm motion and secondarily by the elbow flexion [37]. Kim et al. studied the congruency index of proximal radioulna joint (PRUJ) in vivo and the translation motion of the radial head with regard to the lesser sigmoid notch with forearm rotation. He verified that PRUJ congruency changed during forearm rotation [4].

In addition, some investigations focused on the dynamics change in the shape of IOM and also on the quantification of the distance change during the forearm rotation [13], [38]. Marai et al. introduced a modeling method to determine bony contact areas and ligaments paths in articulation. In this method, bones are modeled both implicitly (scalar distance field) and parametrically (manifold surface). Thus inter-bone distances are computed by this double representation [39].

Furthermore, limitation of the range of forearm pronation-/supination is a topic that is often encountered in the treatment of forearm bones' fractures. It was shown in cadaver and retrospective studies that the direction and magnitude of the angulation, as well as narrowing of the interosseous space between the radius and ulna, can affect the forearm function significantly. Tarr et al. researched the limitation of forearm rotation caused by angular deformity of forearm bones. A cadaver study showed that the soft-tissue tension, especially of the IOM, rather than impingement between the forearm bones limited the rotation of the forearm [5]. In another report, Yasutomi et al. presented the correlation between the positions of pronation-/supination axis and narrowing of the interosseous space [40]. Later on, Kasten et al. developed a computer program based on angular deformities, for the simulation of forearm rotation and the prediction of impairment [3]. However, the real bone geometry was not taken into account in this model.

1.3 Objective

Based on an elasto-kinematic forearm model proposed by Kecskeméthy and Weinberg [24], the primary objective of this thesis is to develop a method to automatically determine the model parameters as well as the relative location of the bone geometry with respect to the links in the mechanism. The model parameters will be fitted by searching for the minimum error between predicted and measured values (MRI) by an optimization routine. The influence of the bone morphology, as well as the position of elbow on the kinematics will be also considered. After the fitting process, the accuracy of the simulation will be evaluated.

Based on this automatic determination of the model parameters, a 3D visualized user-friendly interface will be developed with the multi-body programming library MOBILE . Thus, the interactive window could facilitate the application of the model in medical training and surgical treatments.

Another objective of this thesis is to elucidate the minimum distance changes taking place during forearm rotation, which is not yet proved in anatomical and clinical literatures. During the forearm rotation, the value and location of the minimum distance between these two forearm bones actually varies at different cross-section levels as well as different pro-/supination angles. The methods for this investigation in 2D model (MRI slice) and 3D model (rotating bones) will be established, and results will be analyzed.

Moreover, in this thesis, the mechanism will be extended to the deformed forearm. Several examples will be analyzed based on the data from a literature, since there no testers available with bone fractures. The value and location of the minimum distance change between bones and the maximum pronation angle of the forearm deformity will be evaluated. A good preliminary result will enlighten the potential application of the fractured mechanism in the prediction of the impairment of function, and the need for a more detailed investigation in the future.

The present work validates the theoretical derivations on a single subject only. Future work may be devoted at generalizing the findings to larger subject sets, which is however out of the scope of this thesis.

1.4 Outline

The outline of this work is as following:

Chapter **1** states the reason why the computer-based simulation of forearm motion is becoming more and more important, and chronically describes the works which have been done on the forearm motion modeling.

Chapter **2** details the basic anatomic units in the arm that are involved in the pro- and supination, and describes the 2DOF surrogate mechanism employed in this study. The modeling conditions, e.g. coordinate, environment and used classes, are also introduced in detail.

Chapter **3** starts from the description of the MRI measurements which are the databases for the studies. Two kinds of MRI measurements are performed: fine static scans and dynamic motion scans, at 5 rotational angles, 3 torque conditions and series of cross-section levels, respectively. A semi-automatic segmentation algorithm is then used to gain the three-dimensional bone geometry, based on which the distribution of the bone centroid line is determined. In the next step, following the described fitting principles, model parameters are then optimized by the fitting process which includes a self-calibration process to determine the arm position in the MRI scanning tubes. Thereafter, the results computed by using this model are compared with the measured values, in order to evaluate the simulation accuracies. The simulation model is visualized at the interface of object-oriented multibody program library MOBILE. To the end, the results obtained from the 2DOF mechanism is compared with those from a fixed-axis mechanism.

Chapter **4** explains how the minimum distance between forearm bones is calculated. In 2D model (MRI slices) forearm bones are recognized as series of bone contours with B-Spline curves. The point cloud of bone contour is fitted with a smooth and continuous spline curve and the minimum distance between two spline curves is computed by an algorithm with two selection levels. In the next step, the calculation is extended to a 3D model (two rotating forearm bones in space) with regarding the surfaces of forearm bones as series of parallel segment lines, and the distance changing is presented as a function of the pro-/supination angle. At last, the results are analyzed and compared with clinical knowledge.

Chapter **5** extends the distance calculation described in Chapter **4** to fractured forearms. A broken forearm model is developed based on the aforementioned 2DOF kinematic mechanism. To predict the range of motion by forearm impairment, the maximal pronation angle is separately analyzed by two different methods: (1) calculating the minimal distance between the vectors that represent bone ulna and radius in the angulated kinematic model; (2) calculating the minimal distance between the surfaces of two bones ulna and radius in the model. Both results are analyzed and compared to literature data.

Chapter **6** summarizes the results in this work and suggests possible topics of future research.

Chapter 2

Design of Elastokinematic Surrogate Mechanism

In this chapter, the basic biomechanical properties of the human forearm structure and the 2DOF surrogate forearm mechanism are described.

2.1 Basic functional properties of pro- and supination

The human arm is constituted by the humerus bone and the forearm bones which consist of the radius and the ulna. The elbow joint is the connecting articulation between the humerus and forearm bones. The wrist is constituted by metacarpal bones. The carpals form the hand, and the phalanges form the fingers and thumbs. A diagram of human arm bones is shown in Fig. 2.1.

Bone ulna and radius

As the constituents of the forearm, bone ulna and radius are coupled at two ends, resembling a parallel mechanism. As in Fig. 2.2, the proximal ends are jointed to the humerus at the elbow by the radial head (a spherical pit rotation on a spherical condyle of the humerus) and trochlear notch of the ulna (a rotation about the elbox axis due to the clamped shape). The other end connected to the wrist by a radio-ulnar joint enables a sliding and rotating relative motion. The bones are firmly bonded together at the joints by ligaments, with the assistance of the stress from the membrane interossea,. The rotation of the hand about the longitudinal axis brings the hand from supination (palm up) to pronation (palm down) and vice versa.

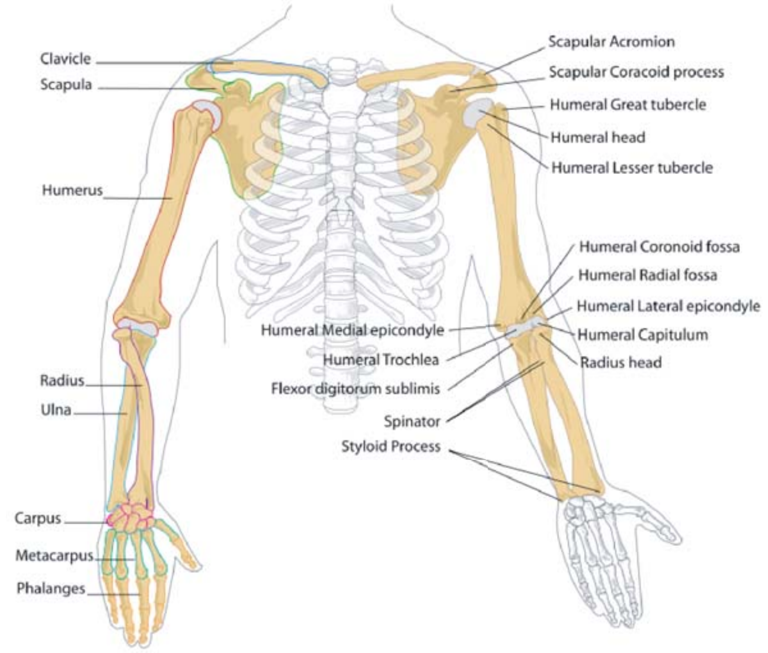

Fig. 2.1: Diagram of human arm bones.

Bone ulna is at the side of foream adjacent to the body in the anatomical position while the palm of the hand facing forward. Structurally it is prism-shaped, and with a broader proximal side and a narrower distal side. Proximally, there are an olecranon process and a structure looking like a hook, which fits into the olecranon fossa of the humerus, forming a hinge point with the trochlea of the humerus. This construction helps to prevent the hyperextension. The distal end has a styloid process. Functionally the ulna can support the forearm and allow its motion, and in addition it is also the support for many muscles and ligaments. For example, the muscles attached to the ulna contain the pronator teres muscle, the flexor digitorum superficialis muscle, triceps brachii muscle, supinator muscle and pronator quadratus muscle etc [41].

Bone radius is located from the lateral side of the elbow to the thumb side of the wrist in the anatomical position, functioning as an articulation with the capitulum of the humerus, the radial notch and the head of the ulna. Structurally it is of prismatic form and slightly curved in the longitudinal direction, parallel to the ulna, but shorter and smaller compared to the latter. It consists of a body and two extremities. There is a cylindrical head at the upper extremity which is the site to articulate with the humerus and the ulna, a neck and a double tuberosity. The somehow quadrilateral shaped lower extremity of the radius renders the articular site for the ulna, scaphoid and lunate bones. The distal end of bone radius forms a palpable point, named the styloid process. Many muscles are attached to bone radius, e.g. the biceps, supinator, flexor digitorum superficialis etc [41].

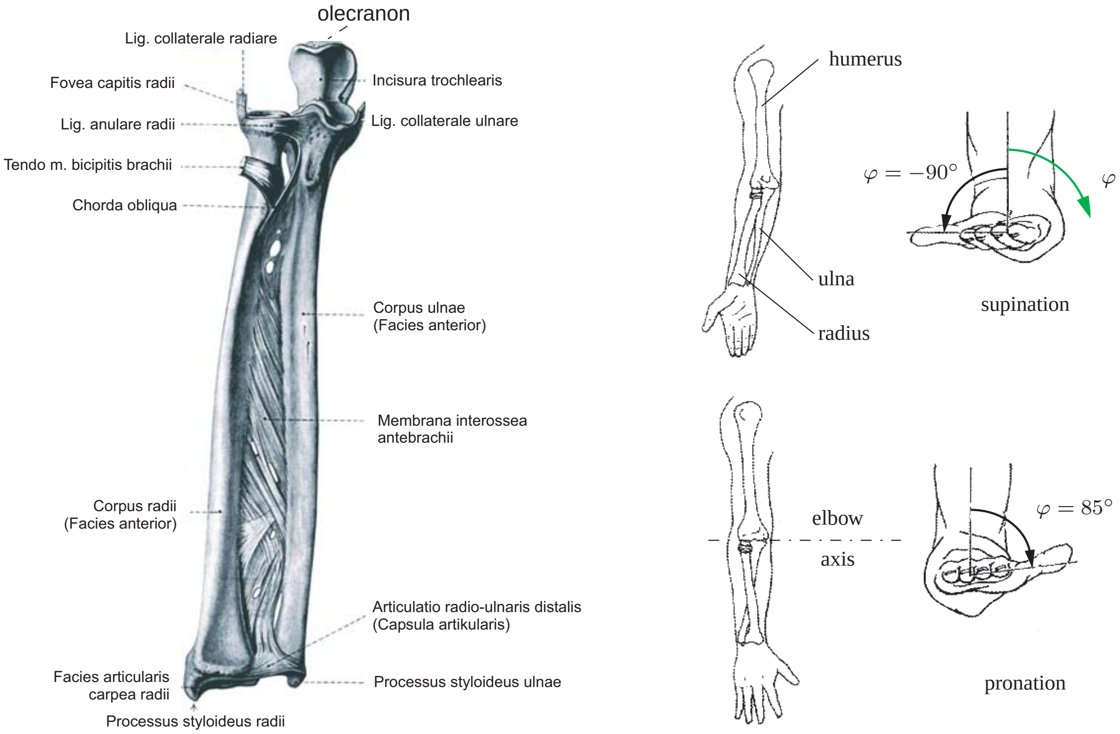

Fig. 2.2: Anatomy of forearm bones (adapted from Rauber [42] and Kapandji [19]).

Ligaments

Also known as articular ligaments, the ligaments are fibrous tissues to connect bones and thus to stabilize them. The ligament of the forearm is called the interosseous membrane, which is strong and flexible. The interosseous membrane consists of the central band, accessory bands and proximal interosseous bands. Functionally it connects the radius and the ulna along their length, and thus increases the stability between the two bones, but also allows for the twisting of the forearm. Along the motion of forearm from pronation to neutral and to supination position, the interosseous membrane fibers change from a relaxed state, to a tense state, and then become relaxed again in a respective sequence. Furthermore, the interosseous membrane is the support for the attachment of muscles, through which forces could be transmitted from the radius, to the ulna, to the humerus.

Articulation

The trochlea of the humerus fitting into the trochlear notch of the ulna forms the humeroulnar joint, and the capitulum of the humerus articulating with the fovea on the head of the radius forms the humeroradial joint. The articulation of the radius and ulna with each other at their proximal and distal ends at synovial joint are termed as the proximal and distal radioulnar joints, that enable the pronation and supination. At the location of the proximal articulation, the radial head is kept in the position of the radial notch of the ulna by the strong annular ligament that is a fibrous collar in a U shape and is attached to the anterior and posterior margins of the radial notch. At the location of distal articulation, the rounded side of the head of the ulna articulates with the ulna notch at the distal end of the radius by a fibrocartilage articular disc.

Range of motion

The active range of motion (ROM) of the forearm is usually taken as 85° in supination and 75° in pronation while the elbow is flexed at 90° (Fig. 2.3). In the figure, the shaded region represents the range sufficient for most activities of daily living, such as eating, using a telephone [42]. A loss of up to 20°is usually considered acceptable, either at supination or at pronation. The active ROM can be different among patient groups to be examined, and it is also dependent on demographics and laxity of the joint and its surrounding tissues. In 1979 Boone and Azen have measured a mean value of 82.1±2.8° for supination and 75.8±5.1° for pronation with the neutral being with the forearm in mid-position [43]. Some other reported data are listed in Table 2.1.

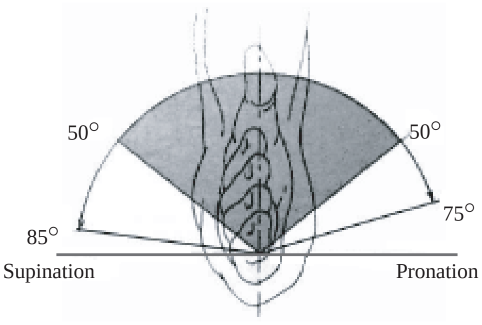

Fig. 2.3: Normal range of forearm rotation.

Table 2.1: Reported range of supination and pronation of the forearm

	Supination (°)	Pronation (°)
Dempster (1955) [44]	113	77
Schnelle (1964)	70-85	60-80
Nakamura et al. (1999) [20]	75-97	62-103
Weinberg et al. (2000) [22]	79-90	60-74

When the radius and ulna are not injured, the adjacent soft tissue is not compromised in the forearm rotation and the muscles between tissues operate at their optimum scale. In case of mal-union and rotational mal-aligned forearm fractures, the curvature of the radius is deteriorated. Consequently, there is a reduction of the interosseous space between the radius and ulna which leads to a limited ROM.

2.2 Forearm surrogate mechanism model

2.2.1 Classic forearm model

There are two basic assumptions in the classic forearm model regarding the motion of the forearm bones related to humerus: (1) the radius head's surface is sufficiently concave and cup-shaped to articulate with the corresponding spherical surface of the capitulum of the humerus, which allows a fixed-point rotation of the radius; (2) the ulna has proximally an olecranon process with a hook-like structure that fits into the olecranon fossa of the humerus, functioning as a hinge joint that allows only a rotation about the elbow axis. In other words, the motion of ulna is presumed to be held with respect to the humerus during pro- and supination in the classical model.

In this model, the relative motion between bone ulna and radius is simplified by regarding the proximal and distal radioulnar as spherical articulations, due to the correspondingly shaped contact surfaces [11] (Fig. 2.4). Herewith, the proximal articulation between the radial head and the sigmoid fossa of ulna is achieved by compelling the ends of radius and ulna together through the annular ligament and the ligament of denuce, while the distal articulation between the radial notch and the ulna head is bounded by the triangular ligaments, volar radioulnar ligament and dorsal radioulnar ligament. Furthermore, both bones are held together by a cross-fibered membrane called the membrana interossea antebracii, which joins the medial border of the radius to the lateral border of the ulna. Therefore, the pro- and supination motion in the classic model is defined as a fixed ulna and a pure rotation of the radius around a fixed axis. The axis is a straight line going through the two centers of the spherical articulations which model the proximal and distal radioulnar joints (Fig. 2.9a and Fig. 2.10a).

The derived mechanism based on this classical model can be illustrated as the diagram in Fig. 2.5. The vectors $\underline{r}_1$ and $\underline{r}_3$ represent the bony axis of the ulna and the radius, and the vectors $\underline{r}_2$ and $\underline{r}_4$ represent the hand and the elbow, respectively. S_1 and S_2 are the spherical joints representing the contact location at proximal and distal radioulnar articulations.

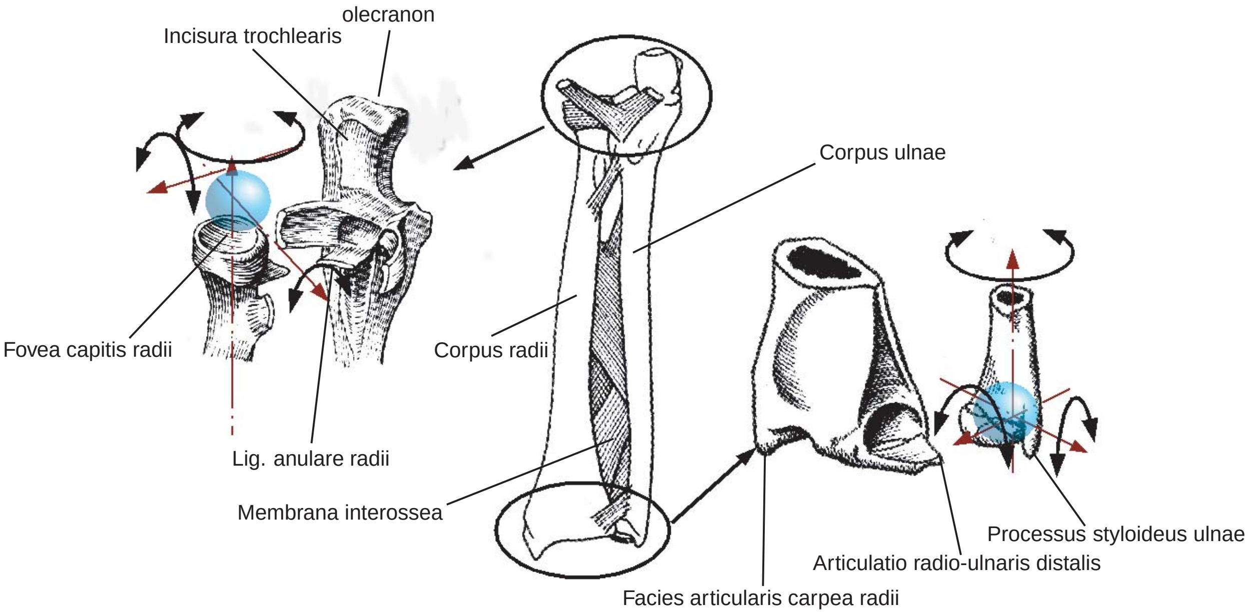

Fig. 2.4: Basic modeling of relative motion between ulna and radius.

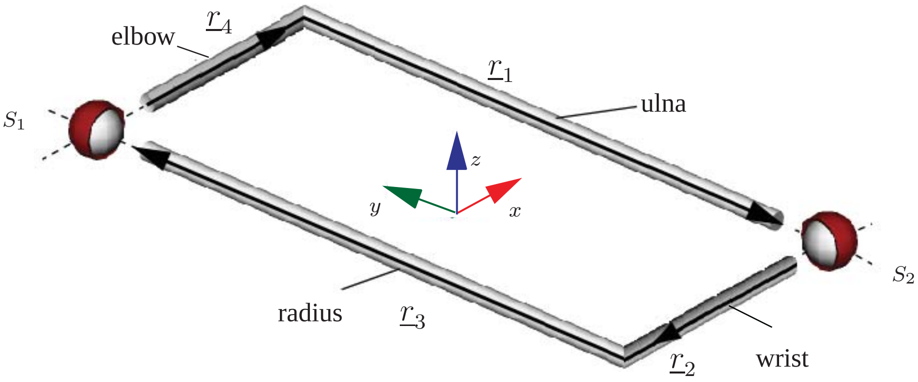

Fig. 2.5: Fick's fixed-axis forearm model.

2.2.2 Forearm kinematic surrogate mechanicsm with 1DOF

During the improvement of the above-mentioned classic model, more comprehensive kinematic models were developed which take the motion of the ulna bone into consideration [20], [23]. Weinberg et al. introduced a surrogate mechanism with one degree of freedom (1DOF) for the pro-/supination. In this mechanism, the effect of joints on the motion were considered by a simplified mechanical analogy. As shown in Fig. 2.6, it is a quadruple linked mechanism. The vectors $\underline{r}_1$ and $\underline{r}_3$ represent the bony axis of the ulna and the radius. And the vectors $\underline{r}_2$ and $\underline{r}_4$ represent the distal and proximal radioulnar articulations, respectively. Vector $\underline{r}_5$ represents the shifting of the ulna in the linear splint.

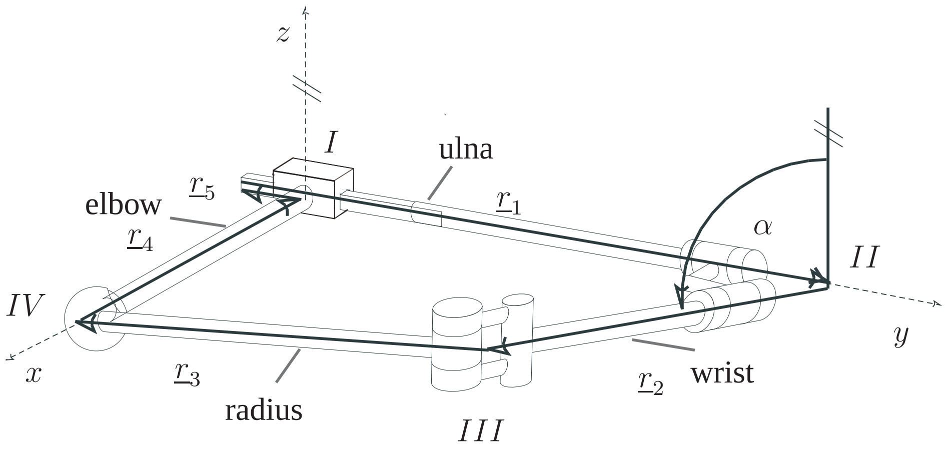

Fig. 2.6: One-degree-of-freedom surrogate mechanism for pro- and supination.

In addition, there are four theoretical joints in this mechanism to reflect the actual motion of supination and pronation. The theoretical joints (I) and (IV) represent the elbow anatomically. The linear prismatic joint (I) is for the translational evasive movement of the ulna. Although this joint cannot exactly reflect the evasive motion of the ulna, it fairly approaches the real movement to a high level. The spherical joint (IV) is used to produce the proximal contact of the ulna and radius. Joints (II) and (III) correspond to the distal radioulnar and radiocarpal joint. The univalent rotational joint (III) between the radius and wrist is applied so that the tilting of the wrist during the motion can be realized. As a bivalent cardan joint, joint (II) comprises the pro-/supination angle α, as well as a torsional rotation of radius with respect to ulna.

The whole set of vectors $\underline{r}_i$ forms a closed kinematic chain, written as:

$$\sum_{i=1}^{5} \underline{r}_i = \sum_{i=1}^{5} \begin{bmatrix} \underline{r}_{xi} \\ \underline{r}_{yi} \\ \underline{r}_{zi} \end{bmatrix} = 0 \tag{2.1}$$

Giving the initial conditions $\alpha = 90^\circ = \alpha_s$ at supination position, one has

$$\boldsymbol{r}_1(\alpha_s) = l_1 \cdot \begin{bmatrix} 0 \\ 1 \\ 0 \end{bmatrix};\ \boldsymbol{r}_2(\alpha_s) = l_2 \cdot \begin{bmatrix} 1 \\ 0 \\ 0 \end{bmatrix};\ \boldsymbol{r}_3(\alpha_s) = l_1 \cdot \begin{bmatrix} 0 \\ -1 \\ 0 \end{bmatrix};\ \boldsymbol{r}_4(\alpha_s) = l_2 \cdot \begin{bmatrix} -1 \\ 0 \\ 0 \end{bmatrix};\ \boldsymbol{r}_5(\alpha_s) = 0 \tag{2.2}$$

2.2.3 Forearm elastokinematic surrogate mechanism with 2DOF

A new mechanism is proposed by Kecskeméthy and Weinberg [24]. They integrated virtual springs to model the elastic components, for example ligaments, in their surrogate mechanism. The operating presumption of this mechanism is that it is at a fixed flexural position of the elbow, and therefore the proper elbow joint is not shown. Fig. 2.7 shows the corresponding surrogate mechanism that allows one to model the effects described above [24].

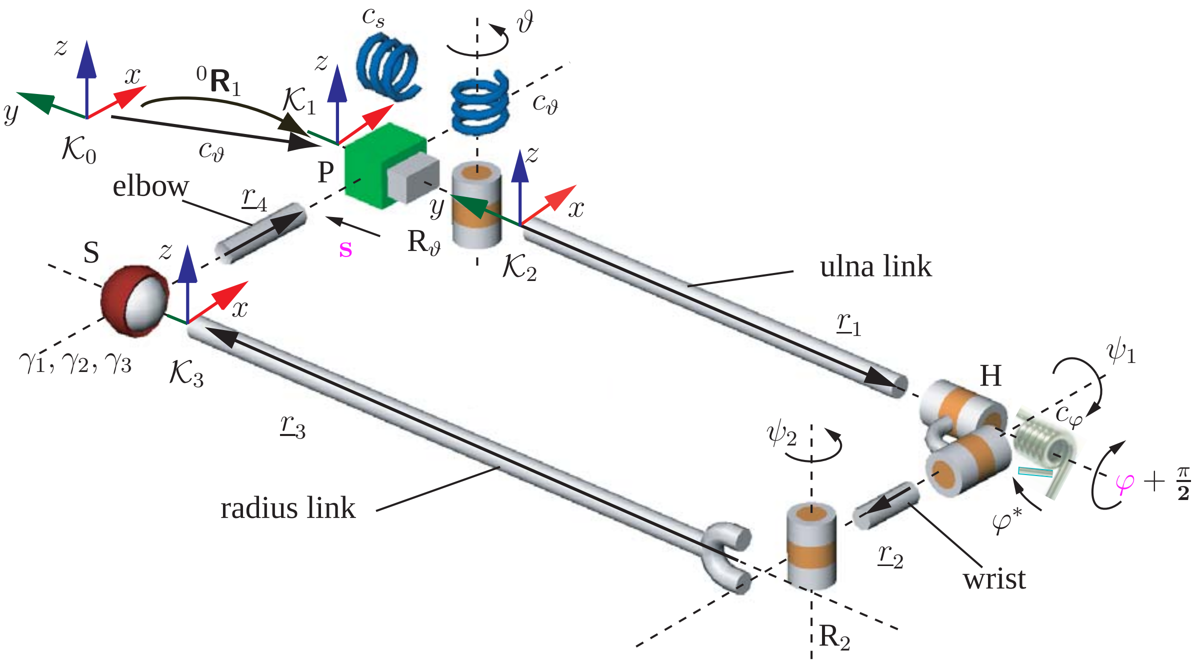

Fig. 2.7: Two-degrees-of-freedom surrogate mechanism for pro- and supination.

The surrogate mechanism consists of a closed kinematic chain with four joints and two degrees of freedom. The prismatic joint P and the revolute R on the proximal end of ulna, represent a small dislocation s and and a small lateral swaying ϑ of the ulna with respect to the humerus. The Hooke joint H represents the distal radio-ulnar joint, consisting of the actual pro-/supination angle φ and the torsional angle ψ_1. The joint R_2 describes the aperture ψ_2 between ulna and radius, and the spherical joint S represents the radial head at the proximal end of radius. The vectors $\underline{r}_1$, $\underline{r}_2$, $\underline{r}_3$, $\underline{r}_4$ represent the corresponding link lengths. At the humero-ulnar joints, two virtual springs with corresponding spring stiffnesses c_s and c_ϑ are placed in order to summarize all elastic effects at these joints, including ligaments, capsules etc. For kinetostatic analysis, a control moment ensuring motion at the other joints is applied on the ulnar axis with a described pronation angle φ and with user supplied input values, c_φ

and φ^*, for the stiffness and the offset of the deflection of a torsional spring respecively.

As the global home system, the inertial frame $\mathcal{K}_0$ is introduced. In this system, MRI data is collected. For the forearm description, we introduce an elbow frame $\mathcal{K}_1$ which may move with respect to the inertial frame from measurement to measurement with corresponding radius vector ${}_0\underline{r}_1$ and relative rotation matrix ${}^0\mathbf{R}_1$. The frames $\mathcal{K}_2$ and $\mathcal{K}_3$ are bone-fixed and are placed at the origin of the corresponding links.

To mathematically describe the rotation, a concept named kinetostatic coupling is defined as the ratio of c_ϑ/c_s. As shown in Fig. 2.8, the larger this ratio is, the smaller the rotational angle is. When the value is close to ∞, the rotational angle becomes so small that it can be ignored, thus only the translational behavior can be observed in the case. Conversely, when this ratio is close to 0, no translational behavior but a large swaying can be observed. The relation of this kinetostatic coupling to the motion will be verified in the later chapter.

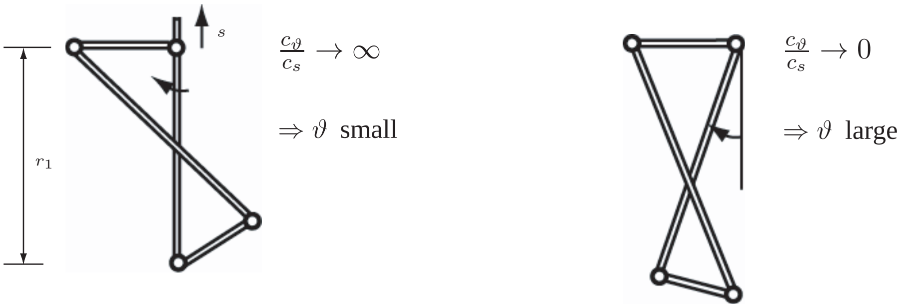

Fig. 2.8: Kinetostatic coupling.

This 2DOF mechanism is compared with the aforementioned fixed-axis one in Fig. 2.9. In the fixed-axis model the ulna is assumed to remain fixed with respect to the elbow, and the radius is supposed to rotate about the axis passing through the center of the radial head and the radio-ulnar articulation joints [11]. However, these assumptions prove to be non-realistic by MRI measurements which shows that the ulna performs a small lateral swaying rotation and a small axial sliding along its axis with respect to the elbow (lateral motion of point B in Fig. 2.9b). This result indicates that the humero-ulnar (elbow) joint allows some tilting and dislocation.

The effect of the improvement of motion reproduction by the new mechanism is depicted in Fig. 2.10. According to Fick's fixed-axis model, the hand could not stay parallel to the elbow during rotation, and it would tilt unrealistically to the side of the body in the pronation position (Fig. 2.10b). In order to compensate this tilting, there is a need of a small penetration and a small lateral swaying of ulna at the elbow joint (Fig. 2.10c). This requirement demands

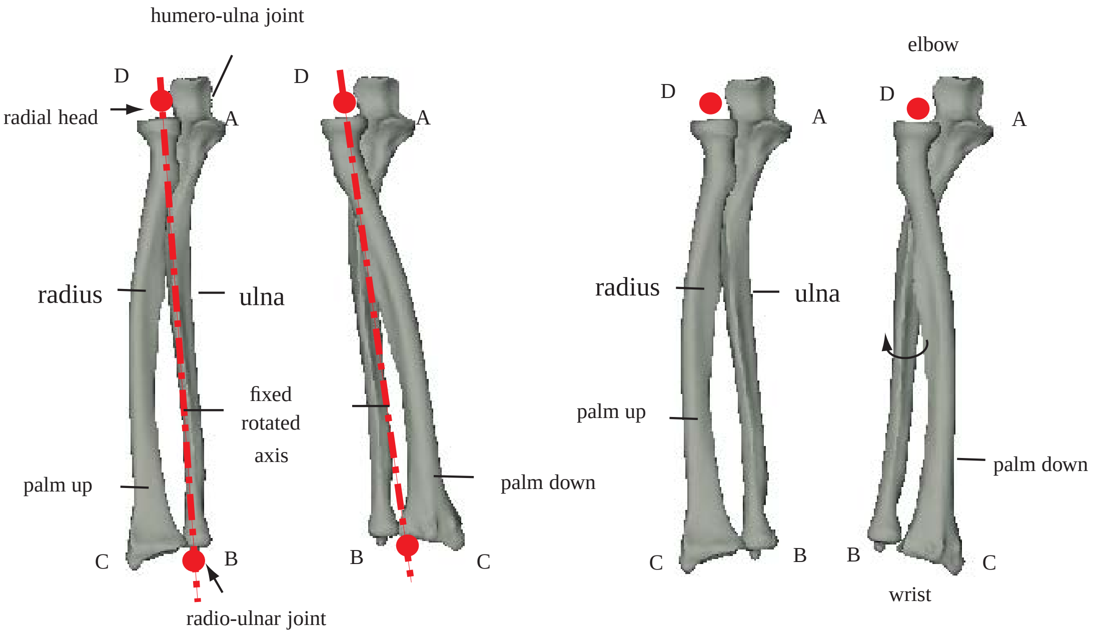

a) fixed-axis model b) 2-DOF model

Fig. 2.9: Simple and extended model of forearm pose at supination and pronation (right hand).

an additional revolute joint and an additional prismatic joint between elbow and ulna at point A. Furthermore, an additional revolute joint between radius and wrist is laid at point C. These two degrees of freedom are actually featured in the new 2DOF mechanism. It is worth mentioning that Joint C can be thought as a virtual rotation center within the radius corpus (Fig. 2.11). It is not a physical articulation but represents the center of curvature of the projection of the contact surface between radius and ulna at their distal radio-ulnear articulation on the plane spanned by ulna axis and distal radioulnar contact point.

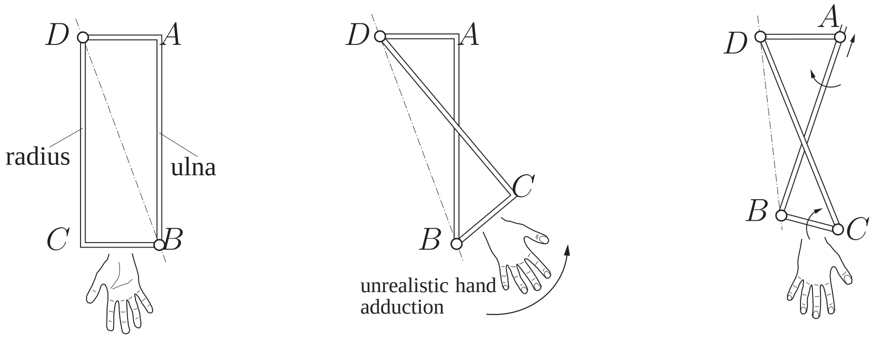

a) supination b) tilting of hand in pronation c) compensation of tilting

Fig. 2.10: Deficiencies of the fixed-axis model.

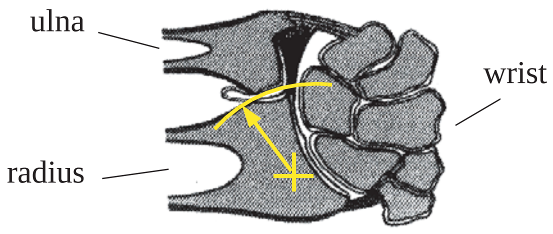

Fig. 2.11: Virtual rotation center at distal radius head.

2.2.3.1 Position Kinematics

To abstract the kinematics of this mechanism into mathematical expression, homogeneous vectors and the corresponding homogeneous transformation matrices which are usually applied for the characterization of rigid-body motions are used here [45]. The homogeneous coordinates are determined by the notation

$$\overset{\text{H}}{\underline{p}} = \begin{bmatrix} p_x \\ p_y \\ p_z \\ 1 \end{bmatrix} \tag{2.3}$$

and the homogeneous matrices are defined as

$$\mathsf{A} = \begin{bmatrix} \mathsf{R} & \underline{r} \\ 0 & 1 \end{bmatrix} = \begin{bmatrix} \rho_{11} & \rho_{12} & \rho_{13} & r_x \\ \rho_{21} & \rho_{22} & \rho_{23} & r_y \\ \rho_{31} & \rho_{32} & \rho_{33} & r_z \\ 0 & 0 & 0 & 1 \end{bmatrix} \tag{2.4}$$

The notation $\underline{p} = [p_x, p_y, p_z]^{\text{T}}$ is a general vector in the three-dimensional space. In the matrices, R is the orthogonal rotation matrix, in which the components ρ_{ij} depict the coordinates of the rotated unit vectors of the target frame in the base frame. $\underline{r}$ is the displacement vector, and its components define the position of the origin of the moving frame in coordinates of the base frame. In this way, the body-fixed coordinates $\underline{p}' = [p_{x'}, p_{y'}, p_{z'}]^{\text{T}}$ regarding to the moving frame can be transformed to the fixed coordinates $\underline{p} = [p_x, p_y, p_z]^{\text{T}}$ with respect to the base frame as

$$\begin{bmatrix} \underline{p} \\ 1 \end{bmatrix} = \begin{bmatrix} \mathsf{R} & \underline{r} \\ 0 & 1 \end{bmatrix} \begin{bmatrix} \underline{p}' \\ 1 \end{bmatrix} \quad . \tag{2.5}$$

The elementary transformations are introduced as:

$$\texttt{Rot}\,[\,\underline{e}_1,\Theta\,]=\begin{pmatrix}1&0&0&0\\0&\cos\Theta&-\sin\Theta&0\\0&\sin\Theta&\cos\Theta&0\\0&0&0&1\end{pmatrix}\quad,\quad\texttt{Trans}[\,\underline{e}_1,s\,]=\begin{pmatrix}1&0&0&s\\0&1&0&0\\0&0&1&0\\0&0&0&1\end{pmatrix}\tag{2.6a}$$

$$\texttt{Rot}\,[\,\underline{e}_2,\Theta\,]=\begin{pmatrix}\cos\Theta&0&\sin\Theta&0\\0&1&0&0\\-\sin\Theta&0&\cos\Theta&0\\0&0&0&1\end{pmatrix}\quad,\quad\texttt{Trans}[\,\underline{e}_2,s\,]=\begin{pmatrix}1&0&0&0\\0&1&0&s\\0&0&1&0\\0&0&0&1\end{pmatrix}\tag{2.6b}$$

$$\texttt{Rot}\,[\,\underline{e}_3,\Theta\,]=\begin{pmatrix}\cos\Theta&-\sin\Theta&0&0\\\sin\Theta&\cos\Theta&0&0\\0&0&1&0\\0&0&0&1\end{pmatrix}\quad,\quad\texttt{Trans}[\,\underline{e}_3,s\,]=\begin{pmatrix}1&0&0&0\\0&1&0&0\\0&0&1&s\\0&0&0&1\end{pmatrix}\tag{2.6c}$$

where $\underline{e}_i$ are the unit vectors in direction of the three coordinate axes, and Θ is a rotation angle, and s is a translation. Furthermore, a pure rotation and a pure translation can be denoted as:

$$\texttt{Rot}\,[\,\mathbf{R}\,]=\begin{bmatrix}\mathbf{R}&\underline{0}\\0&1\end{bmatrix}\ ;\ \texttt{Trans}[\,\underline{r}\,]=\begin{bmatrix}\mathbf{I}_3&\underline{r}\\0&1\end{bmatrix}\ ,\tag{2.7}$$

where $\mathbf{I}_n$ is a $n\times n$ identity matrix. The loop closure condition could be written as:

$$\begin{aligned}&\texttt{Trans}[\,y,s\,]\circ\texttt{Rot}\,[\,z,\vartheta\,]\circ\texttt{Trans}[\,y,-r_1\,]\circ\texttt{Rot}\,[\,y,\varphi+\pi/2\,]\circ\texttt{Rot}\,[\,x,\psi_1\,]\\&\circ\texttt{Trans}[\,x,-r_2\,]\circ\texttt{Rot}\,[\,z,\psi_2\,]\circ\texttt{Trans}[\,y,r_3\,]\circ\texttt{Rot}\,[\,y,\gamma_1\,]\circ\texttt{Rot}\,[\,z,\gamma_2\,]\\&\circ\texttt{Rot}\,[\,x,\gamma_3\,]\circ\texttt{Trans}[\,x,r_4\,]=\mathbf{I}_4\end{aligned}\tag{2.8}$$

where $\circ$ is the composition operator used to define the concatenation of two subsequent transformations. Referring to

$$\mathbf{A}^{-1}=\begin{bmatrix}\mathbf{R}^{\mathrm{T}}&-\mathbf{R}^{\mathrm{T}}\,\underline{r}\\0&1\end{bmatrix}\tag{2.9}$$

and that $\texttt{Trans}[\,x,-r_2\,]$ and $\texttt{Rot}\,[\,x,\psi_1\,]$ commute for the particular geometry at hand, the individual transformations in Eq. (2.8) can be reorganized to render an alternative loop closure condition,

$$\begin{aligned}
&\texttt{Rot}\,[\,x,\psi_1\,]\circ\texttt{Rot}\,[\,z,\psi_2\,]\circ\texttt{Trans}[\,y,r_3\,]\circ\texttt{Rot}\,[\,y,\gamma_1\,]\circ\texttt{Rot}\,[\,z,\gamma_2\,]\circ\texttt{Rot}\,[\,x,\gamma_3\,]\\
&\quad=\ \texttt{Trans}[\,x,r_2\,]\circ\texttt{Rot}\,[\,y,-(\varphi+\pi/2)\,]\circ\texttt{Trans}[\,y,r_1\,]\circ\texttt{Rot}\,[\,z,-\vartheta\,]\circ\texttt{Trans}[\,y,-s\,]\\
&\qquad\circ\texttt{Trans}[\,x,-r_4\,]\ .
\end{aligned}\tag{2.10}$$

From this equation, it can be seen that the transformation from the wrist point C to the humero-radial joint S , after commuting $\texttt{Trans}[-\underline{r}_2\,]$ and $\texttt{Rot}\,[\,x,\psi_1\,]$, can be described by two sets of sequences, either through ψ_1, ψ_2, $\underline{r}_3$, γ_1, γ_2, γ_3, or through the sequence $-\underline{r}_2$, $-\varphi$, $-\underline{r}_1$, $-\vartheta$, $-s$, $-\underline{r}_4$.

In matrix form, Eq. (2.10) becomes

$$\begin{aligned}
&\begin{bmatrix}1&0&0&r_2\\0&1&0&0\\0&0&1&0\\0&0&0&1\end{bmatrix}\cdot\begin{bmatrix}-\sin\varphi&0&-\cos\varphi&0\\0&1&0&0\\\cos\varphi&0&-\sin\varphi&0\\0&0&0&1\end{bmatrix}\cdot\begin{bmatrix}1&0&0&0\\0&1&0&r_1\\0&0&1&0\\0&0&0&1\end{bmatrix}\cdot\\
&\begin{bmatrix}\cos\vartheta&\sin\vartheta&0&0\\-\sin\vartheta&\cos\vartheta&0&0\\0&0&1&0\\0&0&0&1\end{bmatrix}\cdot\begin{bmatrix}1&0&0&0\\0&1&0&-s\\0&0&1&0\\0&0&0&1\end{bmatrix}\cdot\begin{bmatrix}1&0&0&-r_4\\0&1&0&0\\0&0&1&0\\0&0&0&1\end{bmatrix}\\
=&\begin{bmatrix}1&0&0&0\\0&\cos\psi_1&-\sin\psi_1&0\\0&\sin\psi_1&\cos\psi_1&0\\0&0&0&1\end{bmatrix}\cdot\begin{bmatrix}\cos\psi_2&-\sin\psi_2&0&0\\\sin\psi_2&\cos\psi_2&0&0\\0&0&1&0\\0&0&0&1\end{bmatrix}\cdot\begin{bmatrix}1&0&0&0\\0&1&0&r_3\\0&0&1&0\\0&0&0&1\end{bmatrix}\cdot\begin{bmatrix}&&&0\\&\mathbf{R}_S&&0\\&&&0\\0&0&0&1\end{bmatrix}
\end{aligned}\tag{2.11}$$

where $\mathbf{R}_S=\mathbf{R}(\gamma_1,\gamma_2,\gamma_3)$ is the rotation matrix at the spherical joint.

From this matrix equation, proper scalar equations can be extracted to determine the three unknown parameters: φ (pro-/supination angle), ψ_1 (torsional angle between ulna and radius) and ψ_2 (aperture angle) between ulna and radius. There are 12 nonvanishing equations in Eq. (2.11) and six of them are independent. There are 8 elementary degrees of freedom at the joints in the surrogate mechanism, which are denoted by the variables

$\underline{\beta} = [s, \vartheta, \varphi, \psi_1, \psi_2, \gamma_1, \gamma_2, \gamma_3]^{\mathrm{T}}$. Due to the particular geometry of the loop, its degrees of freedom are constrained to 2 (s and φ) and the other 6 variables are functions of the two degrees of freedom, which can be determined in closed form. Such a kind of closed-form solution can be solved by an approach, which is proposed by Kecskemethy and Hiller [46], in order to find a suitable sequence of equations automatically. This is reproduced here for better reference.

In the approach since the position of all the bodies of the loop can be determined by computing the variables $\vartheta, \psi_1, \psi_2$, there is no need to take the spherical joint angles $\gamma_1, \gamma_2, \gamma_3$ into account. One can multiplicate the basis vectors Eq. (2.12) from the left and right of Eq. (2.11) to get the scalar equations.

$$\overset{\mathrm{H}}{\underline{e}}_1 = \begin{bmatrix} 1 \\ 0 \\ 0 \\ 0 \end{bmatrix} , \; \overset{\mathrm{H}}{\underline{e}}_2 = \begin{bmatrix} 0 \\ 1 \\ 0 \\ 0 \end{bmatrix} , \; \overset{\mathrm{H}}{\underline{e}}_3 = \begin{bmatrix} 0 \\ 0 \\ 1 \\ 0 \end{bmatrix} , \; \overset{\mathrm{H}}{\underline{o}} = \begin{bmatrix} 0 \\ 0 \\ 0 \\ 1 \end{bmatrix} \; . \tag{2.12}$$

In this equation, $\overset{\mathrm{H}}{\underline{e}}_i, i = 1, 2, 3$ are the three orientation vectors in the direction of three coordinate axes, respectively, which are perpendicular to the coordinate planes. $\overset{\mathrm{H}}{\underline{o}}$ is the position vector describing the origin of the coordinate system. Note that, for orientation vectors, it holds

$$\mathbf{A}^{-1} \overset{\mathrm{H}}{\underline{e}} = \mathbf{A}^{\mathrm{T}} \overset{\mathrm{H}}{\underline{e}} \; . \tag{2.13}$$

Due to this property, multiplication from the left of a homogeneous matrix is defined for an orientation vector:

$$\overset{\mathrm{H}}{\underline{u}}{}^{\mathrm{T}} \mathrm{A} = \left(\mathrm{A}^{\mathrm{T}} \overset{\mathrm{H}}{\underline{u}} \right)^{\mathrm{T}} = \left(\mathrm{A}^{-1} \overset{\mathrm{H}}{\underline{u}} \right)^{\mathrm{T}} . \tag{2.14}$$

The ‘homogeneous norm’ for positional vectors can be defined as:

$$\| \underline{\xi} \|_{\mathrm{H}} = \sqrt{\| \underline{\xi} \|^2 - 1} \;\; , \tag{2.15}$$

where $|| \cdot ||$ denotes the Euclidean norm. It features

$$\| \mathrm{A} \, \overset{\mathrm{H}}{\underline{o}} \, \|_{\mathrm{H}} = \| \mathrm{A}^{-1} \, \overset{\mathrm{H}}{\underline{o}} \, \|_{\mathrm{H}} \; . \tag{2.16}$$

This equation describes that the distance between the origins of a fixed and a moving frame doesn’t depend on the direction of transformation.

When Eq. (2.11) is multiplied with $\overset{\mathrm{H}}{\underline{o}}$ from the right by the homogeneous norm, the effects of the spherical joint as well as the two rotations ψ_1 and ψ_2 are evidently excluded. The derived fact is that the distance between the center of the spherical joint and the radial-side intersection point of the two axes for ψ_1 and ψ_2 is independent of the corresponding joint variables.

Equating the square of the homogeneous norms on both sides yields for the remaining unknown ϑ

$$A(s,\varphi)\,\cos\vartheta + B(s,\varphi)\,\sin\vartheta + C(s) = 0 \;\;,\;\; \text{where} \;\left\{\begin{array}{lcl} A &=& 2\,(r_2\,r_4\,\sin\varphi - r_1\,s) \\ B &=& 2\,(r_2\,s\,\sin\varphi - r_1\,r_4) \\ C &=& r_1^2 + r_2^2 + r_4^2 + s^2 - r_3^2 \end{array}\right. \tag{2.17}$$

This equation can be rewritten as

$$\overline{C}\,\cos(\vartheta - \vartheta^*) + C = 0 \;\;,\;\; \text{where}\;\; \overline{C} = \sqrt{A^2 + B^2} \;\;,\;\; \tan\vartheta^* = \frac{B}{A} \;\;, \tag{2.18}$$

and

$$\sin\psi_2 = -\frac{r_2 + \sin\varphi\,(r_4\,\cos\vartheta + s\,\sin\vartheta)}{r_3} \;\;. \tag{2.19}$$

$$\tan\psi_1 = -\frac{\cos\varphi\,(\,r_4\,\cos\vartheta + s\,\sin\vartheta\,)}{r_1 + r_4\,\sin\vartheta - s\,\cos\vartheta} \;\;. \tag{2.20}$$

Hence, the three variables $\vartheta, \psi_1, \psi_2$ for the determination of the closed from solution can be derived from the two degrees of freedom s and φ.

2.2.3.2 Velocity relationships

In the kinetostatic modeling, it is needed to transmit the degrees of freedom to the pro-/supination angle φ, and therefore the Jacobian of the transmission is required. From Eq. (2.17) it follows

$$A_\vartheta\,\dot{\vartheta} + A_s\,\dot{s} + A_\varphi\,\dot{\varphi} = 0 \;\;, \tag{2.21a}$$

where

$$\left\{\begin{array}{lcl} A_\vartheta &=& r_4\,(\,r_1\,\cos\vartheta - r_2\,\sin\vartheta\sin\varphi\,) + s\,(\,r_2\,\cos\vartheta\sin\varphi + r_1\,\sin\vartheta\,) \\ A_s &=& r_2\,\sin\vartheta\sin\varphi + r_1\,\cos\vartheta \\ A_\varphi &=& r_2\,(\,r_4\,\cos\vartheta + s\,\sin\vartheta\,)\cos\varphi \end{array}\right. \tag{2.21b}$$

thus

$$\dot{\vartheta} = [J_s \ \ , \ \ J_\varphi] \begin{bmatrix} \dot{s} \\ \dot{\varphi} \end{bmatrix} = \mathbf{J}\,\underline{\dot{q}} \tag{2.22a}$$

where $\mathbf{J} = [J_s, J_\varphi]$ is the Jacobian of the transmission, and $\underline{q} = [s, \varphi]^{\mathrm{T}}$ is the vector of input coordinates. The Jacobian coefficients J_s and J_φ follow as

$$J_s = -\frac{A_s}{A_\vartheta} = -\frac{r_2 \sin\vartheta \sin\varphi + r_1 \cos\vartheta}{r_4\,(\,r_1 \cos\vartheta - r_2 \sin\vartheta \sin\varphi\,) + s\,(\,r_2 \cos\vartheta \sin\varphi + r_1 \sin\vartheta\,)} \tag{2,22b}$$

$$J_\varphi = -\frac{A_\varphi}{A_\vartheta} = -\frac{r_2\,(\,r_4 \cos\vartheta + s \sin\vartheta\,)\cos\varphi}{r_4\,(\,r_1 \cos\vartheta - r_2 \sin\vartheta \sin\varphi\,) + s\,(\,r_2 \cos\vartheta \sin\varphi + r_1 \sin\vartheta\,)} \tag{2.22c}$$

Typically $\vartheta << 1$, therefore the denominator is always positive and the transmission is free from singularities. On the other hand, the Jacobian coefficient J_φ becomes zero at the supination and pronation positions when $\varphi = \pi/2$ and $\varphi = -\pi/2$. This indicates that this model advocates that the swaying motion of the ulna is "locked" with respect to axial rotation of the forearm at supination and pronation. In the other word, lateral forces do not generate a tendency at pronation and supination, but do at other axial rotations.

2.2.3.3 Kinetostatics

As discussed above in the kinematics of the mechanism, the forearm motion can at the end be described in the model as functions of two degrees of freedom, the dislocation s and the swaying angle ϑ at the humero-ulnar joint. Typically for pro- and supination the rotation with respect to the ulnar axis (denoted by φ) is prescribed, with the motion at the other joints as resultants. However, the two degrees of freedom make the distribution of the rotation on the individual relative joint motions, non-unique. As a solution for these small perturbations, two virtual springs are therefore introduced into the mechanism at the two humeroulnar joints, with yet unknown stiffness coefficients c_s and c_ϑ respectively (Fig. 2.7). Thus, the forearm motion can be actuated by a torque applied in direction of the pronation angle, which can be imagined in the way that the hand is twisted with an external moment applied about the middle finger. The consequent effect on the two degrees of freedom is that one of them will be more deflected than the other. This effect is up to the ratio of the two spring stiffness c_s and c_ϑ. When the modeling result is compared to the measured one, e.g. by MRI, the stiffness ratio can be determined in order to reproduce the observed geometric motion. Along this line, the problem mentioned at the beginning concerning on the accuracy of the two degrees of freedom mechanism can be solved by measuring the global gross motion behavior and then defining the stiffness ratio.

To determine the ratio from geometric measurements, the force transmission is described by a simple relationship between motion and force proposed by Kecskemethy [47]. The relationship is regarded as a kinetostatic transmission element which can transmit the motion and force in an ideal way without bringing the change of power (Fig. 2.12).

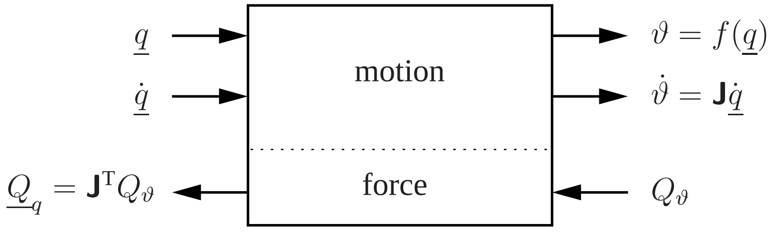

Fig. 2.12: Model of the kinetostatic transmission element.

Mathematically, the force at the prismatic joint P is defined as Q_s , the torque with respect to the revolute joint R$_\vartheta$ as Q_ϑ, and the torque about the pronation rotation φ as Q_φ. The force and torque at the input joints can be described by a vector $\underline{Q}_q = [Q_s, Q_\varphi]^{\mathrm{T}}$. The power equality at input and output is

$$\underline{Q}_q^{\mathrm{T}} \, \dot{\underline{q}} = Q_\vartheta \, \dot{\vartheta} \quad . \tag{2.23}$$

When the kinematical relationship (2.23a) is introduced, it becomes

$$\underline{Q}_q^{\mathrm{T}} \, \dot{\underline{q}} = Q_\vartheta \, \mathbf{J} \, \dot{\underline{q}} \quad .$$

Since the relationship must hold independently of the input velocity, the coefficients $\dot{\underline{q}}$ can be removed from both sides and the following equation can be obtained:

$$\underline{Q}_q = \mathbf{J}^{\mathrm{T}} \, Q_\vartheta \quad , \tag{2.24}$$

which means that the transmission of forces can be performed by the transposed Jacobian in the opposite direction to the velocities.

The deflection at the joints is arised while applying the forces and torques at the virtual springs. A control moment along the pronation axis is used which is regulated by an additional spring law with the form

$$Q_\varphi = c_\varphi \, (\, \varphi - \varphi^* \,) \ \ , \tag{2.25a}$$

In this form φ^* and c_φ need to be input. φ^* stands for the offset of the deflection, and c_φ denotes the stiffness of a torsional spring applying with respect to the pronation axis. Since it holds $Q_s = c_s \, s$ and $Q_\vartheta = c_\vartheta \, \vartheta$ at the humeroulnar degrees of freedom, based on Eq. (2.24) the following equations can be derived

$$c_s \, s \ = \ J_s \, c_\vartheta \, \vartheta \ \ , \tag{2.25b}$$

$$c_\varphi \, (\varphi - \varphi^* \,) \ = \ J_\varphi \, c_\vartheta \, \vartheta \ \ . \tag{2.25c}$$

For a given φ^*, these equations can be solved by a Newton-Raphson solver to result the three variables φ, ϑ, s which determine the subsequent static equilibrium position. Since the variables are dependent on the input value φ^*, a sequence of equilibrium positions $s(\varphi^*)$, $\vartheta(\varphi^*)$, $\varphi(\varphi^*)$ obtained for given φ^*. Therefore the computed functions $s_C(\varphi)$ and $\vartheta_C(\varphi)$ can be constructed to describe the deflections at the degrees of freedom for a given pronation angle. Because the computed functions depend on the applied stiffness coefficients, the kinetostatic coupling of ϑ and s is in terms of new independent input φ^*.

Therefore, in Eq. (2.25c), if a sping stiffness coefficient c_φ is set arbitrarily and the spring offset φ^* is chosen according to user specified values, the loop will then move to its new equilibrium position. In the point view of the user, it looks like the operation is done by a single given input φ^*.

2.3 Visualisation of human forearm motion

2.3.1 Coordinate of bone geometry

For the visualisation of the human forearm motion, it is required to define appropriate coordinate systems. For the right forearm, these are as follows (Fig. 2.13):

1. The humeral origin is placed at the midpoint of trochlea of humerus; the *z* axis is parallel to the shaft pointing to the shoulder; the *y* axis is directed towards the ulna

styloid; and the *x* axis points laterally.

2. The radial origin is placed at the centroid of capitulum of the humerus; the *y* axis is parallel to the shaft; the *x* axis points laterally; and the *z* axis points anteriorly.
3. The ulnar origin is defined as the middle point on the sagittal ridge of the greater sigmoid notch; the *y* axis is parallel to the shaft; the *x* axis points laterally; and the *z* axis points anteriorly.

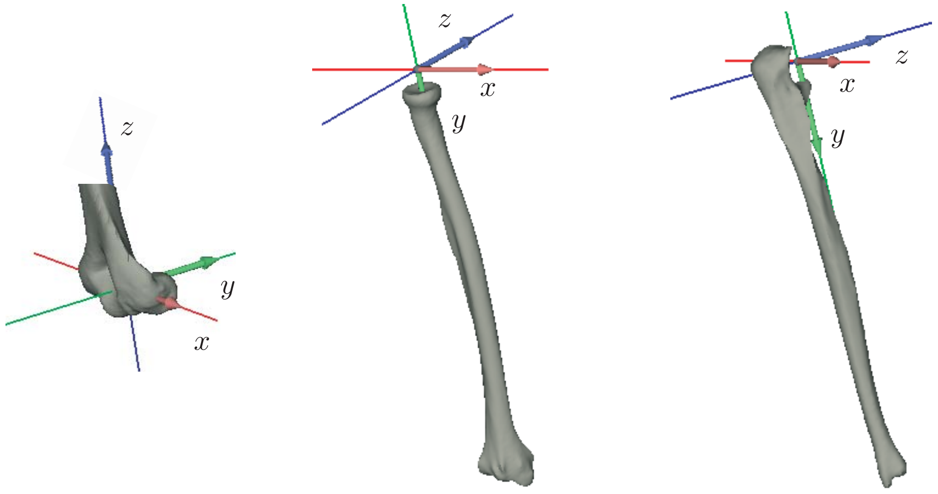

Fig. 2.13: Anatomic coordinate systems embedded for bones.

2.3.2 Programming environment

The object-oriented multi-body programming library MOBILE [48] is used for the implementation of the model and the visualisation of the forearm motion. The software MOBILE is a C++ library used for the modeling of multi-body systems. It consists of not only classes representing state objects and kinetostatic transmission elements (including objects for solving constraint equations), but also objects to generate, solve and integrate the equations of motion.

In order to provide the end user a vivid appearance of the forearm bones motion, surface models of the bones are attached to the moving frames (Fig. 2.14). As shown in this figure, beside the window for the visualization of the modeling, there is a panel on the left side for the adjustment of parameters via sliding bars. Thus, the pro- and supination motion can be visualized online for any given setting, e.g. rigid body motion parameters from inertial frame to elbow frame, spring stiffnesses, offset, and pro-/supination angle.

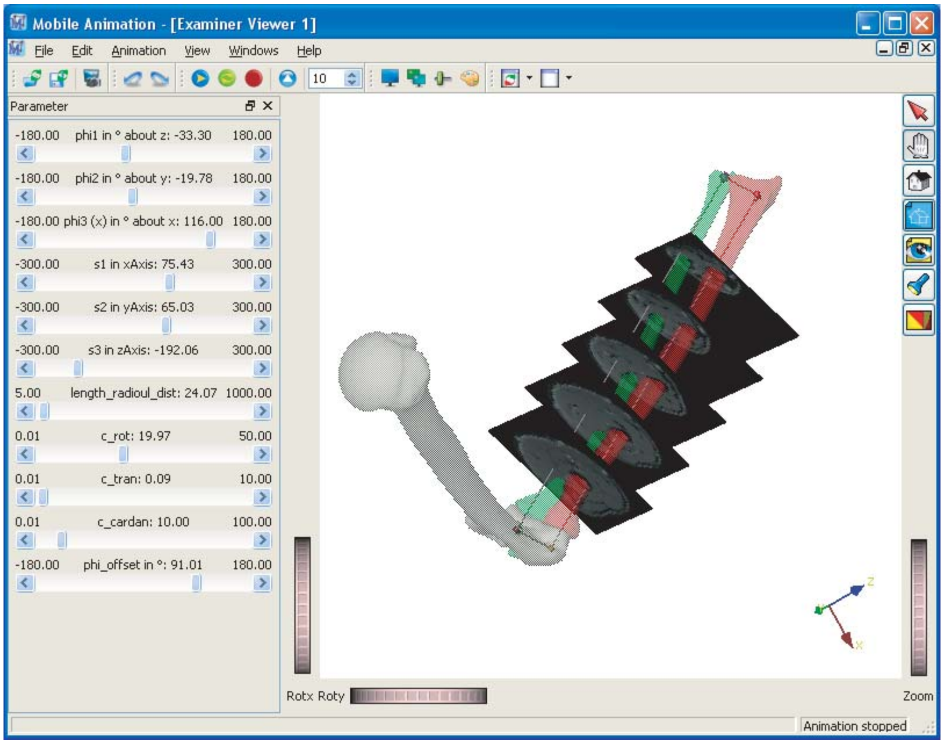

-180.00 phi1 in ° about z: -33.30 180.00
-180.00 phi2 in ° about y: -19.78 180.00
-180.00 phi3 (x) in ° about x: 116.00 180.00
-300.00 s1 in xAxis: 75.43 300.00
-300.00 s2 in yAxis: 65.03 300.00
-300.00 s3 in zAxis: -192.06 300.00
5.00 length_radioul_dist: 24.07 1000.00
0.01 c_rot: 19.97 50.00
0.01 c_tran: 0.09 10.00
0.01 c_cardan: 10.00 100.00
-180.00 phi_offset in °: 91.01 180.00

Fig. 2.14: Screen shot of the developed simulation environment for pro-/supination.

Chapter 3

Model Parameter Fitting from MRI Measurements

To obtain model parameters from the measured data, an automatic fitting method was developed which can self-calibrate the arm position in the MRI scanning tube and fit the model parameters from MRI scans. The fitting process was run by reducing the errors between the simulated and measured values in an optimization loop. Thereafter, a multibody programming library was used to implement the model into its graphical user interface in order to animate the forearm motion and provide a 3D visualisation. Finally the 2DOF model used for this study was compared to the fixed-axis model described in Section **2.2.1**, in terms of absolute motion of bone ulna and bone radius relative to the humerus, and the relative motion between ulna and radius.

3.1 MRI measurements

1. MRI background:

In previous studies, different methods have been used to get information on the forearm geometry, from in-vitro to in-vivo. The application of the in-vitro method on forearm motion analyses has inherent limitations such as the absence of physiological muscle loading, passive simulation of forearm rotation, and artificial fixation of the ulna bone. As a non-invasive medical imaging method, magnetic resonance imaging was used in many investigations, although it is still a relatively new technology. The MRI image was firstly published in 1973

[49]. In January 1974, its first application on getting cross-sectional images from a living mouse was reported. MRI can be used to visualize detailed internal structure and limited function of the body. In the MRI scanning, the magnetization of some atoms in the body can be initialized under a powerful magnetic field, and the alignment of this magnetization can be tuned by the radio frequency fields. The generated rotating magnetic field can be detected by the scanner, and the signal can be manipulated by additional magnetic fields to build up so much information that an image of the scanned area of the body can be constructed. Compared to computed tomography (CT), it can provide much better contrast between the soft tissues. Moreover, there is no ionizing radiation in MRI measurements.

2. Subject:

In this study, only one test was perforamed with a male subject of age 30. Moreover, data collected in a previous measurement in the clinic of Heiderburg in 2007 was also inlcuded in this setting. All the tests followed the same measurement protocol.

3. Torque device:

In order to observe the influence of wrist load on forearm kinematics, a special torque generation device was prepared and used (Fig. 3.1(a)). It is a plastic device featuring a rotatable handle on a box placed at the end of the MRI scanning tube (Fig. 3.2). The device allowed us to produce, via a Bungee cord, a resisting torque while operating the handle to a corresponding rotational angle which could be read directly from the goniometer (Fig. 3.1(b)). The torque generated by this device was in the range from 0 to 8.3 Nm. Five blocks (shown as position 1-5 in Fig. 3.1(a)) asured the obtained torques roughly constant (ca. 4.2 Nm in the experiments) at prescribed rotational angles.

Considering the operation condition of MRI (no magnetic elements permitted), the raw material of the box was made of PVC, and the long rotational stick (black) was made of carbon fiber. This device had an optimal dimension fitting to the height of MRI scanning tube and the operating place, so that the tester could hold/rotate the handle without uncomfortableness (Fig. 3.2).

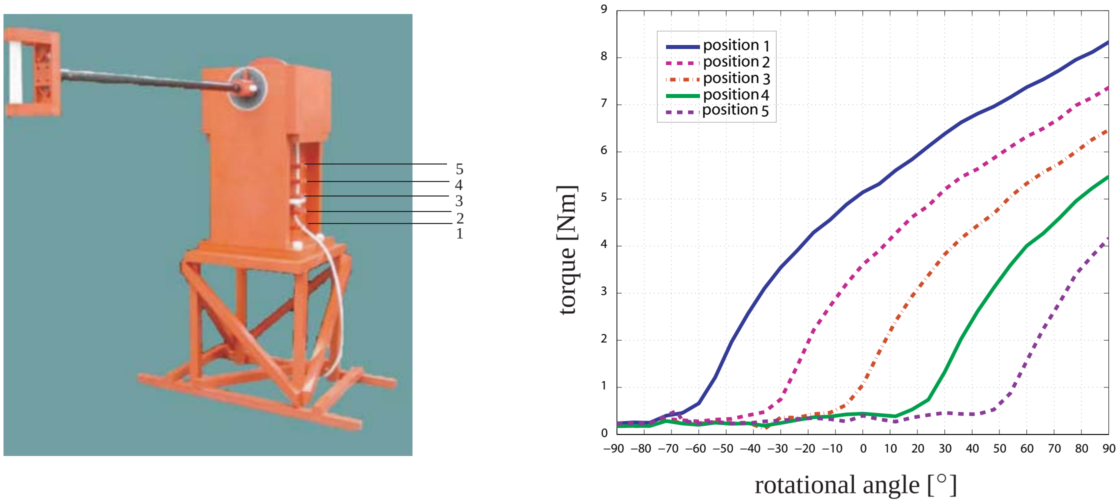

(a) torque generated device

(b) calibration graph of the device

Fig. 3.1: Schematic of the torque device and the calibration graph.

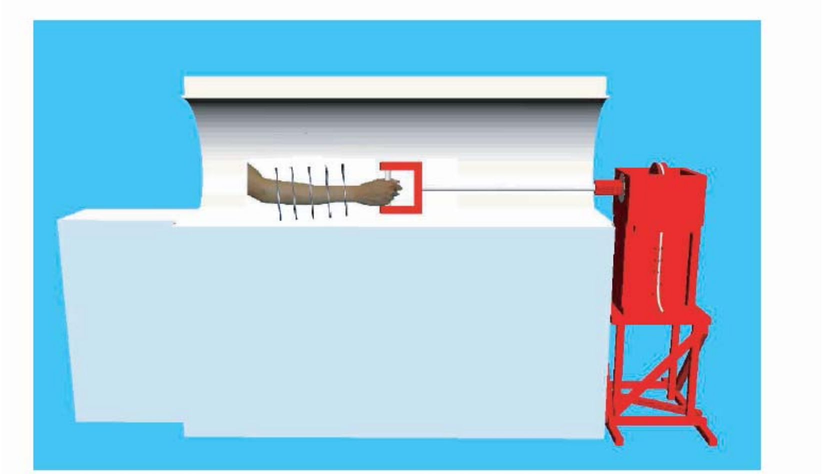

Fig. 3.2: Schematic location of the torque device in MRI scanning.

4. Scanning protocol:

The position of the subject (tester) inside the MRI scanner tube was carried out on the table with the elbow in 45° flexion (Fig. 3.3(a)). An adjustable support cushion under the subject's arm and chest increased the comfort of the subject during scanning and thus helped to maintain the subject's position stable. Gripping the goniometer at 0° of rotation aligned the dorsopalmer axis with the x axis of the scanner, the length of the forearm with the y axis of the scanner, and the radioulnar axis of the wrist with the z axis of the scanner. MRI scanning was performed from the distal humerus to the proximal carpal row.

In this study two sets of MRI measurements, fine scans and motion scans, were performed:

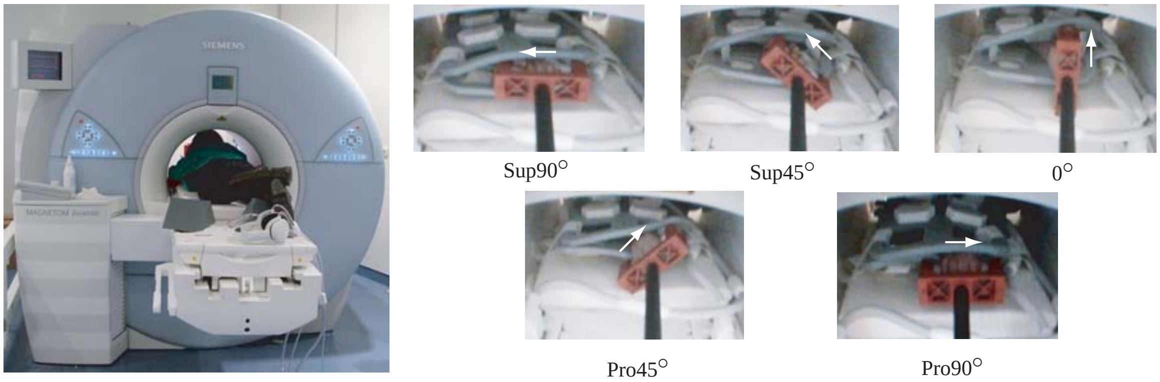

(a) tester on MRI table (b) holding the handle at defined rotational angles

Fig. 3.3: MRI device and defined rotational positions.

(1) **Fine MRI scans** were carried out for the determination of the bone geometry and the result was used as the reference in the later study. For each tester, around forty images were taken with the forearm at a fixed position. From these reference scans, a quite smooth distribution of the bone marrow centroid lines and the cross-sectional areas along the MRI axial direction could be obtained by using automatic segmentation. The derived bone geometry was used as a reference in subsequent applications of the simulation package.

(2) **Motion scans** recorded the forearm rotational motion. For each tester series of the images were taken at three torque conditions and at defined rotational pro-/supination angles from maximum supination, 45° supination, neutral, 45° pronation to maximum pronation (as shown in Fig. 3.3(b)). The toque conditions were (1) no resistive torque, (2) torque of 4.2Nm against pronation, and (3) torque of 4.2Nm against supination. This active torque was generated by the device while the tester grasped the handle and held the forearm against the grip at defined rotational positions as described above. At each condition for each tester, five/seven (in clinic of Heidelberg/Essen respectively) cross-section MRI slices were taken along the forearm length with fixed distance between each other (Table 3.5).

The fine MRI scan was performed only at one angle position, with a scanning time of approximately 4 min. In the case of motion scan a limited set of MRI slices $S_1, \ldots, S_M$ (M =5/7) were scanned under each condition, where the time duration for each series was less than 30 seconds. Since the slices for one angle position were taken roughly simultaneously, they could represent the same forearm position. In the analysis the images were reconstructed with a display field of view, such as 240*240mm and an in-plane resolution of 0.9375*0.9375mm^2. The following Table 3.1 and Table 3.2 detail the parameters for acquisition:

Table 3.1: Image parameters taken at clinic Heidelberg

image parameters	repetition time (ms)	echo time (ms)	field of view (mm^2)	slice matrix	slice thickness (mm)	slice number	slice distance (mm)
fine scan	3657.4	15	160*160	0.3125*0.3125	5	40	10
motion scan	143.3	13.8	240*240	0.9375*0.9375	5	5	37

Table 3.2: Image parameters taken at clinic Essen

image parameters	repetition time (ms)	echo time (ms)	field of view (mm^2)	pixel spacing	slice thickness (mm)	slice number	slice distance (mm)
fine scan	3000	11	146*199	0.5208*0.5208	3	47	6
motion scan	3000	11	146*200	0.7813*0.7813	3	7	36

5. MRI images and the corresponding information:

The MRI image data were saved in DICOM format. DICOM (Digital Imaging and Communications in Medicine) is a standard for handling, storing, printing, and transmitting information in medical imaging, such as CT and MRI scans. It defines a data dictionary, data structures, file formats, client and server services, workflow, etc. A DICOM file contains both a header portion, including items such as patient ID, study time, series time, acquisition data etc, as well as the image data such as the image pixels.

6. Coordinate systems in DICOM:

A single *patient-centered* coordinate system is used in the DICOM standard to locate points in three-dimentional space. This system is defined with respect to the patient's body. Dicom standard contains the following tags recording the information of image position and orientation:

1. Image Position (0020, 0032): specifies the *x*, *y*, and *z* coordinates of the upper left corner of the image. This tag defines the coordinates of the first voxel transmitted.
2. Image Orientation (0020, 0037): specifies the direction cosines of the first row and the first column with respect to the patient. This data allows one to uniquely determine the mapping between the image and the cooresponding view plane. Hereby, the *x* axis points to patient's left-hand side, the *y* aixs points to the posterior side of the patient, and *z* axis increases toward the head of the patient.

3. Patient position (0018, 5100): describes the location relative to the equipment required for MR images. The often used descriptors are: HFP (head first-prone), HFS (head first-supine), HFDR (head first-decubitus right), HFDL (head first-decubitus left), FFP (feet first-prone), FFS, FFDR, FFDL. In our MRI measurements the tester was nearly aligned on the table, and thus HFP was used.

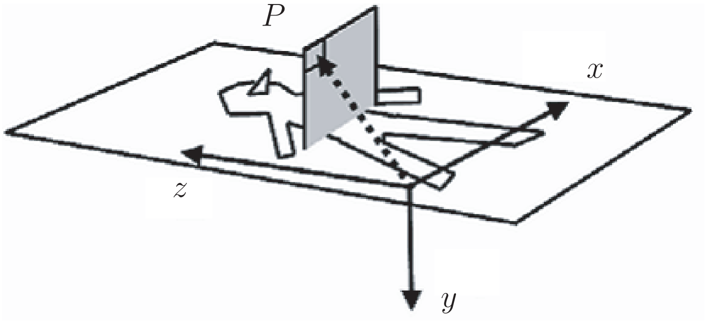

Fig. 3.4: DICOM patient-space coordinate.

7. MRI slices in the Open Inventor suite:

Open Inventor is a library of objects and methods used to create interactive 3D graphics application [50]. In order to draw MRI images in space, two classes were used, *SoIndexedFaceSet* and *SoTexture2*. *SoIndexedFaceSet* represents a 3D shape formed by constructing faces (polygons) from vertices located at the coordinates specified in the *vertexProperty* field. The *SoTexture2* defines a texture map and parameters for this map that is used to apply texture to subsequent shapes as they are rendered. An example series of visualized MRI slice in sequence is shown in Fig. 3.5.

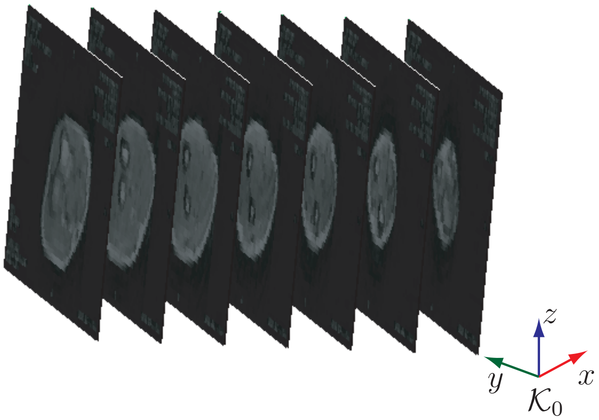

Fig. 3.5: Visulized MRI slices in coordinate.

8. Bone landmarks:

In the following setting, two kinds of bone landmarks were employed: one set from the finely scanned MRI which was used to determine the bone geometry, and the other was from the motion scans recording the forearm rotation.

(1) For the fine scans the pertinent osseous features were used as landmarks on the radius and ulna, which was digitized according to xyz coordinates from axial images as shown in Fig. 3.6 and Fig. 3.7. These landmarks denote the ulnar fovea (UF), the center of ulnar head (COUH) at the distal radioulnar joint (DRUJ), and the center of radial head (CORH) at the proximal radioulnar joint (PRUJ), respectively. All of them were manually identified by using the ImageJ tool.

The slice location of DRUJ was identified as the most distal axial slice with the first complete and continuous cortical outline of the ulnar head, containing the visible ulnar fovea while it was viewed in the direction from distal to proximal. The location of UF was then defined from this slice by taking the center point of the ulnar fovea pit. Thereafter, COUH was also derived from the same slice. As shown in (Fig. 3.6), the image in the middle met this criterion. On this image the digitized position of UF, indicated as the red dot, could be distinguished. Since on the right image UF appeared obscured by the base of the ulnar styloid and became not distinct any longer, it was not applicable for the analysis. The center of ulnar head (COUH) was semi-automatically digitized as the red circle with cross by using the ImageJ tool.

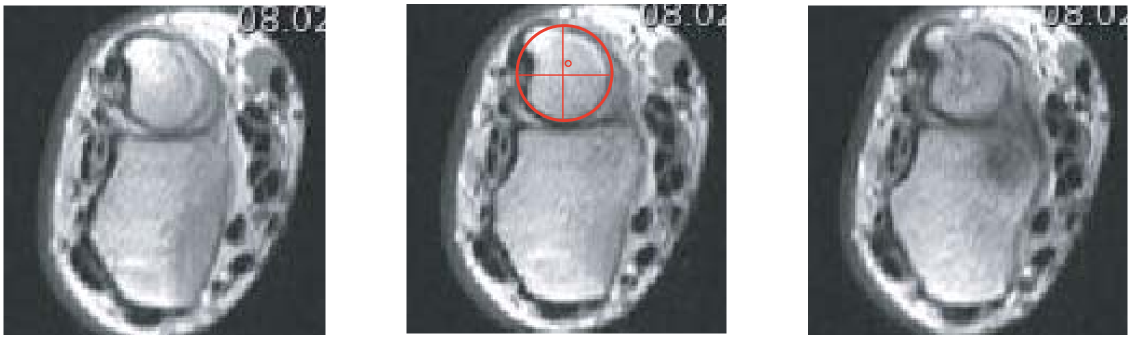

Fig. 3.6: Axial images through the distal radioulnar joint (DRUJ).

The location of PRUJ slice was determined as the axial slice containing the largest area of the radial head, as shown in Fig. 3.7. In the axial images through the proximal radioulnar joint, the image in the middle showed the largest visible cross-sectional area of the radial head, therefore it was taken as PRUJ slice. The CORH was then determined from the same slice, and was semi-automatically digitized (red circle with cross) by using the ImageJ tool.

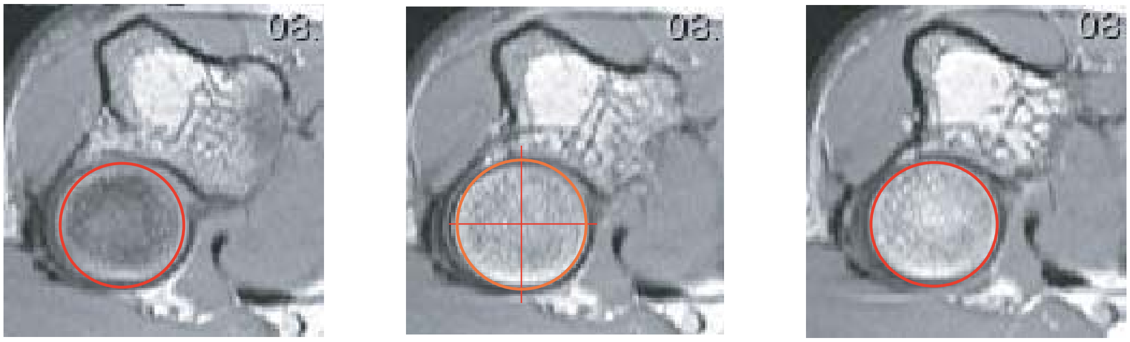

Fig. 3.7: Axial images through the proximal radioulnar joint (PRUJ).

(2) The second bone landmark was the bone marrow center, which was recognized from the cross-section slices of bone radius and ulna in motion scans. As shown in Fig. 3.8, the bone marrows of ulna and radius could be differentiated from cortical bone due to their different gray shading: cortical bone tissue shows low signal intensity (black) while bone marrow shows high intensity (gray). In this study, the characteristic curves of the bones were associated to the centroids of the bone marrow cross sections, and thereafter an automatic segmentation program was used to recognize the bone contours and their centroid position. This process will be explained in Section **3.2**.

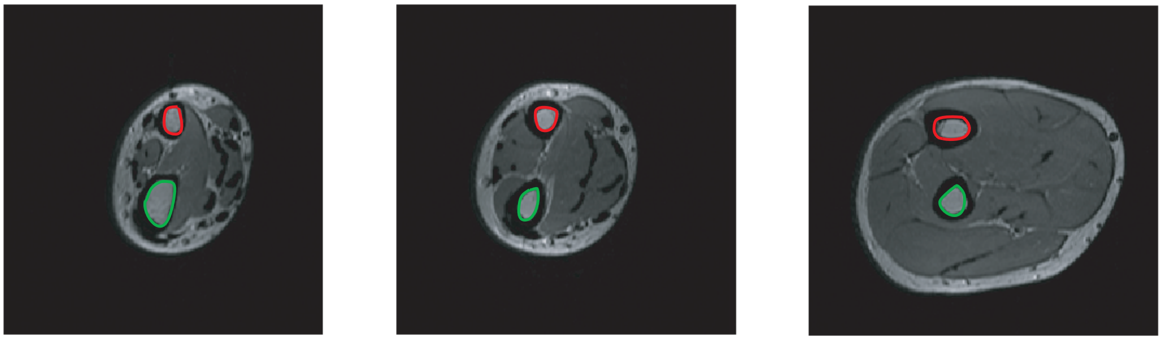

Fig. 3.8: Recognized bone marrows (ulna (red) in upper, radius (green) in lower).

3.2 Forearm bone segmentation

As known, in the surgical planning information of geometry and functional parameters of the patient’s bone are highly valuable. In terms of reducing the workload of the surgeons, an automatic medical image analysis can become a very important tool. However, such a tool is difficult to be realized because of the inherent limitations of the medical images, such as the limited grey level resolution, bad image contrast and image noise etc. Except that, human tissues's complex structure limits the capability of automatic medical image analysis method as well.

This section describes the process to segment the forearm bones between the proximal humerus head and distal wrist portion on MRI. In this process, the position of point clouds of the bone contour and their geometric centers were the first issue to be addressed. Subsequently, the segmented 3D object was used to match the measured forearm motions, and the distance between these two bones was further investigated.

3.2.1 Segmentation overview

The set of segmentation methods presented in this study was developed for the human gait analysis, and the bone geometry represented as triangular meshes was acquired by using a segmentation algorithm based on gray scale [51]. The segmentation program used DICOM MRI images as inputs, thresholding and region growing to process the analysis to extract the functional parameters. After the 3D reconstruction, text files were generated as outputs. Fig. 3.9 shows an overview of the processing flow of the whole segmentation procedure.

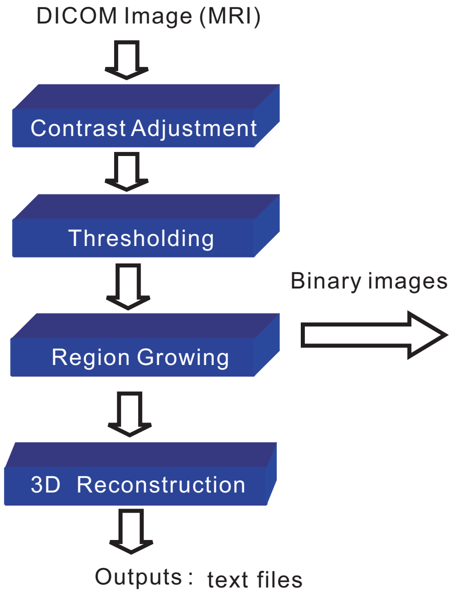

Fig. 3.9: Segmentation processing flow.

3.2.2 Processing

A library named DCMTK was used to read the DICOM images. The library loads all the DICOM images to memory, reads the head of DICOM to get the coordinates of each image center, voxel size and patient name, and then re-sorts all images based on the coordinate of each image center. In order to obtain an optimal binary image with bones as foreground and other tissues as background, the contrast of the DICOM image was adjusted. Here, in order to make the grey level of bone structures more homogenous, the Gauss filter and median filter were used to sieve out the noise in the image.

For thresholding, two threshold values were set: one for the background and the other for the bones. Hereby, since the illumination varies in different sections of the body, the thresholds are section dependent.

In the binary images, bones were presented in black color and the other tissues were in white. However, since some soft tissues in the MRI images had the same grey level as bones, after thresholding, the black region on these binary images contained not only bones but also some small soft tissues. Therefore, after the floodfill method was used to take out the background of the image, some tissues were still left on the image. Region growing was run through the whole MRI images to eliminate these tissues.

Fig. 3.10 shows an example of the process. The left image is an original MRI image, the middle one is the binary image after thresholding process and the right one is after region growing process. It can be seen clearly on the middle image that some tissues are also black and stay on the image after the thread holding process, but disappear after the region growing process.

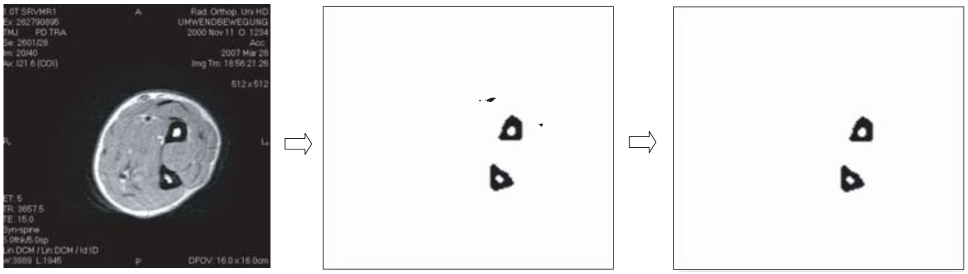

original MRI images after thresholding after region growing

Fig. 3.10: MRI image processing.

3.2.3 User application

The user interactive interface was developed for the visualisation of 2D segmentation and the following 3D reconstruction. This interface is based on C++, QT and some special libraries, such as OpenCV for image processing, DCMTK for DICOM reading, and VTK for 3D reconstruction.

As shown in Fig. 3.11, series of MRI images could be loaded into the window on the left side by clicking the option *'Load'*. Images could be worked one by one by scrolling the bar, with the slice number shown as the *'Current'*. On each image, the resolution of bone structures could be optimized via adjusting the parameter slider *'ContrastH'* or *'ContrastL'*. Then the region of bone of interest could be highlighted with red color by choosing the parameters for *'Backgroud'*, *'Low Threshold'* and *'High Threshold'*. As discussed above, due to the similar grey level of some soft tissues as bones, they also had red color. Therefore, in the next action, *'Seeds'* were set manually by clicking the mouse on some position of the bone, and the optimal value was used to remove those noise-bringing tissues by *'Region Growing'*.

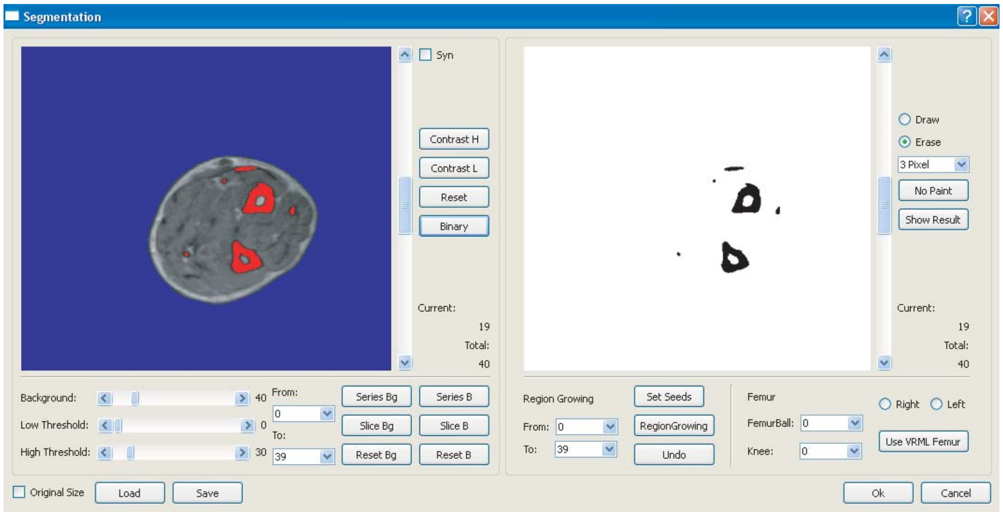

3 Pixel

Current: 19
Total: 40

Current: 19
Total: 40

Background: 40
Low Threshold: 0
High Threshold: 30
From: 0
To: 39

From: 0
To: 39

FemurBall: 0
Knee: 0

Fig. 3.11: User interface of bone image segmentation window. The left window shows the original DICOM images and the preview of thresholding result. The right window is the working area for region growing.

Fig. 3.12 shows the result window after choosing *'Show Results'*. The window on the left side shows both the DICOM image and the segmentation result, and the right side shows the segmentation result individually.

The binary image in BMP format is then loaded in the 3D reconstruction interface. As shown

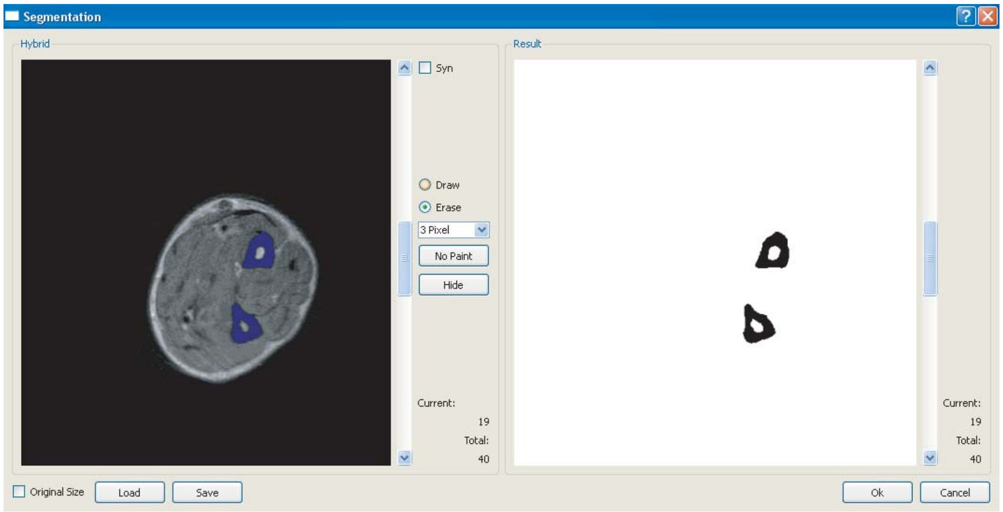

Fig. 3.12: User interface of bone segmentation result window.

in Fig. 3.13, there are two options to realize the reconstruction: iso-surface and delaunary. The Iso-surface method uses binary BMP images as inputs. It connects the points having the same grey level on each adjacent pair of images, and thus a surface is generated based on these polygon curves. The delaunary method allocates the 3D coordinates of the edges in the binary images. From the voxel size, the 2D coordinates in pixel and the images' index, 3D object is produced.

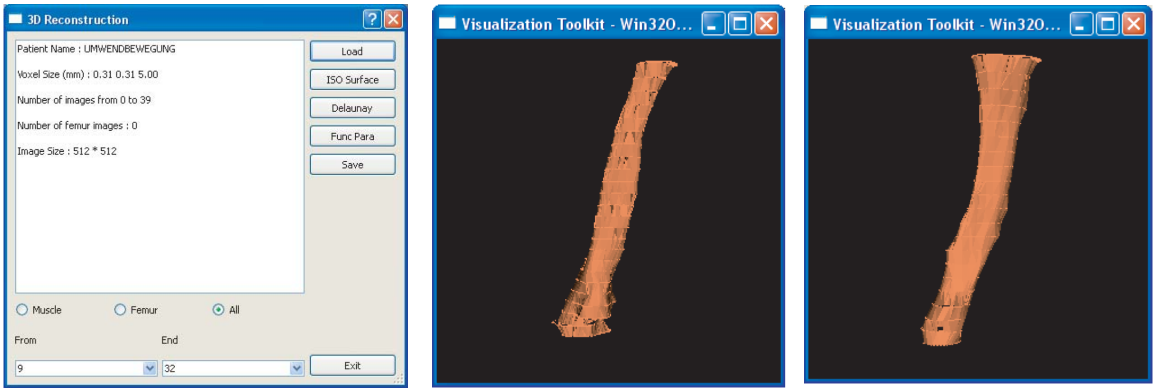

Patient Name : UMWENDBEWEGUNG
Voxel Size (mm) : 0.31 0.31 5.00
Number of images from 0 to 39
Number of femur images : 0
Image Size : 512 * 512
○ Muscle ○ Femur ● All
From 9
End 32

DAT file reconstructed bone ulna reconstructed bone radius

Fig. 3.13: User interface of 3D Reconstruction using the delaunary method.

The forearm bones segmented from the series of fine MRI scans using the delaunary method are displayed at the left side of Fig. 3.14 and the derived 3D reconstruction is shown at the right side. The spherical yellow ball represents the center of radius head. This patient-based specific bone geometry was applied in the further forearm motion study.

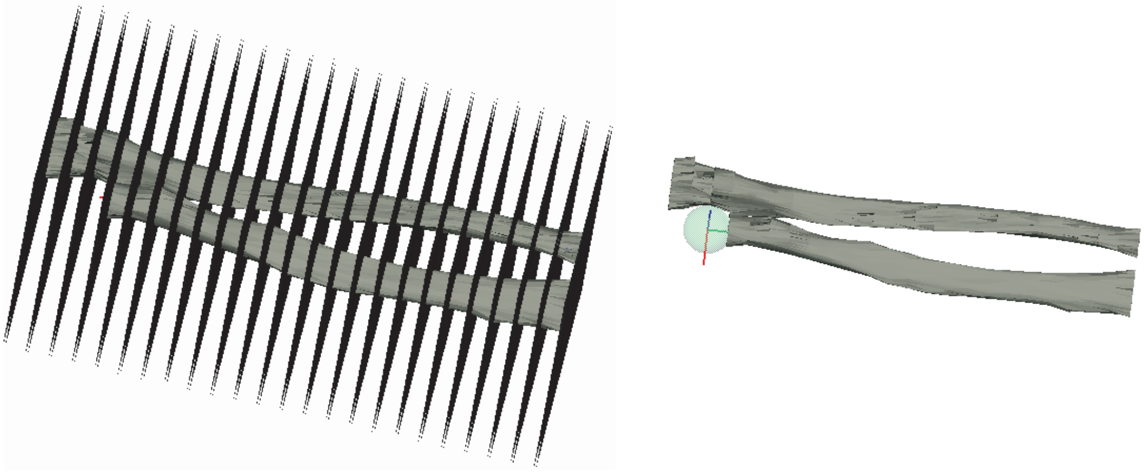

Fig. 3.14: 3D presentation of the segmented bones with MRI.

3.2.4 Segmentation accuracy

Since the change of bone contour along the forearm is one important parameter, a high segmentation accuracy is required. In an effort to check the degree of accuracy of the automatic segmentation, its results were compared with functional parameters which were manually specified by considering the bone area and contour's center respectively. Fig. 3.15(a) is the original MRI. Fig. 3.15(b) shows the bone contours recognized manually (red), automatically (black) and the overlap of these two, from left to right, respectively. The overlap reached 96%. The high accuracy proves the applicability of the automatic segmentation method.

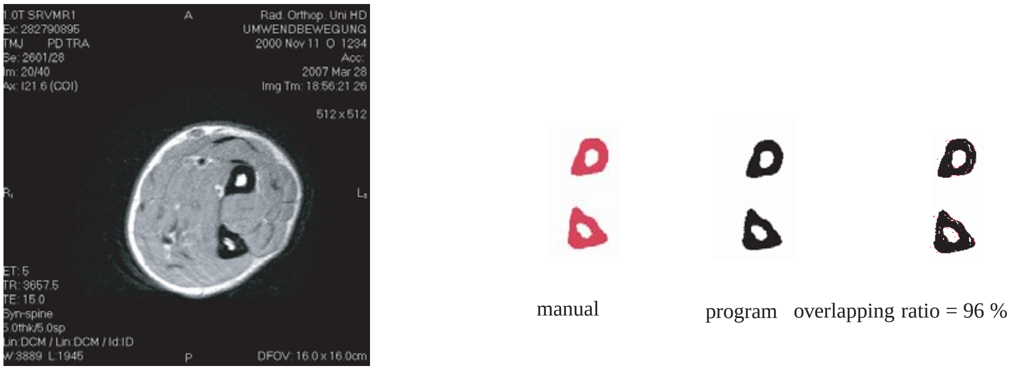

(a) original MRI image

(b) recognized bone cross section

Fig. 3.15: Matching of bone contour by the automatic and manual method.

The details of the comparisons on bone areas and center positions for ulna and radius are shown in Table 3.3 and Table 3.4.

Table 3.3: A comparison of the automatic method and manual procedure for extracting the bone area.

	Manual setting (mm^2)	Automatic method (mm^2)	Deviation (mm^2)	Ratio (%)
Bone ulna area	110.547	112.631	2.084	97.2%
Bone radius area	123.112	125.784	2.672	96.1%

Table 3.4: A comparison of the automatic method and manual procedure for extracting the bone center.

	Manual setting (mm)	Automatic method (mm)	Deviation (mm)
Bone ulna center	(-101.687, -87.308)	(-101.342, -87.767)	0.574
Bone radius center	(-72.428, -98.259)	(-72.684, -98.881)	0.655

3.3 Model parameter fitting

The geometric and elastic parameters of the surrogate mechanism, such as the link length and spring coefficient, cannot be directly determined from the image data. It is necessary to have a fitting process to optimize the mechanism parameters such that the computed results are consistent with the measured values. In this section, a proposed fitting procedure to analyze MRI slices at different rotational configurations is described.

3.3.1 Measured bone marrow centroid

As shown in the example MRI slice in Fig. 3.16, the bone marrows of both ulna and radius can be differentiated from the cortical bone according to their different gray level. Cortical bones show comparatively low signal intensities (black) and bone marrows show relatively higher intensities (gray). The interosseous membrane of the forearm appears is recognizable as thin dark line with low signal intensity.

In image analysis, as described in Section **3.2**, the bone contour of interest was recognized and the position of the bone marrow centroid with respect to the body-fixed frame was obtained. Here, the notation ${}^{i}_{j}\underline{b}_{b}$ denotes a vector from the origin of frame $\mathcal{K}_j$ to the origin of frame $\mathcal{K}_b$ in coordinates of frame $\mathcal{K}_i$. ${}^{i}\mathbf{R}_b$ denotes the orthogonal rotation matrix transforming coordinates with respect to frame $\mathcal{K}_b$ to coordinates with respect to $\mathcal{K}_i$ (here is $\mathcal{K}_0$).

1. The upper left point P_0 is defined as the origin of the body-fixed frame K_b, and $\underline{e}_x$ and $\underline{e}_y$ as the unit vectors spanning the slice plane. These geometric entities define the

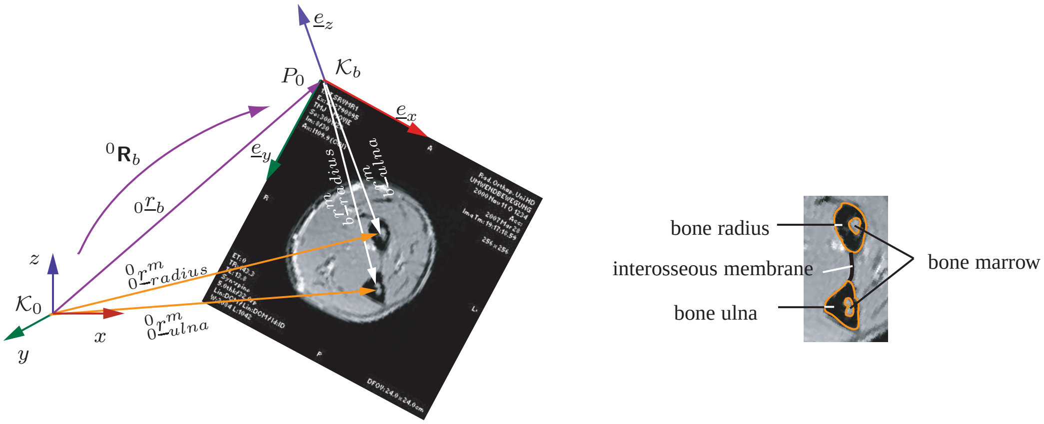

Fig. 3.16: Coordinate transfer.

image position and orientation in DICOM's patient coordinate.

2. The location of the measured centroid of bone radius and ulna in the body-fixed frame are presented as ${}_{b}\underline{r}^{m}_{radius}$ and ${}_{b}\underline{r}^{m}_{ulna}$, where m means measured, and the additional included index $ulna$ or $radius$ defines the corresponding slice for bone ulna and radius, respectively.

3. The position of the bone marrow centroid can be further transformed into the inertial frame K_0, where MRI data is collected, by a transformation matrix ${}^{0}\mathbf{R}_b$ given as

$$ {}^{0}\underline{e}_z = {}^{0}\underline{e}_x \times {}^{0}\underline{e}_y \quad , \tag{3.1}$$

$$ {}^{0}R_b = [{}^{0}e_x, {}^{0}e_y, {}^{0}e_z] \quad . \tag{3.2}$$

4. Series of corresponding vectors ${}^{0}_{0}\underline{r}^{m}_{radius}$ and ${}^{0}_{0}\underline{r}^{m}_{ulna}$ which point to the bone marrow centroids of radius and ulna from discrete MRI slices are presented in the MRI reference coordinate frame by the affine transformations.

$$ {}^{0}_{0}\underline{r}^{m}_{radius} = {}_{0}\underline{r}_b + {}^{0}R_b \cdot {}_{b}\underline{r}^{m}_{radius} \quad , \tag{3.3}$$

$$ {}^{0}_{0}\underline{r}^{m}_{ulna} = {}_{0}\underline{r}_b + {}^{0}R_b \cdot {}_{b}\underline{r}^{m}_{ulna} \quad . \tag{3.4}$$

5. The connection of each pair of adjacent marrow centroids forms a polygon line, termed here as "measured skeleton line" (Fig. 3.17).

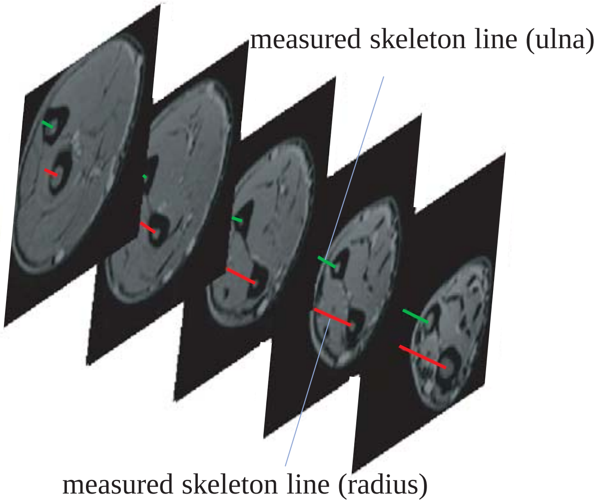

Fig. 3.17: Measured skeleton lines with MRI slices.

3.3.2 Computed bone marrow centroid

Based on the surrogate mechanism model, the vectors which point to the bone marrow centroids from MRI slices were computed. The polygon line connecting the computed points of the bone marrow centroids on radius or ulna is named as "computed skeleton line" (Fig. 3.18).

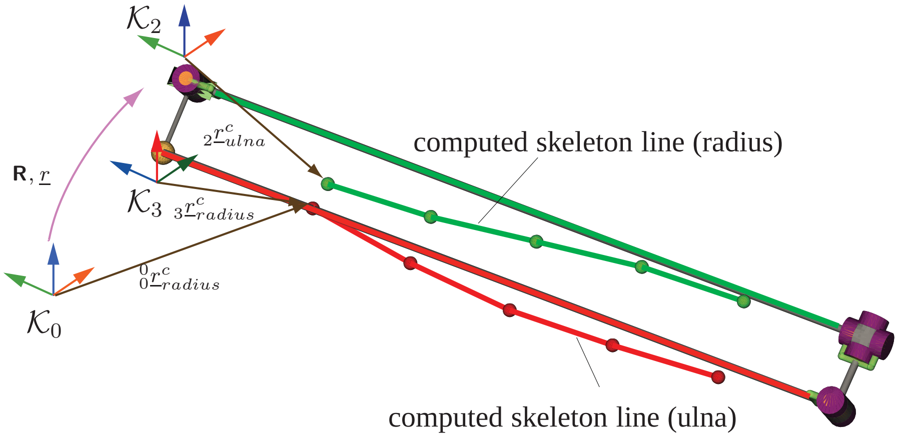

Fig. 3.18: Computed skeleton line with surrogate mechanism.

Hereby, the following procedure is applied:

1. The position vectors of the bone marrow centroids are fixed to the link ulna and radius in the local coordinate of K_2 and K_3, respectively. $\mathbf{R}$ and $\underline{r}$ denote the location of the surrogate mechanism in the MRI reference frame.

2. The location of the computed positions of the bone marrow centroids ${}_{2}\underline{r}^{c}_{ulna}$ and ${}_{3}\underline{r}^{c}_{radius}$ are obtained by a self-calibrating procedure for the determination of the centroid points of the forearm bones at a set of scan slices. This procedure will be detailed in Section **3.3.4**.

3. The computed vectors in the respective body-fixed frame are then expressed in the reference frame K_0 as ${}^{0}_{0}\underline{r}^{c}_{ulna}$ and ${}^{0}_{0}\underline{r}^{c}_{radius}$, by using the corresponding transformation $\mathbf{R}$ and $\underline{r}$.

The computed positions of bone marrow centers depend on the model parameters (link length, spring coefficient), as well as the location of the mechanism ($\mathbf{R}$ and $\underline{r}$).

3.3.3 Parameter fitting principle

In the surrogate model, the bone is regarded as a polygon line with a series of discrete marrow centroid points along the forearm. During the fitting process, the curve connecting the measured/computed centroids of the bone marrow cross sections is generated and named as the measured/computed skeleton line. When the forearm rotates, the centroid points change their spatial positions. The model parameters are then optimized such that square error between the measured and computed skeleton line is minimal over all positions. To calculate the square error, the inertial frame $\mathcal{K}_0$ is introduced as the global home system where MRI data is collected (Fig. 3.19). The elbow Frame $\mathcal{K}_1$ may move with respect to the inertial frame from measurement to measurement with corresponding radius vector ${}_{0}\underline{r}_{1}$ and relative rotation matrix ${}^{0}\mathbf{R}_{1}$. The frames $\mathcal{K}_2$ (ulna) and $\mathcal{K}_3$ (radius) are bone-fixed and are placed at the origin of the corresponding links.

The model fitting procedure is:

1. Let $\underline{r}^{m}_{i,j}$ denote the radius vector to the measured centroid at the j-th slice of the i-th measurement (corresponding to a pro-/supination angle).

2. Let $\underline{r}^{c}_{i,j}$ denote the corresponding computed radius vector to the same target point.

3. Both vectors are assumed to be decomposed in $\mathcal{K}_0$.

4. An additional index U or R is included for denoting the corresponding slices for the ulna or radius bones, respectively.

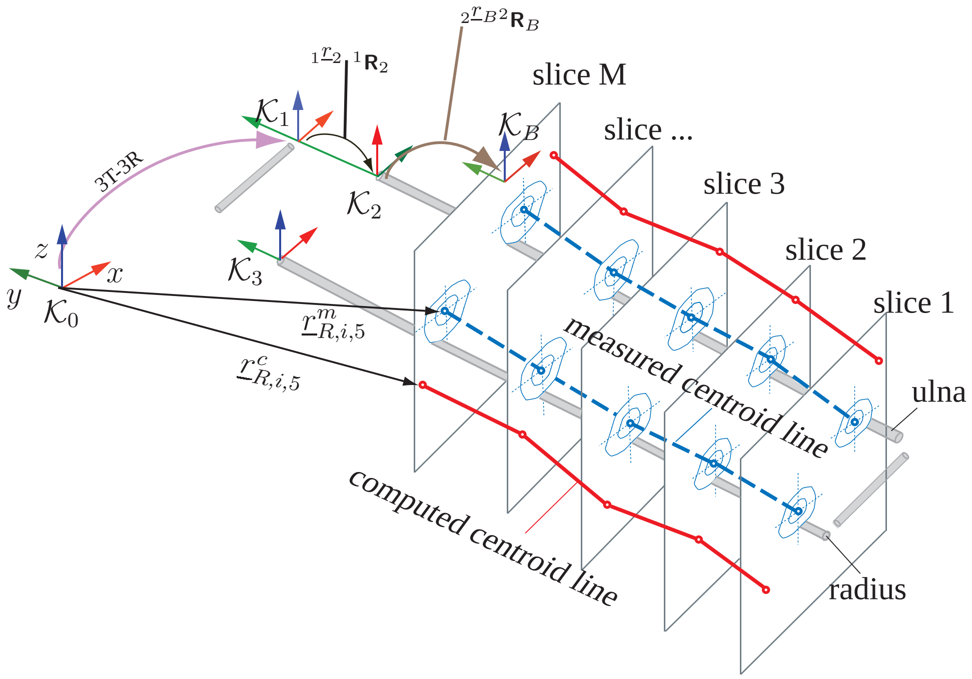

Fig. 3.19: Computed and measured bone marrow centroid line.

5. The minimization target is then

$$\underset{\underline{x}}{min} : \sum_{i=1}^{N}\sum_{j=1}^{M}\{||\,\underline{r}^m_{U,i,j} - \underline{r}^c_{U,i,j}\,||^2 + ||\,\underline{r}^m_{R,i,j} - \underline{r}^c_{R,i,j}\,||^2\} \tag{3.5}$$

In the minimization, design variables $\underline{x}$ are composed of

1. the mechanism kinetostatic parameters r_1,r_2,r_3,r_4,c_s, c_ϑ (Fig. 2.7)
2. the rigid-body motion of the elbow, for each measurement, represented by three translations x_0^j, y_0^j, z_0^j and three rotations $\chi_1^j, \chi_2^j, \chi_3^j$ (i.e. $3T-3R$)
3. the relative location of bone geometry frame $\mathcal{K}_B$ with respect to the link reference frame, involving three constant translations, $\kappa_1, \kappa_2, \kappa_3$ and three constant rotations $\epsilon_1, \epsilon_2, \epsilon_3$ for each bone(e.g. ${}_2\underline{r}_B$, ${}^2\mathbf{R}_B$)
4. the pro-/supination angle $(\varphi)^j$, which rotates the mechanism to the optimal configuration.

All design variables must be determined simultaneously, as they are highly coupled. There are thus in total $18 + 7\,N$ design variables for N measurements.

3.3.4 Automatic axial calibration of motion scans along bone axis

While the forearm rotates, it is unlikely that changes of the forearm position from measurement to measurement will not occur when the measurement is performed in vivo. In order to compensate this variability, a self-calibrating procedure is developed for determining the location of forearm bones at a series of scan slices.

3.3.4.1 Bone cross-section's variability

As already mentioned in Section **3.1**, a fine MRI scan with a set of slices is performed to provide the information of smooth bone geometry, and also as a reference for the motion scans. The fine scan shows that the shape and cross-sectional area of bone ulna and radius, as well as the distance between them vary along the bone axis (Fig. 3.20). Hereby, the following features can be recognized:

1. Change of the bone shape:
   The proximal end of bone radius is smaller than its distal end. The shape of bone radius changes from a circular cylinder to a prismatic-triangular shape, somewhat concave towards the ulna, and then becomes broader distally, and quadrilateral in cross section [41].

   The ulna is more irregular in shape at the proximal end. Its cross section then changes from triangular in the middle segment to circular in the distal third section and then irregular again [41].

2. Size of the cross-sectional area:
   By using automatic segmentation, the area of each bone contour (inner and outer) at a slice position can be directly calculated. An example of the measured profile of cross-sectional areas is shown in Fig. 3.21. They are ploted based on data from the fine scan. On the figure the solid red line represents the area of the outer cortical bone contour and the blue line represent the inner cortical bone area. Obviously, the varying of contour areas is irregular, and cannot be interpreted as a simple increasing or decreasing along the bone axis.

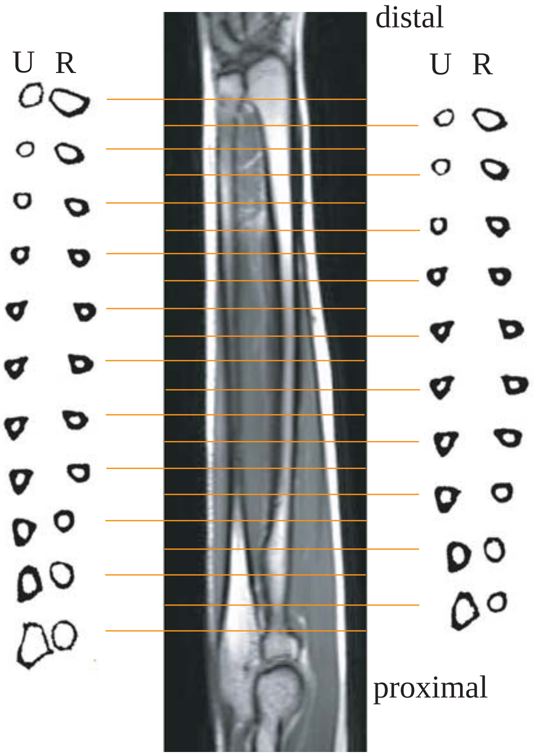

Fig. 3.20: Scheme of the cross-section change of the radius and ulna along forearm.

3. Distance between ulna and radius:
   The distance between ulna and radius also varies along the bone axis, which is relatively shorter at the proximal side, larger at the middle, and again shorter at the distal side. During the forearm rotational motion, the radius crosses over the ulna, indicating that the distance also depends on the pro-/supination angle. The detailed analysis of the complex distance change will be described in Chapter **4**.

The cross-sectional area of the bones can now be utilized in the calibration, since its change along the forearm is smooth and significant.

3.3.4.2 Axial calibration

Since a change of forearm location in the in-vivo measurement is not avoidable, a self-calibrating procedure is proposed for the determination of the bone marrow centroids of forearm bones at a series of scan slices. In such a procedure, an offset s^* needs to be determined to facilitate the synchronization of the profile of measured cross-sectional areas at motion slices with the interpolated contours of cross-sectional area achieved from fine scans. This is conducted by using the quadratic error minimization [27].

As described above, the change of the cross-sectional area is smooth and significant (Fig. 3.21), and can thus be used for automatic calibration along the axial direction. Calibration along transversal direction is easily accomplished by the optimization procedure described in Section **3.3.3**.

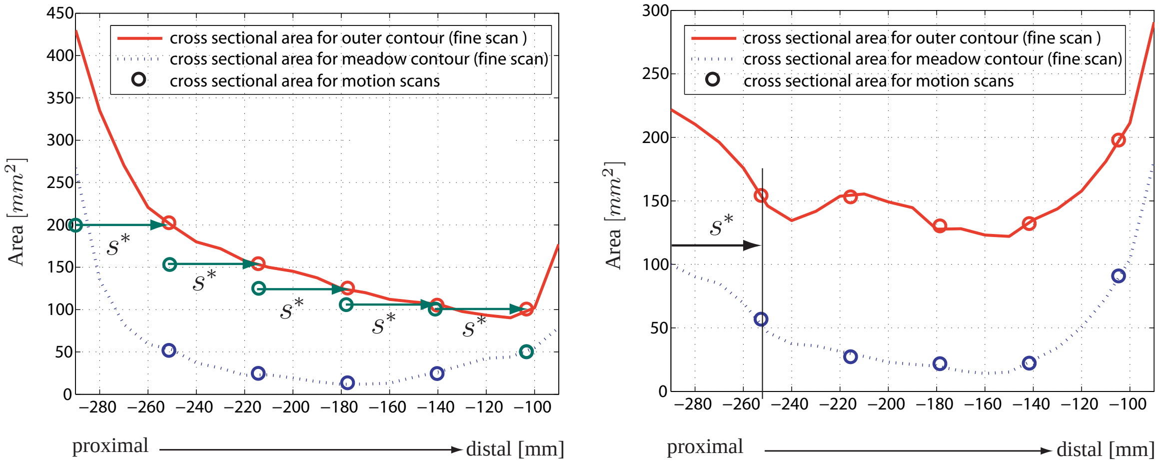

a) ulna

b) radius

Fig. 3.21: Cross-sectional area of ulna and radius (supination angle $\varphi = 90°$).

The axial calibration procedure consists of the following steps:

1. Calculate the cross-sectional area of bone ulna and radius at each slice i of fine MRI scan ($i = 1, 2, 3 \cdots L$, L is the slice number in fine scans), named as $A^s_{U,i}$ and $A^s_{R,i}$. The outer and inner area are plotted verse the axial location as solid red line and dotted blue line shown in Fig. 3.21(a) and (b), respectively.

2. Calculate the cross-sectional area from the measured motion scans, named as $A^m_{U,j}$ and $A^m_{R,j}$, where j is the number of motion scans at defined pro-/supination angle ($j = 1, 2, 3 \cdots M$, M=5 in this study).

3. Extract the constant distance between each two adjacent slices for the motion scan, defined as d_s from the DICOM data base.

4. Assume that the aixal offset of the first slice is s, then the axial location of all slices of the same series are $s_j = s + (j - 1) * d_s, j = 1, 2, 3 \cdots M$.

5. Calculate the interpolated cross-sectional areas $A^{int}_{U,j}$ and $A^{int}_{R,j}$ for the fine scans at the axial locations s_j.

6. Run the quadratic error minimization (3.6) to determine s^*, where the indexes U and R correspond to bone ulna and radius, respectively, so that the cross-sectional areas of the corresponding slices of motion scans match the reference well. It is noted here that s^* should be same for ulna and radius, apart from a possible constant offset, i.e. the offset of ulna and radius is coupled.

$$\overset{min}{s} : \sum_{j=1}^{M} ||A^{m}_{U/R,j} - A^{int}_{U/R,j}(s_j)||^2 \tag{3.6}$$

7. Repeate the process 2 to process 6 for the calculation of the offset s^* at a new pro-/supination angle.

8. Once the location of s^* are identified, $s_j = s^* + (j-1) * d_s, (1 \leq j \leq M)$ can be obtained subsequently. Therefore, the bone-fixed coordinates of bone marrow centers can be determined by linear interpolation of the reference bone marrow centroid, and the corresponding bone-fixed vectors ${}^{B}_{B}\underline{\xi}_{i,j}$ are obtained. Referring to Fig. 3.19, the corresponding computed bone marrow centers then become

$$\underline{r}^{c}{}_{i,j} = \underline{r}_{2/3} + {}^{0}\mathbf{R}_{2/3} \, (\, {}^{2/3}_{2/3}\underline{r}_{B}, + {}^{2/3}\mathbf{R}_{B} \, {}^{B}_{B}\underline{\xi}_{i,j} \,) \tag{3.7}$$

where, the indexes 2 and 3 correspond to bone ulna and radius, respectively, and the index B denotes for their corresponding bone reference frame (ulna or radius). The notation ${}^{i}_{i}\underline{b}_{B}$ defines a vector from the origin of frame $\mathcal{K}_i$ to the origin of frame $\mathcal{K}_B$ decomposed in the coordinates of frame $\mathcal{K}_i$. The ${}^{i}\mathbf{R}_{j}$ define the orthogonal rotation matrix transforming coordinates with respect to frame $\mathcal{K}_j$ to coordinates with respect to $\mathcal{K}_i$. Here, ${}^{2/3}_{2/3}\underline{r}_{B}$ and ${}^{2/3}\mathbf{R}_{B}$ are the (unknown) design parameters describing the constant pose of the bone geometry with respect to the corresponding mechanism link.

3.3.5 Geometric and kinetostatic parameter fitting

The model parameters of the surrogate mechanism cannot be determined directly from the image data. A fitting procedure is necessary to optimize the parameters, and thus the computed results coincide with the measured values. This procedure consists of two basic steps:

(1) to obtain initial geometric parameters (link lengths) from medial view of the forearm; (2) to determine the kinetostatic parameters (geometric quantities and stiffness coefficients of the two virtual springs) using the optimization procedure of Eq. (3.5).

3.3.5.1 Geometric initial parameter estimation

The geometric initial parameter estimation is based on a medial MRI scan (Fig. 3.22) and fine cross-sectional MRI scans (Fig. 3.23). The initial model parameters r_1=r_3=l, r_2=r_4=b are estimated from the medial MRI scan with the assumption that the surrogate mechanism is roughly a parallelogram in the supination configuration. The length l is defined as the distance from the proximal point of the radius head to the distal point of the styloid process of ulna. The width b is defined as the largest diameter of the radius head, which can be deduced from medial MRI image (Fig. 3.22). For example, in the case of the Heidelberg measurement, l and b were measured as 252[mm] and 25[mm], respectively.

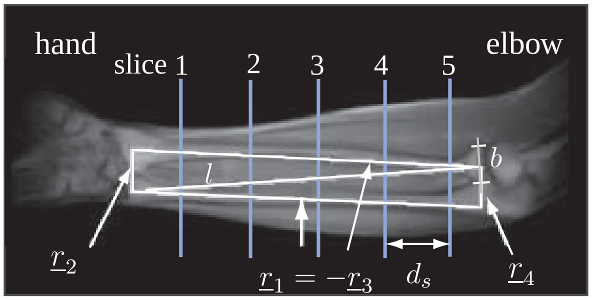

Fig. 3.22: Geometry bone parameters from axial image.

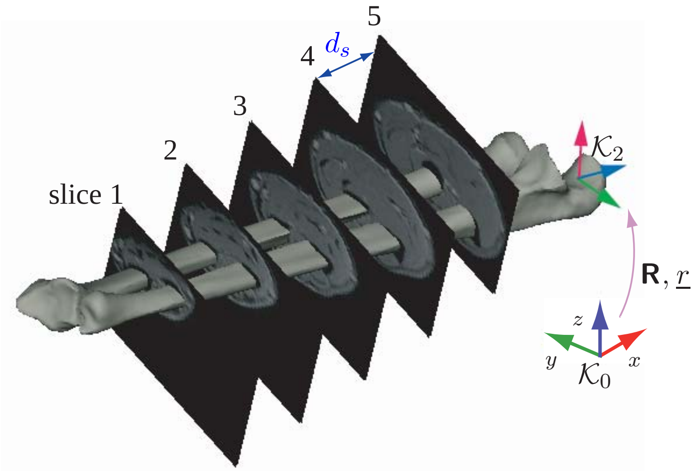

Fig. 3.23: Location of MRI slices for the right arm.

The dimensions of testers's forearms in these two measurements are summarized in Table 3.5.

Table 3.5: Initial measured bone geometry data and slice offsets

	r_1 (mm)	r_3 (mm)	r_2 (mm)	r_4 (mm)	number of slices reference scans	d_r (mm)	number of slices motion scans	d_s (mm)
Heidelberg	252	252	25	25	42	10	5	37
Essen	246	246	23	23	94	3	7	36

3.3.5.2 Kinetostatic parameter fitting

The database for the fitting are series of MRI slices, which consist of scanning bone cross sections of the forearm at different pro-/supination angles $\varphi_1, \ldots, \varphi_N$. For each pro-/supination angle, a reduced set of MRI slices $S_1, \ldots, S_M$ (M=5/7) is scanned as described in Section **3.1**. Fig. 3.23 presents the location of the slices from motion scans along the forearm axial direction, with the defined space d_s between each two adjacent slices.

Taking the Heidelberg measurement as an example, the reference scan contained 42 slices with 10mm distance to each other, and the motion scans contained 5 slices with 37mm distance. The hand rotated from vertical palm (φ= 0°) to supination (φ=90°) in two steps with 45° angle in each step, and then to pronation (φ=-90°) in the same way. The angles were prescribed by the aforementioned device featuring a rotatable handle on a box placed at the end of the MRI tube. The device can produce, via a Bungee cord, a resisting torque while operating the handle. The three runs were (1) no resistive torque, (2) torque of 4.2Nm against pronation, and (3) torque of 4.2Nm against supination.

Fig. 3.24 shows the resulting MRI images of one run (without torque) from the perspective of the wrist. The rows from top to bottom display the images of the chosen slices along the forearm length from proximal elbow portion to distal wrist portion, and the columns from left to right show the cross sections at maximum supination, 45° supination, neutral, 45° pronation and maximum pronation. The two small circles represent the radius (red) and ulna (green) respectively, and the grey parts inside the circle are bone marrows. From these images, the relative rotation of the radius around the ulna can be observed.

The same phenomenon were also observed in the MRI slices with ±4.2Nm torque, shown in Fig. 3.25 and Fig. 3.26, respectively.

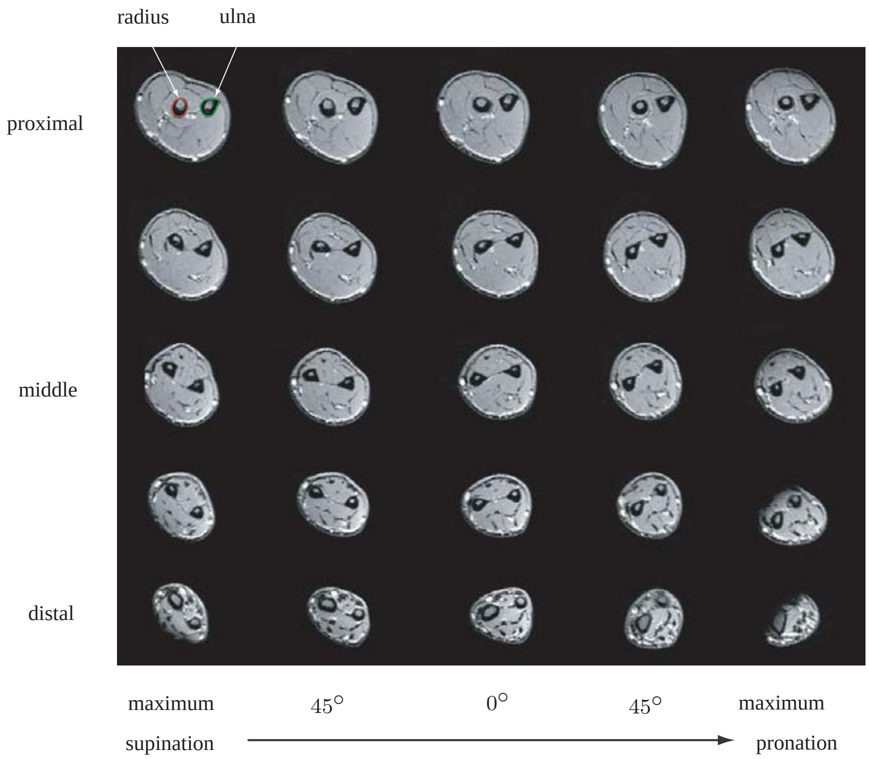

Fig. 3.24: MRI slices measured without torque (perspective view of the wrist).

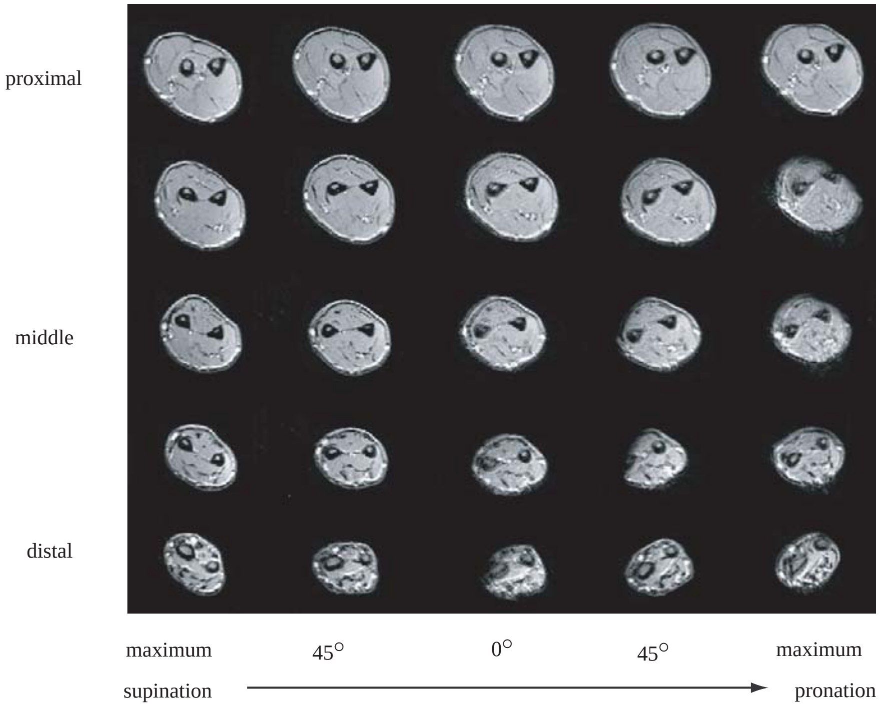

Fig. 3.25: MRI slices measured with resisted pronation torque (perspective view of the wrist).

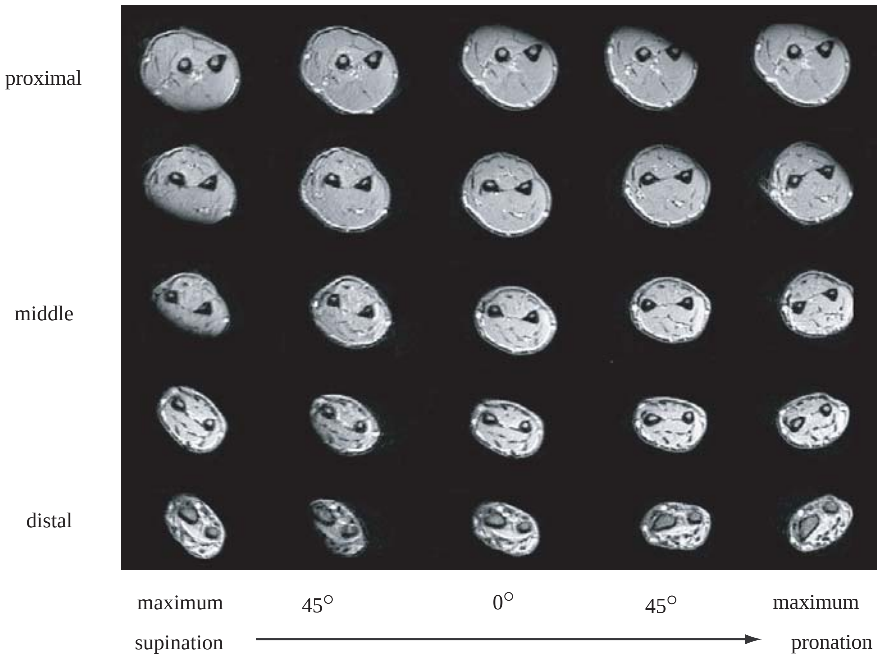

Fig. 3.26: MRI slices measured with resisted supination torque (perspective view of the wrist).

To determine the axial displacement of ulna, Weinberg et al. used the in-vitro measurements on a cadaveric probe to measure the axial displacement at the humero-ulnar articulation as a function of pro- and supination [24]. A CCD camera was used to record the opening at the humero-ulnar joint from ventral view for three positions under loading conditions (no loading, varus stress and valgus stress). In this work, the dislocation was not determined by such in-vitro measurements, but by fitting in-vivo data under different physiologic loading conditions (Fig. 3.31). It is necessary to note that the opening at the humero-ulnar joint, i.e. the gap from ventral view, does not represent the axial displacement s at the humero-ulnar joint directly, but comprises also an additional displacement of the edge of lateral swaying rotation due to the offset between the bone axis and the edge of the trochleus (Fig. 3.27). Hence, the observed gap is $\overline{s} = -s + l_o \sin\vartheta + \overline{s}_0$, where $\overline{s}_0$ is a fixed constant relating the model variable s with the measured gap through a fixed offset [24].

3.4 Simulation results

Based on these measurements, the optimization procedure described in Eq. (3.5) was carried out with the built-in Matlab function `fmincon`, and thus the values for c_s and c_ϑ were

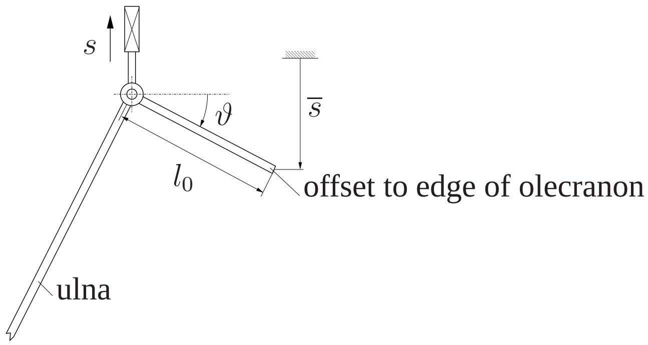

Fig. 3.27: Opening of the gap (pronation).

determined. The typical computational time for one optimization run was 30 minutes in this study.

`Fmincon` stops when the predicted change in the objective function is less than the default value of the function tolerance and constraints are satisfied to within the default value of the constraint tolerance. The development of cost function over iteration steps are plotted, by taking the Heidelberg measurement as an example, for fixed-axis model and 2DOF model in Fig. 3.28. It can be observed that in both model the cost function decreases by 80% from its initial value after the first 20 iterations and becomes already quite stable after 30 iteration steps. The cost value in 2DOF model is much less than that in fixed-axis model, which proves that 2DOF model has a better computation match to the measurements.

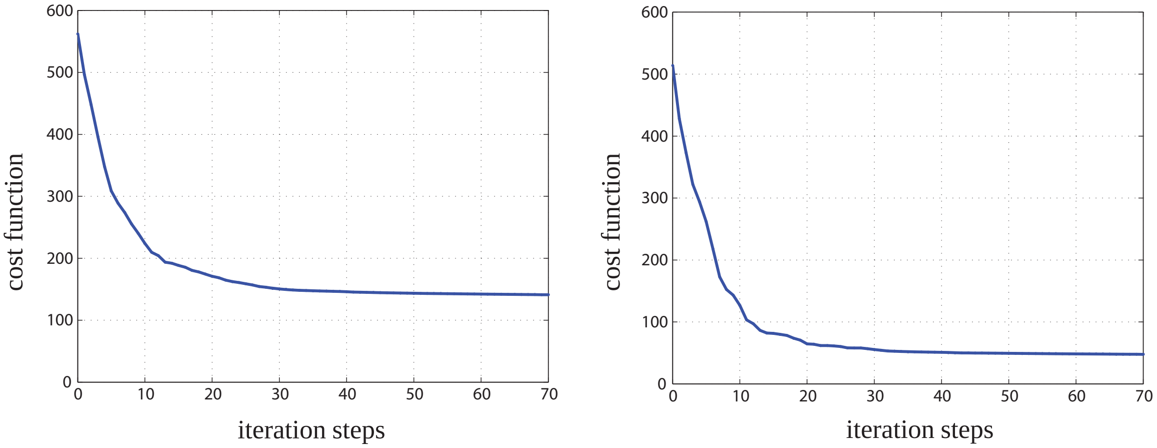

(a) fixed-axis model

(b) 2DOF model

Fig. 3.28: Development of the cost function over the iteration steps.

3.4.1 Numerical data

The measured data obtained from the fine MRI scanning is shown here as a reference. As initial values, the anatomical lengths described in Section **3.3.5.1** were chosen. The subsequent computed results for the cases of no-torque, pron-resist torque and supin-resist torque, are shown in Table 3.6 for Heidelberg measurement, and Table 3.7 for Essen measurement.

Table 3.6: Identified mechanism dimensions and stiffness coefficients (Heidelberg measurement)

		radius	ulna	elbow	wrist	c_s	c_ϑ	ratio	$\vartheta_{\max}$	$\overline{s}_{\max}$
		(mm)	(mm)	(mm)	(mm)	(N/mm)	(N mm)	c_ϑ/c_s	$(^\circ)$	(mm)
Measured		252	252	25	25	-	-	-	-	-
Computed	without torque	252.13	252.08	24.71	24.07	0.091	19.97	219.45	7.93	0.597
	pron. torque	252.31	252.22	24.82	24.43	0.092	20.32	220.87	7.85	0.605
	supin. torque	252.73	252.54	24.61	24.24	0.094	20.28	215.74	7.83	0.583
	average	252.39	252.28	24.71	24.25	0.092	20.19	218.68	7.87	0.595
	S.D.	0.26	0.21	0.10	0.15	0.002	0.19	2.65	0.05	0.011

Table 3.7: Identified mechanism dimensions and stiffness coefficients (Essen measurement)

		radius	ulna	elbow	wrist	c_s	c_ϑ	ratio	$\vartheta_{\max}$	$\overline{s}_{\max}$
		(mm)	(mm)	(mm)	(mm)	(N/mm)	(N mm)	c_ϑ/c_s	$(^\circ)$	(mm)
Measured		246	246	23	23	-	-	-	-	-
Computed	without torque	246.57	246.31	23.14	22.98	0.131	23.56	179.84	7.98	0.615
	pron. torque	246.82	246.61	23.05	22.87	0.145	25.85	178.28	7.94	0.656
	supin. torque	246.64	246.25	22.74	22.68	0.134	24.48	182.68	8.01	0.662
	average	246.68	246.39	22.97	22.84	0.137	24.63	180.27	7.97	0.644
	S.D.	0.13	0.19	0.21	0.15	0.007	1.15	2.23	0.03	0.025

In both cases the average computed bone length and width are almost identical to the measured values. Moreover, the results show only minor deviations among different torque conditions, which indicates there is no dependency of the mechanism parameters, i.e. the link length and the stiffness of the virtual springs, on the external torque (4.2Nm). Hereby, the presented stiffness coefficients do not represent real absolute values of the stiffnesses induced by the tendon system, but are scaled quantities for the kinetostatic coupling. This scaled value is stable, which demonstrates that only the ratio of these two coefficients is relevant during the fitting of swaying and axial motion of the ulna. Thus, deformations at the humero-ulnar joint (swaying angle ϑ and dislocation $\overline{s}$) are basically decoupled from the external loads. Moreover, the resulting translational dislocation is so small that it does not impair the functionality of the humero-ulnar joint, while allowing the important sway motion of the ulna to take place by approximately 8° at full pronation.

As there are two degrees of freedom in 2DOF model, the distribution of the pronation rotation on the individual relative joint motions is thus not unique. Refering to (2.25c) ($c_\varphi\,(\varphi - \varphi^*\,) = J_\varphi * c_\vartheta * \vartheta$), the control torque $c_\varphi\,(\varphi - \varphi^*\,)$ along the pronation axis is distributed at the relative joint R_ϑ and the prismatic joint P, which are placed at the proximal ulna head in the model. As shown in Fig. 3.29, the distributed torque value $c_\vartheta * \vartheta$ at R_ϑ is plotted in red colour, where the blue curve is the control torque applied at the Hooke joint which is plotted here as a reference. As it can be seen from the figure, the control torque is much smaller than the torque at the elbow, therefore the torque at the elbow does not constrain the motion at the spring.

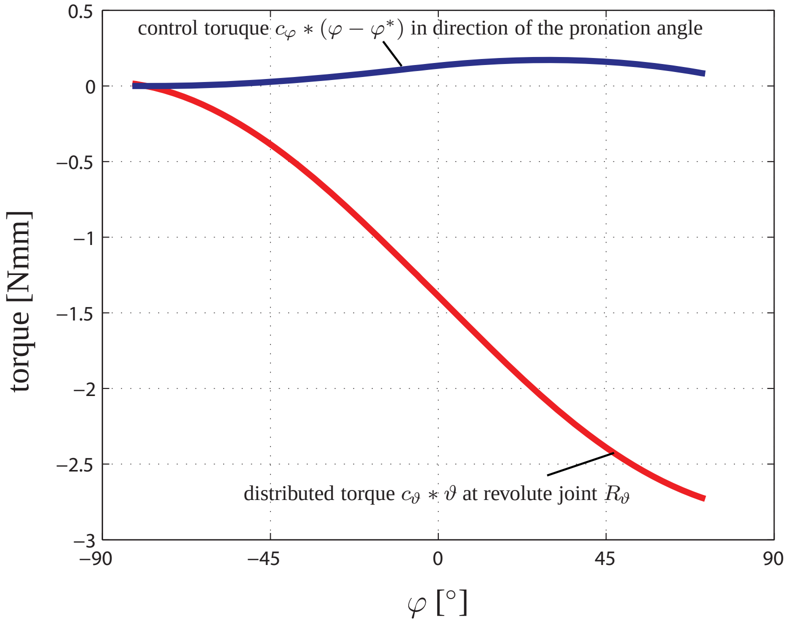

Fig. 3.29: Torque distribution as a function of pro-/supination angle.

The relationship between the stiffness ratio c_ϑ / c_s and rotational angle φ is analyzed by fixing 2DOF mechanism parameter and re-run the rotational motion. As in Fig. 3.30, it is found that the stiffness ratio c_ϑ / c_s is a non-linear equation during the pro- and supination, which deviated from our computed average ratio value 218.68 in a small range ($\leq$3). However, since the deviation is so small, the stiffness ratio can be regarded as a constant value for the whole rotational process for an individual subject.

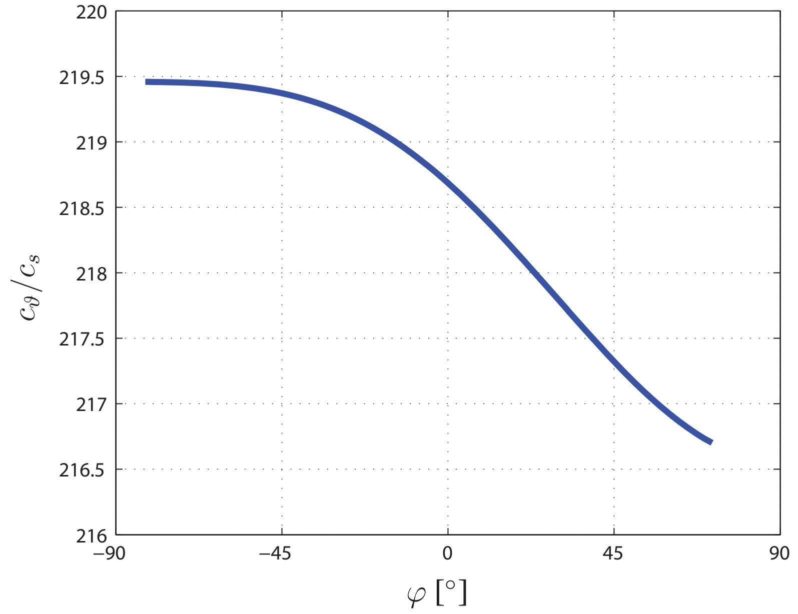

Fig. 3.30: Plot of stiffness ratio c_ϑ/c_s as a function of pro-/supination angle.

3.4.2 Histories of elbow variables as functions of pronation angles

Fig. 3.31 shows the resulting plots for the swaying angle ϑ, the humero-ulnar gap at the trochlea edge $\overline{s}$, the radio-ulnar torsion angle ψ_1 and the aperature angle ψ_2 as a function of the pronation angle φ, respectively. There are three plots on each figure, corresponding to the three loading conditions. As shown in the figure, the maximum supination angles under three torque status are 82°, 78° and 76°, and the maximum pronation angles are 72°, 65°, 67° respectively. These results are consistent with the results from a clinical study performed by Weinberg et al. [52] (supination: [84.4±5.49°], pronation [66.4±7.6°]). Furthermore, it can be observed from the figures that the three curves (without wrist torque (red), pronation-resisted 4.2Nm torque (blue) and supination-resisted 4.2Nm torque (green)) have nearly identical behavior. This fact proves that the lateral swaying and displacement of ulna with respect to humerus have no observable dependency on the outer torque, and the same do the radio-ulna torsion and apertures. In other words, the wrist load has no apparent influence on the forearm kinematics, and the virtual springs at the two degrees of freedom virtually operate like a kinematical coupling between the two degrees of freedom of the surrogate mechanism. Hence, the model is applicable for all cases with realistic wrist torques.

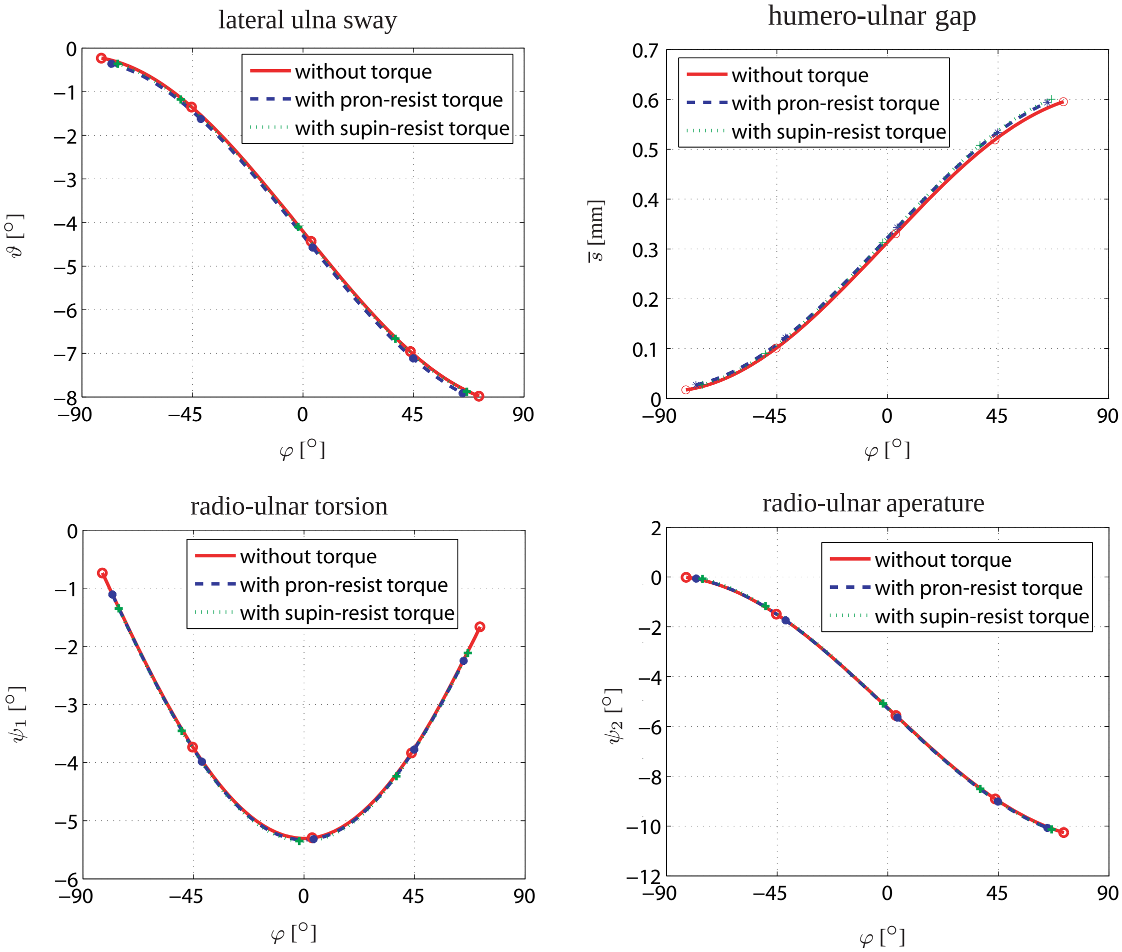

Fig. 3.31: Histories of elbow variables with different load status.

Known from clinical studies [52], the predominant valgus motion in the transverse plane is 7.1° (SD 0.8°, min 6°/max 8°), and the axial dislocation from a cadaveric arm measurement is 0.6mm. Our simulated results agree with these anatomical results very well, e.g.: (1) in the Heidelberg measurement, the amplitude of the lateral sway angle ϑ under different loading status are 7.93°, 7.85°, 7.83°, and the axial gap are 0.597 mm, 0.605 mm, 0.583 mm; (2) in the Essen measurement, the amplitude of the lateral sway angle ϑ under different loading status are 7.98°, 7.94°, 8.01°, and the axial gap are 0.615mm, 0.656mm, 0.662mm. The good coincidence of simulated motions to the anatomical data indicates the reasonability of the surrogate mechanism and the applicability of the simulation approach.

In Fig. 3.32, the resulting swaying angle ϑ is plotted against the humero-ulnar gap at the trochlea edge $\bar{s}$ under different torque conditions. It can be observed there exists an almost linear relationship between them.

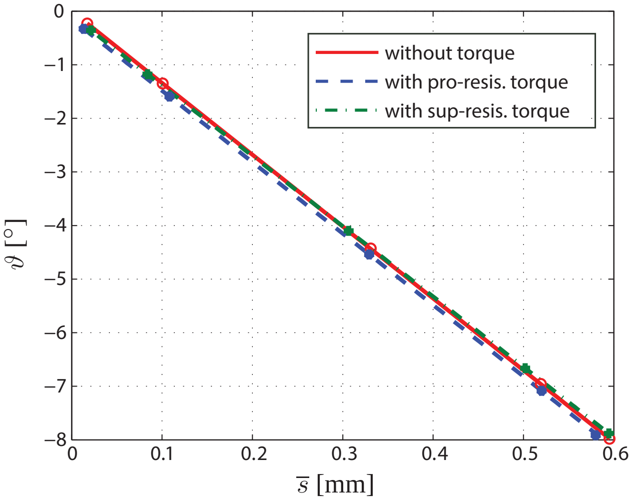

Fig. 3.32: Lateral sway against humeral ulna gap with different load status.

Fig. 3.33 shows the motion of the surrogate model at five rotational positions from supination to pronation, which are respectively colored by blue for sup90°, purple for sup45°, green for neutral, brown for pro45° and red for pro90°. The link representing ulna is highlighted boldly. Here, x-axis pointing laterally towards the radius and the y-axis along the forearm pointing to the ulna styloid, are defined as positive direction. A significant swaying motion of the ulna distal end towards radius side (right) can be observed. Comparetively, at the proximal end, only a delicate axial displacement along y-axis occures. The position of both ends of ulna in this coordinate are listed in Table 3.8 and Table 3.9 for the Heidelberg and Essen measurements, respectively.

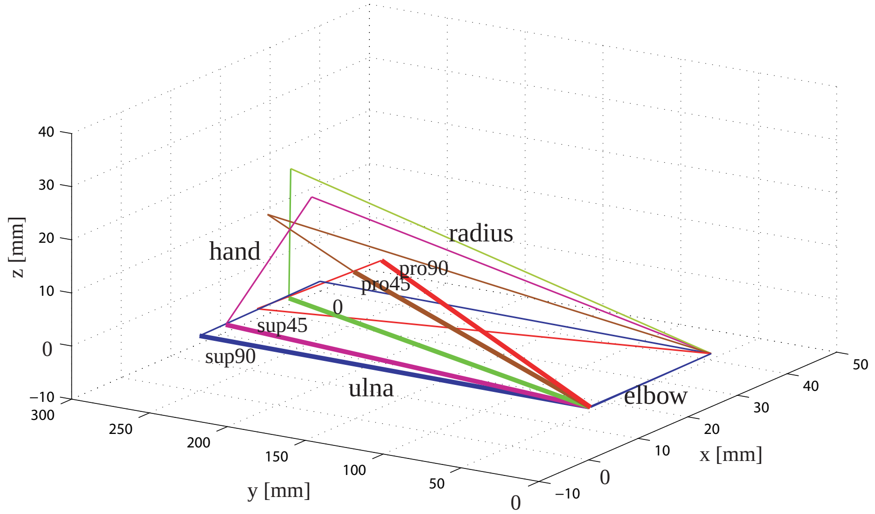

Fig. 3.33: Motion of the forearm mechanism from supination to pronation.

Table 3.8: Identified positions of ulna proximal and distal ends (Heidelberg measurement)

	ulna proximal end	ulna distal end
sup 90 °	(0, 0 ,0)	(0, 252.39, 0)
sup 45°	(0, -0.21, 0)	(6.02, 252.11, 0)
0°	(0, -0.65, 0)	(18.43, 251.07, 0)
pro 45°	(0, -1.09, 0)	(30.98, 249.39, 0)
pro 90°	(0, -1.28, 0)	(36.30, 248.48, 0)

Table 3.9: Identified positions of ulna proximal and distal ends (Essen measurement)

	ulna proximal end	ulna distal end
sup 90 °	(0, 0, 0)	(0, 246.57, 0)
sup 45°	(0, -0.22, 0)	(7.07, 246.25, 0)
0°	(0, -0.60, 0)	(19.00, 245.24, 0)
pro 45°	(0, -0.98, 0)	(31.11, 243.62, 0)
pro 90°	(0, -1.15, 0)	(36.27, 242.74, 0)

To consider the relative motion between ulna and humerus, the instant rotation center of bone ulna relative to humerus is plotted for the Heidelberg and Essen measurements, respectively, as shown in Fig. 3.34. The instant centre of rotation, also called instantaneous centre, is the point in a body undergoing planar movement that has zero velocity at a particular instant of time. In the figure, x-axis points laterally towards the radius, and the y-axis points to the ulna styloid along the forearm. The instant rotation axis is vertical to the x-y plane through each instant center at instant of time. During the complete forearm rotation, the x-axis position of the instantaneous rotation center varies within a large range, especially at sup/pro 65-66 ° for the Heidelberg measurement and 62-63 ° for the Essen measurement. However, its y-axis position deviates only slightly.

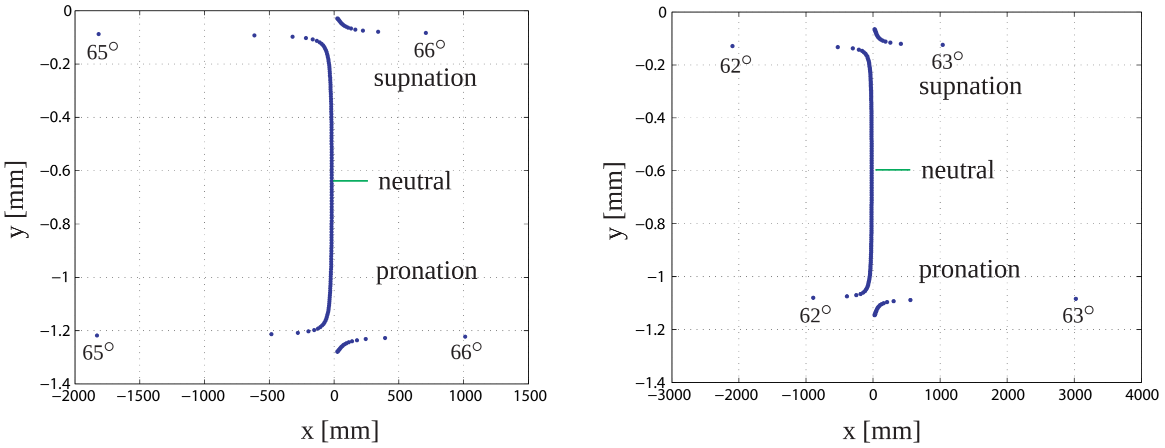

a) Heidelberg measurement

b) Essen measurement

Fig. 3.34: Instant center of roation of bone ulna relative to bone humeurs.

3.4.3 Optimization accuracy

During optimization, the best fitting of computed positions of bone marrow centroids in spatial coordinates to the measured data, is searched. Matching errors for the Heidelberg measurement under three loading conditions are shown in Table 3.10, Table 3.11 and Table 3.12, respectively. Hereby, 50 centroid points are analyzed for each load condition. In the case without torque, 94% points show errors less than 1.5mm, and the maximal error is 1.79mm. Together with the measurements under torque, totally 150 centroid points are processed. In total, 92% points show an error smaller than 1.5mm, and the maximal error among them is less than 2mm.

Table 3.10: Matching errors of bone marrow centroids (without torque) for the Heidelberg measurement

pro-/supination angle φ in ° (identified)	Error between computed and measured marrow centroid (in mm) (without resistive torque)									
	cross-section 1		cross-section 2		cross-section 3		cross-section 4		cross-section 5	
	radius	ulna	radius	ulna	radius	ulna	radius	ulna	radius	ulna
-82	0.15	0.22	0.47	0.30	0.84	0.82	0.83	0.85	0.91	0.68
-45	0.92	0.61	0.35	0.57	0.85	0.23	0.69	0.45	0.66	0.88
0	0.63	0.39	0.38	0.99	0.44	0.77	1.11	0.67	1.37	1.14
45	0.78	0.87	0.94	0.95	1.29	1.24	1.49	1.43	1.31	1.71
68	0.86	0.76	0.77	1.36	1.36	1.43	1.68	0.93	1.79	1.07

Table 3.11: Matching errors of bone marrow centroids (with pron-resist torque) for the Heidelberg measurement

pro-/supination angle φ in ° (identified)	Error between computed and measured marrow centroid (in mm) (with resisted pronation torque)									
	cross-section 1		cross-section 2		cross-section 3		cross-section 4		cross-section 5	
	radius	ulna	radius	ulna	radius	ulna	radius	ulna	radius	ulna
-82	0.70	0.85	0.76	0.96	0.82	0.42	0.88	0.18	0.92	0.99
-45	0.81	0.89	1.09	0.81	0.81	0.96	0.92	0.84	0.96	1.03
0	0.97	0.68	1.19	1.12	0.62	1.02	1.14	1.23	1.16	1.30
45	0.86	1.14	0.82	0.92	0.87	1.21	1.06	1.39	1.29	0.97
68	1.05	1.27	0.95	1.46	1.29	1.32	1.68	0.83	1.96	1.62

Table 3.12: Matching errors of bone marrow centroids (with supin-resist torque) for the Heidelberg measurement

pro-/supination angle φ in ° (identified)	Error between computed and measured marrow centroid (in mm) (with resisted supination torque)									
	cross-section 1		cross-section 2		cross-section 3		cross-section 4		cross-section 5	
	radius	ulna	radius	ulna	radius	ulna	radius	ulna	radius	ulna
-82	0.74	0.76	0.67	0.87	0.81	0.95	0.89	0.77	0.95	0.93
-45	0.87	0.93	0.97	1.01	0.94	0.78	1.04	0.89	1.15	1.05
0	0.76	1.13	1.04	0.78	1.17	1.36	1.25	1.08	1.44	1.24
45	1.11	0.97	1.49	1.13	1.32	1.49	1.17	1.33	1.35	1.13
68	1.22	0.98	1.34	1.53	1.73	1.73	1.98	1.42	1.89	1.57

Matching errors for the Essen measurement are shown in Table 3.13, Table 3.14 and Table 3.15. Most errors from 150 processed centroid points are less than 1.5mm, with the maximum 2.11mm occuring at the maximam pronation (palm down).

Table 3.13: Matching errors of bone marrow centroids (without torque) for the Essen measurement

pro-/supination angle φ in ° (identified)	Error between computed and measured marrow centroid (in mm) (without resistive torque)									
	cross-section 1		cross-section 2		cross-section 3		cross-section 4		cross-section 5	
	radius	ulna	radius	ulna	radius	ulna	radius	ulna	radius	ulna
-82	0.55	0.80	0.39	0.92	0.54	0.45	0.34	0.65	0.73	0.95
-45	0.87	0.98	0.56	0.79	0.89	0.83	0.96	0.88	1.12	0.99
0	0.68	0.64	1.02	0.89	0.73	0.66	0.84	0.65	1.18	0.86
45	0.66	0.60	1.18	0.51	0.92	0.94	0.81	0.44	1.43	1.04
68	0.72	1.01	1.19	0.84	0.99	0.97	1.37	1.77	1.38	1.28

Table 3.14: Matching errors of bone marrow centroids (with pro-resist torque) for the Essen measurement

pro-/supination angle φ in ° (identified)	Error between computed and measured marrow centroid (in mm) (with resisted pronation torque)									
	cross-section 1		cross-section 2		cross-section 3		cross-section 4		cross-section 5	
	radius	ulna	radius	ulna	radius	ulna	radius	ulna	radius	ulna
-82	0.85	0.69	0.69	0.83	0.75	0.43	0.94	0.65	0.73	0.87
-45	0.77	0.87	0.96	1.03	0.82	0.96	0.85	0.88	1.32	0.96
0	0.95	0.85	0.97	0.85	0.94	0.89	0.91	0.65	1.48	0.97
45	1.06	0.79	0.87	0.91	0.72	1.34	1.06	0.44	1.23	1.34
68	1.45	1.03	1.21	0.89	1.32	1.46	1.87	2.05	1.56	1.76

Table 3.15: Matching errors of bone marrow centroids (with supin-resist torque) for the Essen measurement

pro-/supination angle φ in ° (identified)	Error between computed and measured marrow centroid (in mm) (with resisted supination torque)									
	cross-section 1		cross-section 2		cross-section 3		cross-section 4		cross-section 5	
	radius	ulna	radius	ulna	radius	ulna	radius	ulna	radius	ulna
-82	0.89	0.78	0.46	0.78	0.87	0.55	0.67	0.89	0.83	0.75
-45	0.97	0.87	0.78	0.86	0.78	0.69	1.04	0.94	1.54	0.99
0	0.59	0.69	0.83	0.75	0.69	0.97	1.43	0.74	1.53	0.86
45	0.84	0.78	0.56	0.91	0.92	0.85	0.97	0.99	1.37	1.04
68	1.02	0.95	0.96	1.04	0.96	1.53	1.62	2.11	1.88	1.63

Two possible reasons for the deviations are: (1) imperfect extraction of the original data from MRT slices, e.g. a little drift of the end point of the computed vector from the measured centroid point in the reconstruction step; (2) shift of the subject's forearm during the MRI scanning, which can blur the images. However, the deviations are so small that these computed values coincide well with measured ones, indicating the feasibility of the described fitting procedure for clinical purposes.

From above-described results, it can be seen that each tester has an individual coefficient ratio c_ϑ / c_s. In order to test the plausibility of the computed values, artificial variations of the coefficient ratio were carried out in the computations for the Heidelberg measurement and the results were compared with the measured bone marrow centers. From Table 3.16, Table 3.17 and Table 3.18, it can be observed that some errors computed with a coefficient ratio decreased by 20% (coefficient 180) are higher than previous results (coefficient ratio 218 in Table 3.10, Table 3.11 and Table 3.12), thus showing that the computed coefficient ratio is plausible for the measured case.

Table 3.16: Matching errors of bone marrow centroids (without torque) for the Heidelberg measurement, with decreasing c_ϑ / c_s by 20%

pro-/supination angle φ in ° (identified)	Error between computed and measured marrow centroid (in mm) (without resistive torque)									
	cross-section 1		cross-section 2		cross-section 3		cross-section 4		cross-section 5	
	radius	ulna	radius	ulna	radius	ulna	radius	ulna	radius	ulna
-82	0.15	0.22	0.48	0.30	0.83	0.82	0.83	0.85	0.91	0.69
-45	0.97	0.61	0.42	0.57	0.98	0.23	0.85	0.45	0.66	0.78
0	0.66	0.21	0.32	1.23	0.18	0.98	1.07	1.34	1.26	1.93
45	1.10	0.64	1.24	1.50	0.98	1.54	1.79	2.51	1.33	2.28
68	0.96	0.76	0.93	1.36	2.19	1.43	1.82	1.43	1.69	1.77

Table 3.17: Matching errors of bone marrow centroids (with pron-resist torque) for the Heidelberg measurement, with decreasing c_ϑ / c_s by 20%

pro-/supination angle φ in ° (identified)	Error between computed and measured marrow centroid (in mm) (with resisted supination torque)									
	cross-section 1		cross-section 2		cross-section 3		cross-section 4		cross-section 5	
	radius	ulna	radius	ulna	radius	ulna	radius	ulna	radius	ulna
-82	0.74	0.76	0.67	0.87	0.81	0.96	0.89	0.80	0.95	0.94
-45	0.77	0.89	1.27	0.75	1.34	0.92	1.75	1.13	1.65	1.15
0	0.76	1.07	0.96	0.86	1.42	1.08	2.15	1.16	1.59	1.52
45	1.12	1.09	1.50	1.25	1.63	1.24	1.78	1.27	2.35	1.58
68	1.18	1.18	1.56	1.61	1.23	2.30	1.97	1.02	2.47	1.72

Table 3.18: Matching errors of bone marrow centroids (with supin-resist torque) for the Heidelberg measurement, with decreasing c_ϑ / c_s by 20%

pro-/supination angle φ in ° (identified)	Error between computed and measured marrow centroid (in mm) (with resisted pronation torque)									
	cross-section 1		cross-section 2		cross-section 3		cross-section 4		cross-section 5	
	radius	ulna	radius	ulna	radius	ulna	radius	ulna	radius	ulna
-82	0.70	0.85	0.77	0.95	0.83	0.78	0.99	0.95	0.89	0.99
-45	0.55	0.65	1.03	0.87	0.84	1.16	1.04	1.29	1.21	1.05
0	0.86	0.88	1.22	0.93	0.96	1.36	1.20	1.54	1.49	1.26
45	1.21	1.09	1.05	1.44	1.11	1.96	1.45	1.79	1.44	1.82
68	1.35	1.47	1.33	2.04	1.31	2.15	1.86	1.95	2.06	2.35

To summarize, the described computation provides reasonable parameters: (a) for the two different subjects, different coefficient ratios due to their different physical parameters, e.g. bone lengths, were obtained; (b) the computed bone physical parameters are very close to the measured values; (c) the matching errors between computed and measured bone marrow centroids based on the optimized coefficient have accepted deviations; (d) the matching errors based on a manipulated stiffness coefficient value (e.g. decreasing by 20%) are slightly higher.

3.5 Modeling visualisation

The object-oriented multibody programming library MOBILE [48] based on C++ is utilized to implement the model and simulate the forearm motion. Its graphical user interface is used to animate the forearm motion, based on which a bone geometry is attached to the moving frames of the mechanism for realistic visualisation. Thus, the simulation of pro-/supination can be visualized online while searching for parameters, e.g. pronation angle (Fig. 3.35), for an optimal result.

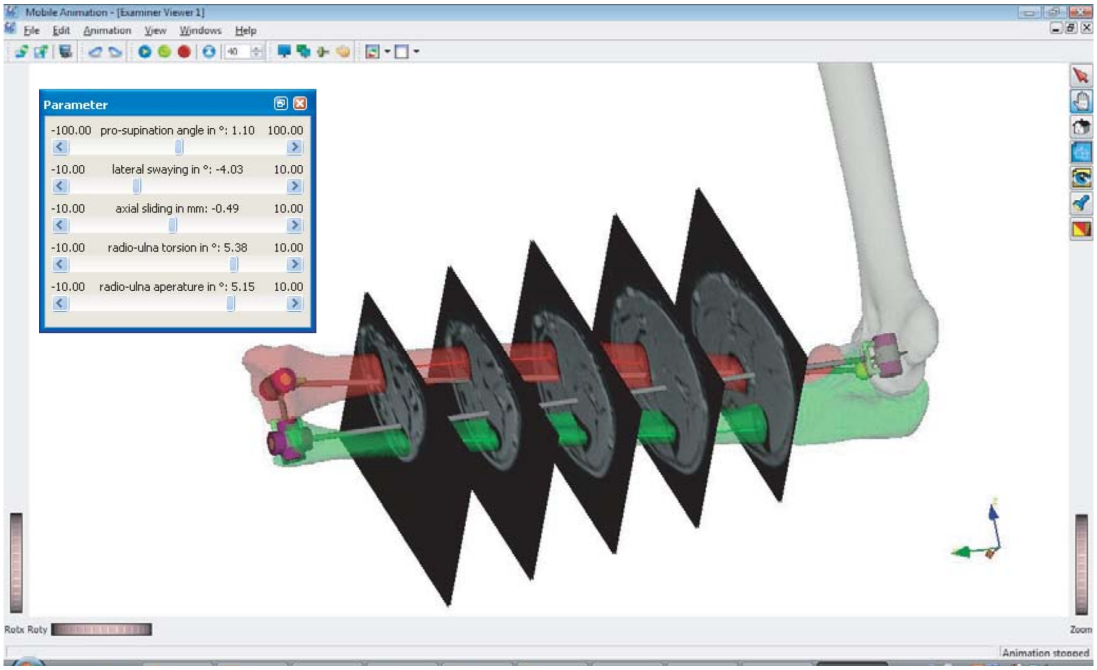

Parameter

-100.00 pro-supination angle in °: 1.10 100.00

-10.00 lateral swaying in °: -4.03 10.00

-10.00 axial sliding in mm: -0.49 10.00

-10.00 radio-ulna torsion in °: 5.38 10.00

-10.00 radio-ulna aperature in °: 5.15 10.00

Fig. 3.35: Screenshot of the developed environment for pro-/supination simulation.

Fig. 3.36 and Fig. 3.37 present the 3D lateral swaying and dislocation between bone ulna and humerus, which shows an obvious changing process of ϑ and $\overline{s}$ during the rotational motion from supination to pronation.

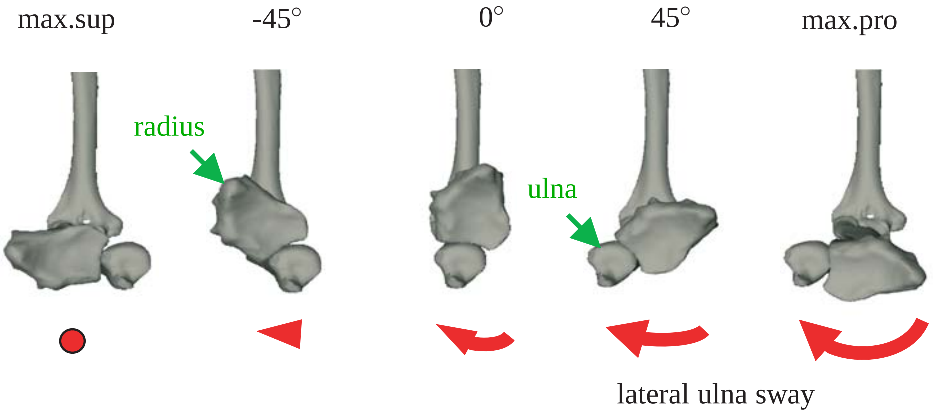

Fig. 3.36: Visible lateral swaying between ulna and humerus.

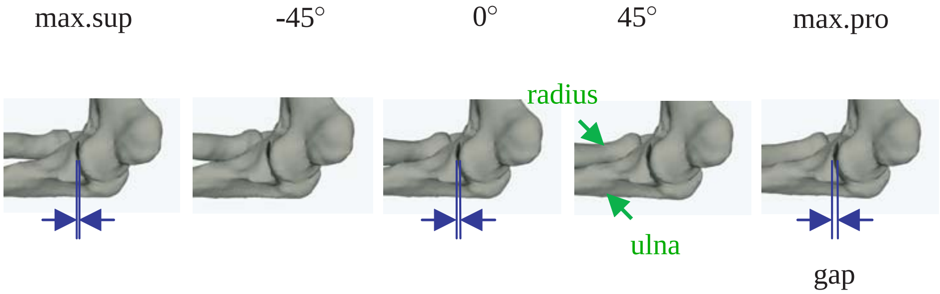

Fig. 3.37: Visible dislocation between ulna and humerus.

The continuous interpolation of intermediate positions of radius with respect to ulna can render a visually smooth motion of radius with respect to ulna, which is required for the medical diagnosis. Moreover, its utilization will in this work be extended to angulated bone geometry in one example analysis, with the aim that the surgery to correct a fracture could be planned and thus unnecessary operation could be prevented. Another add-on of this visualisation program for clinical application is that it can be used relatively easily to assess the distance between bone ulna and radius at random rotational position.

3.6 Comparison of two forearm mechanism models

In order to compare the applicability of this 2DOF model (Section **2.2.3**) to the fixed-axis model described in the literature (Section **2.2.1**), the absolute motions of bone ulna, bone radius motion with respect to the humerus and the relative motions between bone radius and ulna in these two models were studied.

3.6.1 Comparison of absolute motion

In Section **3.4**, the simulation process based on the 2DOF model was presented. In this study, the similar optimization routine (Eq. (3.5)) was applied to the fixed-axis model. The optimization procedure was carried out with the built-in Matlab function `fmincon`, and the development of cost function over iteration steps was plotted in Fig. 3.28(a).

In the minimization, there are four sets of design variables:

1. the mechanism proper parameters r_1,r_2,r_3,r_4 (Fig. 2.5).
2. the rigid-body motion of the elbow, represented by three translations x_0^j, y_0^j, z_0^j and three rotations $\chi_1^j, \chi_2^j, \chi_3^j$ (i.e. $3T - 3R$) for each measurement.
3. the relative location of bone geometry frame $\mathcal{K}_B$ with respect to reference frame of the link, compromising three constant translations, $\kappa_1, \kappa_2, \kappa_3$ and three constant rotations $\epsilon_1, \epsilon_2, \epsilon_3$ for each bone (e.g. ${}_2\underline{r}_B$, ${}^2\mathbf{R}_B$).
4. the offset of the pro-/supination angle $(\varphi^*)^j$, which turns the mechanism to the optimal configuration.

All these design variables must be determined simultaneously, as they are highly coupled. There total $16 + 7\,N$ design variables for N measurements. The initial values were chosen close to the anatomical data, which is shown together with the corresponding simulated results for the Essen measurement in Table 3.19.

During optimization, the best fitting of the computed positions of bone marrow centroids in spatial coordinates to the measured data is searched. Matching errors under three loading conditions are shown in Table 3.20, Table 3.21 and Table 3.22, respectively. Matching errors from the fixed-axis model are obviously much larger compared to those obtained in the 2DOF

Table 3.19: Identified mechanism dimensions

		radius (mm)	ulna (mm)	elbow (mm)	wrist (mm)
Measured		246	246	23	23
Computed	without torque	245.72	245.83	23.24	23.44
	pron. torque	246.26	246.15	22.63	22.37
	supin. torque	246.61	246.26	22.19	21.95
	average	246.23	246.14	22.69	22.58
	S.D.	0.46	0.27	0.53	0.77

model, with a maximum of 4.94mm. And this phenomenon is especially pronounced at the distal portion of the forearm and at the pronation position by this tester.

Table 3.20: Matching errors of bone marrow centroids (without torque)

pro-/supination angle φ in ° (identified)	Error between computed and measured marrow centroid (in mm) (without resistive torque)									
	cross-section 1		cross-section 2		cross-section 3		cross-section 4		cross-section 5	
	radius	ulna	radius	ulna	radius	ulna	radius	ulna	radius	ulna
-82	0.79	0.86	0.88	0.99	1.18	0.83	1.15	0.75	1.19	1.06
-45	1.11	1.01	1.79	1.07	1.77	0.91	1.74	0.77	1.77	1.16
0	1.39	0.88	1.62	1.09	1.47	0.82	1.42	1.51	2.42	1.42
45	0.96	1.51	1.25	1.07	1.75	1.53	1.24	1.83	1.82	1.67
68	1.06	1.02	2.09	1.12	3.54	2.45	3.87	2.54	4.32	1.95

Table 3.21: Matching errors of bone marrow centroids (with pron-resist torque)

pro-/supination angle φ in ° (identified)	Error between computed and measured marrow centroid (in mm) (with resistive torque against supination)									
	cross-section 1		cross-section 2		cross-section 3		cross-section 4		cross-section 5	
	radius	ulna	radius	ulna	radius	ulna	radius	ulna	radius	ulna
-82	0.58	0.80	0.19	0.92	0.38	0.45	0.27	0.65	0.35	0.75
-45	1.09	0.41	1.25	0.79	1.59	0.83	1.74	0.78	1.82	0.78
0	2.23	0.64	3.12	0.89	2.66	0.66	2.76	0.69	3.43	0.85
45	3.22	0.98	3.88	1.31	4.43	1.44	3.63	1.64	4.49	1.25
68	3.48	1.79	4.83	2.09	4.63	2.24	4.35	2.69	4.89	2.84

Table 3.22: Matching errors of bone marrow centroids (with supin-resist torque)

pro-/supination angle φ in ° (identified)	Error between computed and measured marrow centroid (in mm) (with resistive torque against pronation)									
	cross-section 1		cross-section 2		cross-section 3		cross-section 4		cross-section 5	
	radius	ulna	radius	ulna	radius	ulna	radius	ulna	radius	ulna
-82	0.67	0.78	0.45	0.98	0.56	0.49	0.35	0.78	0.44	0.71
-45	1.15	0.41	1.25	0.74	1.59	0.83	1.69	0.88	1.82	0.99
0	1.99	0.69	2.96	0.96	2.48	0.78	2.99	1.65	3.43	1.86
45	2.88	1.10	3.57	1.18	4.39	1.84	3.71	2.44	4.49	2.04
68	3.67	1.43	4.68	2.07	4.58	1.86	4.14	2.57	4.94	3.28

The bone matchings at maximal pronation in these two models are also compared as shown in Fig. 3.38. Hereby, the automatically segmented bone contour on each MRI slice is highlighted with red color. Clearly, the computed bone positions in the fixed-axis model deviate much more from the measured one than those in the 2DOF model at each cross-section level, indicating the better applicability of the 2DOF model.

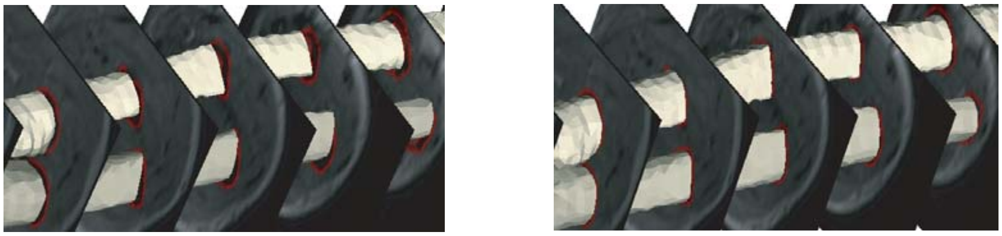

(a) fixed-axis model

(b) 2DOF model

Fig. 3.38: Simulated bones at max. pronation in two models matching to MRI.

Furthermore, the simulated position of the distal radius and ulna at different rotational positions in these two models are compared as shown in Fig. 3.39. In the fixed-axis model, the ulna is fixed and the radius rotates about it. However, in the elasto-kinematic model, the swaying and lateral translation are considered. With cross sections of ulna highlighted with varying colors, the pronounced difference of the absolute motion of bone ulna and radius relative to bone humerus in the two models can be clearly observed.

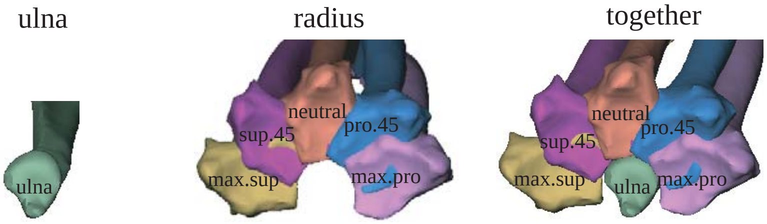

(a) fixed-axis model

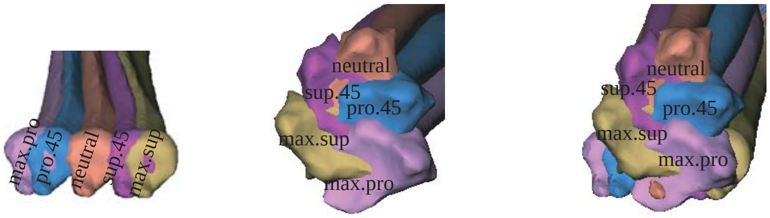

(b) 2DOF model

Fig. 3.39: Simulated absolute motion of bone radius around ulna at the distal portion.

3.6.2 Comparison of relative motion

In order to explain the complex motion of radius and ulna in a more simple way, here the bone movements are referred to the ulna instead of the humerus. Thus, only the transformation of the radius with respect to the ulna needs to be considered. With this simplication, the simple fixed-axis (spherical-spherical) model and the extended 2DOF model (Fig. 2.9(a) and (b)) are compared in the following.

3.6.2.1 Comparison of relative motion of radius to ulna (radius pose)

The spherical concave shape of the proximal articulation of the radius (the fovea capitis radii) allows it to perform a fixed-point, i.e., spherical rotation about the correspondingly shaped surface of the humerus (termed the condyle) as shown in Fig. 3.40(a). This spherical joint representing the fixed-point rotation of radius with respect to humerus, is denoted as S in the fixed-axis model and 2DOF model. The center of this spherical joint is digitized by taking the coronal slice using ImageJ (yellow circle with cross), as shown in Fig. 3.40(b).

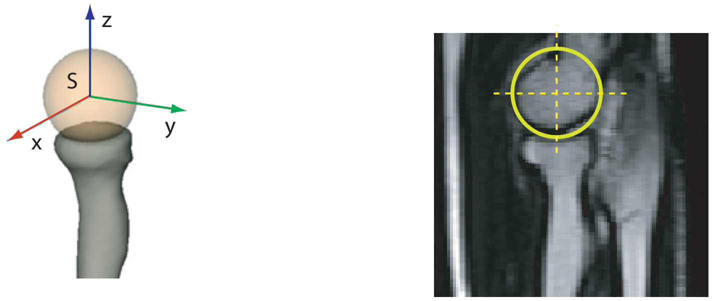

(a) (b)

Fig. 3.40: Spherical concave shape of the proximal articulation of bone radius.

The radius pose with respect to bone ulna during pro-/supination motion is obtained by transforming everything from the inverse of the transformation of inertia frame to ulna frame, after that one can compare the computed radius pose with measured one in two forearm models.

The distance between the computed radius pose and the measured one in the two models is summarized in Table 3.23. Here Δx, Δy and Δz represent the components of distance vectors between computed and measured radius spherical center decomposed in the coordinate of bone ulna. Δd is the distance between them. As can be seen, the distance error in the fixed-axis model increase from supination to pronation where the biggest error is 4.95mm. Limited by the intrinsic shortcoming of the fixed-axis model, its proximal radius head stays at a constant position during the forearm rotational motion. The comparatively large deviation of the result from this modeling indicates that the relative motion between radius and ulna cannot be recognized only as a simple rotation, it also contains a lateral swaying and axial translation. In contrary, the 2DOF model shows a quite well consistency to the measured motion with comparatively very small deviations, with the maximal value of only 0.48mm occuring at pronation position. The other observation from the summarized results is that the main distance deviation comes from y direction, along the forearm shaft to the distal ulna styloid. This phenomenon is reasonable since bone radius has a relative translation towards distal of ulna.

Table 3.23: Matching errors of computed and measured radius spherical head

pro-/supination angle φ in $^\circ$ (identified)	Error between computed and measured radius spherical head Error between computed and measured radius spherical head in (mm)							
	fixed-axis model				2DOF model			
	Δx	Δy	Δz	Δd	Δx	Δy	Δz	Δd
-82	-0.07	-0.69	0.07	0.70	-0.07	-0.39	0.07	0.40
-45	-0.83	-1.40	0.53	1.72	-0.07	-0.41	-0.09	0.43
0	0.15	-2.97	0.36	2.99	0.08	-0.28	0.36	0.47
45	0.22	-4.66	-0.08	4.67	0.05	-0.34	-0.08	0.36
68	-1.08	-4.92	-0.44	4.95	0.05	0.08	-0.47	0.48

To have a closer look on the relative rotational and translational motion, a simulation of the motion of bone radius around bone ulna at the proximal portion is shown in Fig. 3.41. Bone radius is highlighted with different colors at a set of positions from maximum supination (dark yellow), supination 45° (purple), neutral (red), pronation 45° (blue) to maximum pronation (light purple), whereas bone ulna is kept in a fixed position and colored by green. From the color overlap, it can clearly be seen that the radius translates along the distal direction in the 2DOF model, whereas it stays at a constant position in the fixed-axis model. In the local zoomed-in view, it shows the positions of the radius, shown as the spherical balls in the figure, where the yellow balls represent the computed radius spherical centers, and the measured ones are represented by the different color balls with the same colors as their corresponding bone radiuses at the different pro-/supination angles. At each defined pro-/supination angle in the fixed-axis model, the measured spherical center deviates away from the computed one (yellow balls stay at a constant position, away from color balls). However, in 2DOF model the varying computed spherical center match closely to the measured series (color balls follow closely to the yellow balls) .

Based on above discussions, it can be concluded that the 2DOF model shows a good agreement with the measurements both on the relative rotational and translational motion of radius about ulna, whereas the fixed-axis model cannot reflect the reality.

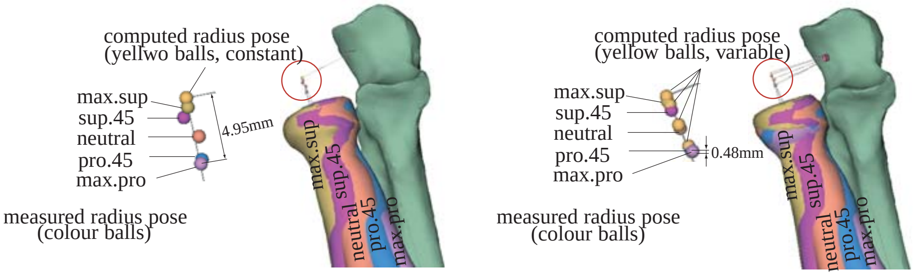

(a) fixed-axis model (b) 2DOF model

Fig. 3.41: Comparison of the radius poses between fixed-axis model and 2DOF model. (yellow balls represent the computed radius spherical head center, other colour balls represent the measured ones corresponding to different pro-/supination angles).

The simulated relative motions of bone radius with respective to bone ulna at the distal portion in these two models are also slightly different, which can be observed from the overlapping pattern of the color regions in Fig. 3.42. For example, as pointed out by the white arrow, the region representing bone radius at maximum supination is not completely covered by the region representing supination 45° in the fixed-axis model, whereas it does in the 2DOF model. As marked by the yellow arrow, the exposed blue part, resulting from the overlap of the regions at 45° pronation and maximum pronation, in the fixed-axis model is larger than that in 2DOF model.

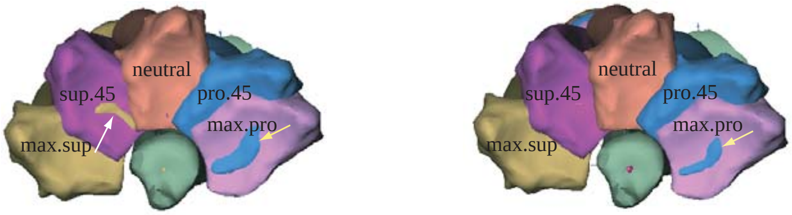

(a) fixed-axis model (b) 2DOF model

Fig. 3.42: Comparison of the distal pose of radius and ulna between fixed-axis model and 2DOF model.

3.6.2.2 Comparison of relative motion of radius to ulna (finite helical axis)

To describe the motion of the radius from supination to pronation, kinematic transformations were calculated for the motion of the radius with respect to the ulna. Hereby, the pose of bone ulna at each rotated condition was transformed to the inertial frame, so that the ulna could be kept at a constant position in the whole rotational process. Afterwards the maximum supination (MS), supination 45° (S45), pronation 45° (P45), and maximum pronation (MP) was transformed to the neutral position (N) by transformations MU, as in Fig. 3.43. Thereafter, the resulting transformation matrices were applied to the corresponding rotated radius, so that each radius dataset was placed in the same coordinate system (tMS and tMP). As following, a second transformation matrix was then created to transmit the radius at each rotated position to the neutral position N by transfornation MR. According to the principles of Kinzel et al. [53], this resultant transformation can be described as a rotation about, and a translation along, a unique axis located somewhere in space. This axis is directly analogous to the instant center of rotation for plane motion and is called the screw axis, or finite helical aixs (FHA), as called in the biomechanics community.

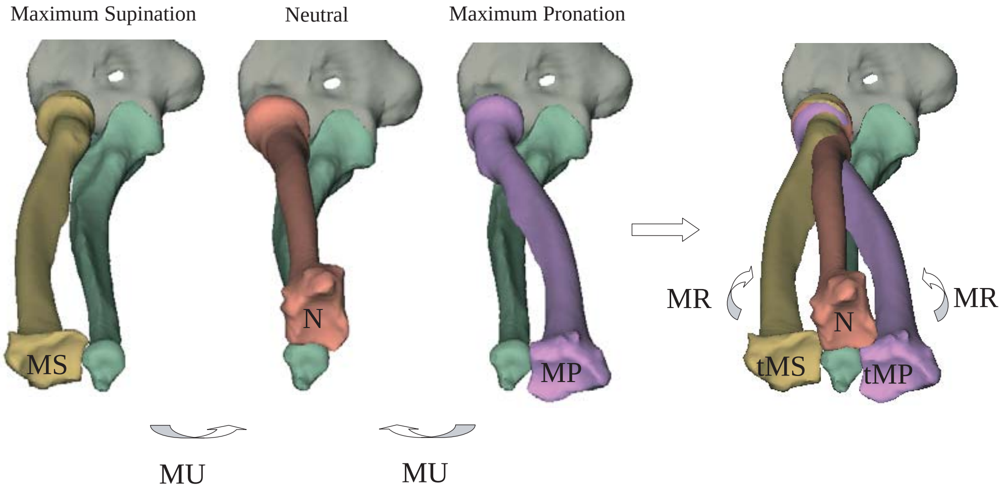

Fig. 3.43: Illustration of the generation of the transformation matrix from max.sup/max.pro to the neutral.

The relative transformation of the radius frame with respect to the ulna frame was then used to calculate the parameters of FHA. The deduced FHA parameters were used to define the location of the forearm axis, and provided a unique and comprehensive description of the kinematics of this enigmatic joint. Table 3.24 lists the computed values of FHA variables: a scalar translation t along the helical axis, and a scalar rotation angle θ around the helical axis.

The rotational amount measured at the grip goniometer was 80° and 65° for maximum supination and pronation respectively. Here, the rotations at supination were defined as negative, and at pronation as positive. The computed FHA parameters for rotation θ in both

Table 3.24: Radius helical parameters at four forearm positions in two models

	fixed-axis model		2DOF elasto-kinemactic model	
	θ (°)	$t(mm)$	θ (°)	$t(mm)$
max.sup 80°	-78.75	0	-77.40	-2.37
sup 45°	-43.09	0	-42.13	-1.66
pro 45°	40.95	0	40.35	1.64
max.pro 65°	63.93	0	62.91	2.25

models are quite close to the measured angle. The proximal and distal translation along the FHAs, t, at max.sup, sup45, pro45 and max.pro were zero in the fixed-axis model. This result is reasonable, since this model assumes a pure rotation of bone radius about ulna. The 2DOF model proved that the proximal-distal translation of the radius relative to the ulna occurs during forearm motion. Here, the translation from distal to proximal along the helical axis was defined as positive. The translations at corresponding positions were -2.37mm, -1.66mm, 1.64mm, and 2.25mm, respectively. The total radius translation in a proximal direction along the FHA from maximum pronation to maximum supination was 4.62 mm, which was consistent with a number of studies which reported translations of the same order of magnitude of 1.5mm in [15], 1.67mm in [54], 0.98mm (95% CI, -0.09 to 2.06) in [55]. Hence, helical axis analysis proves that it can provide not only a geometrical interpretation of the axis of rotation of the forearm, but also to quantify the amount of rotation and translation that occurs around the axis at each forearm position in the 2DOF model.

With the complete set of helical axis parameters, the position and direction of the finite helical axes were plotted onto three dimensional images of forearm bones for visualisation by using the M□BILE program. The FHAs pass through the radial head at the PRUJ, and also pass through the posterior portion of the ulnar head at the DRUJ (Fig. 3.44). The FHAs in fixed-axis model is a constant axis. However, in the 2DOF model, the FHAs pass through the radial head and ulnar head with a slight variance (four colored axis), which can be closer observed in Fig. 3.45. The result based on the 2DOF model coincides well with findings in previous studies. For example, Nakamura et al. performed in-vivo studies using magnetic resonance imaging and reported the movement of the rotational center almost through the radial head to the ulnar head within a small range [20]. Moore et al. found the location of the axis of the DRUJ in the central region of the ulnar head [56]. Another study, using helical axis calculations, also located the DRUJ axis in the central region of the ulnar head [57].

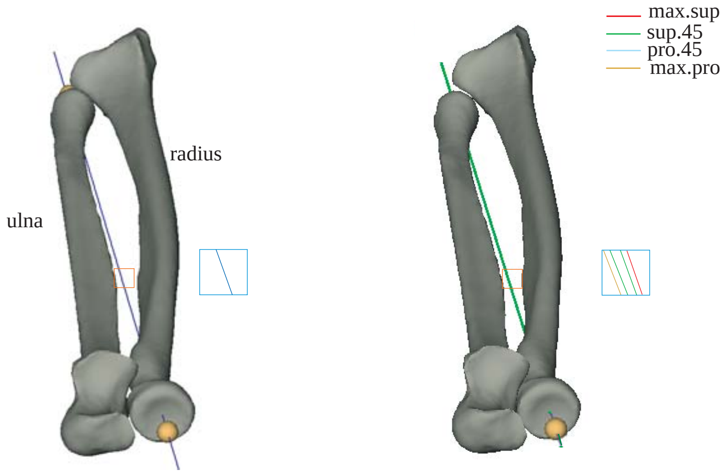

Fig. 3.44: Diagram of the helical axis (left: fixed-axis model, right: 2DOF model).

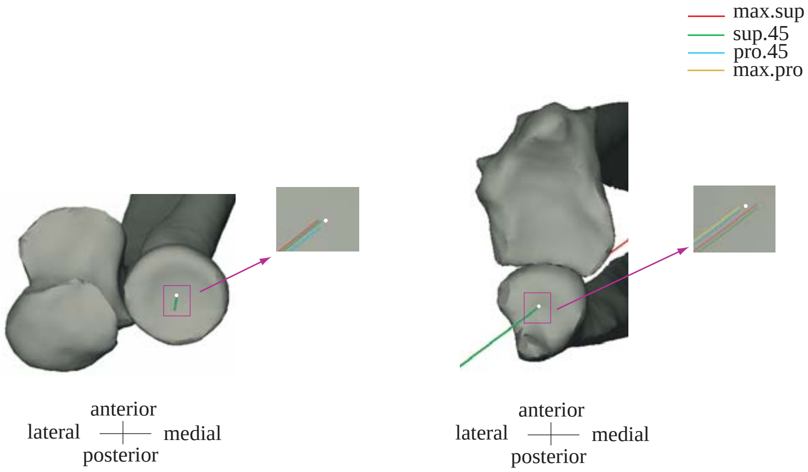

Fig. 3.45: The forearm rotation axis at proximal (left) and distal end (right) (white dot is the centroid of radius/ulna head).

3.6.2.3 Comparison of relative motion of radius to ulna (instantaneous screw axis)

The relative motion of radius was further analyzed by the instantaneous screw axis analysis. Different from above-mentioned finite axis which describes a finite motion, an instantaneous axis describes only an infinitesimal relative motion between two neighboring poses.

As shown in Fig. 3.46, the instantaneous screw axis in the fixed-axis model is a constant axis, whereas in the 2DOF model it varies in a small range at different rotational positions (here 0.5mm in x direction, 0.3mm in z direction). This result obtained from the 2DOF model reflected the reality that bone ulna has a small lateral swaying and light axial dislocation relative to the bone humerus, instead staying at a fixed position.

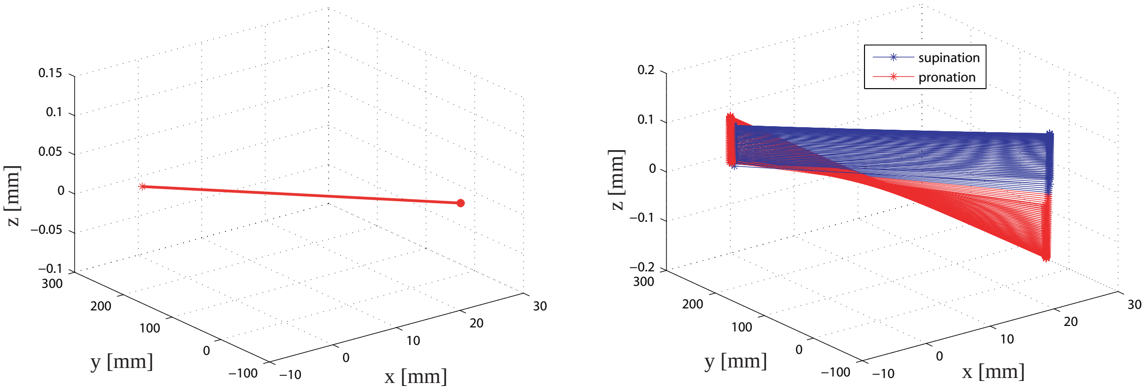

Fig. 3.46: 3D location of the instantaneous screw axis (left: fixed-axis model, right: 2DOF model).

Chapter 4

Distance Study between Forearm Bones

The computation of the minimum distance between two objects is an important topic in many fields such as collision detection [58], virtual prototyping in haptic rendering [59], interference avoidance in NC verification [60], robot path planning [61], and physical simulation in computer graphics [62]. The general principle to calculate a minimum distance between two objects, e.g. A_1 and A_2, is to find the nearest point pair (p, q) such that $p \in A_1$, $q \in A_2$, and the distance between p and q holds minimum. The exact computation is actually a minimization or root-finding method to solve a set of equations which define the conditions for the minimum distance as a common perpendicular line of two free-form objects [62]. It needs to be mentioned that some of the roots in the computation do not fall into the nearest points, and thus are not necessary to be worked out. Moreover, the root-finding method is quite sensitive to the initial guess. As Johnson mentioned [61], the root-finding method has low robustness and low efficiency.

Limaiem presented a method to get a convergence to the local minimal distance between convex curves and surface by insistently updating the nearest points on alternating curves or surfaces [63]. Lin computed the minimum distance between concave surfaces by using bounding polyhedron to obtain the initial values [64]. Both approaches utilized Newton-Raphson method to solve some distance equations to find the roots. To achieve the convergent result, a good initial value is necessary, however, this is hard to be obtained since the surfaces have complex shapes [65].

The minimum-distance computation between curves and surfaces may be categorized into five distance cases: point-curve, point-surface, curve-curve, curve-surface and surface-surface. All these five cases can be solved by a root-finding process of a non-linear equation solver

[61], [66]. For example, in a case of curve-curve with two objects named A_1 and A_2 and two given curves $P = P(u)$ and $Q = Q(v)$ in three-dimensional Cartesian spaces (Fig. 4.1), the squared distance between them is defined as

$$D(u,v) = |P(u) - Q(v)|^2 = (P(u) - Q(v)) \cdot (P(u) - Q(v)) \tag{4.1}$$

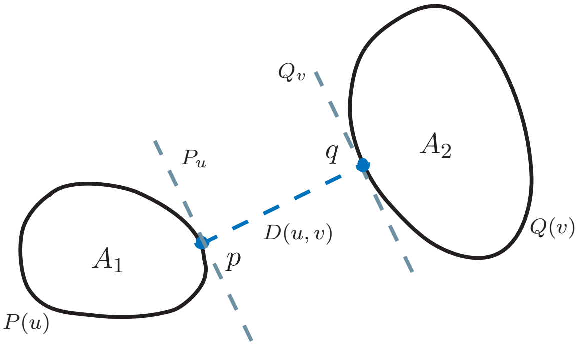

Fig. 4.1: Examples of distance calculations in curve-curve case.

This is a map of (u,v) to non-negative reals. When the nearest points are both inner points of the two curves, the stationary points of $D(u,v)$ satisfy the following equations:

$$D_u(u,v) = 0 \tag{4.2}$$

$$D_v(u,v) = 0 \tag{4.3}$$

where the subscript denotes differentiation with respect to u or v. This equation can be rewritten by using Eq. (4.1) as

$$(P(u) - Q(v)) \cdot P_u(u) = 0 \tag{4.4}$$

$$(P(u) - Q(v)) \cdot Q_v(v) = 0 \tag{4.5}$$

where P_u and Q_v are the tangential vectors of the two curves at points p and q, respectively. When the condition for the shortest distance is satisfied, the projection of D_{uv} (i.e. $|pq|$) on the tangential direction is 0.

In this work, the shortest distance between two forearm bones is regarded as the minimal distance between two rigid objects. Since forearm bones can be recognized to be comprised by a series of bone contours with B-spline curves (Section **4.2.2.3**), the process can thus be categorized as the minimum-distance computation between two curves. In this chapter, the generation of the bone contour with a B-spline curve will be firstly described, followed by the method to calculate the shortest distance between them using the fast algorithm proposed by Ma et al. [67].

4.1 General description of the distance between forearm bones

As shown in Fig. 4.2, the distance d between two forearm bones varies at different cross-section levels (from proximal to distal), as well as at different pro-/supination angles. And from proximal to distal end, this distance increases firstly to a maximum and then decreases.

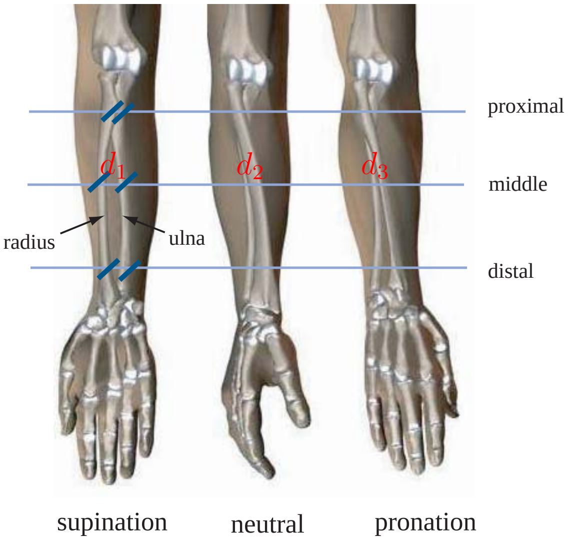

Fig. 4.2: Distance change between two forearm bones (right arm).

As in Fig. 4.3, the rotation is simplified as the relative motion of radius (with different colors at different positions) about ulna (green), therefore the position of bone ulna is not altered. The difference among d_1, d_2 and d_3, which stands for the distance at supination (blue), neutral (red) and pronation (purple) at the same cross-section level respectively, shows the change of distance for varying rotational angles.

To study the distance change between two forearm bones during the rotational motion is a useful tool to evaluate the effect of angular deformities on forearm kinematics, and to predict

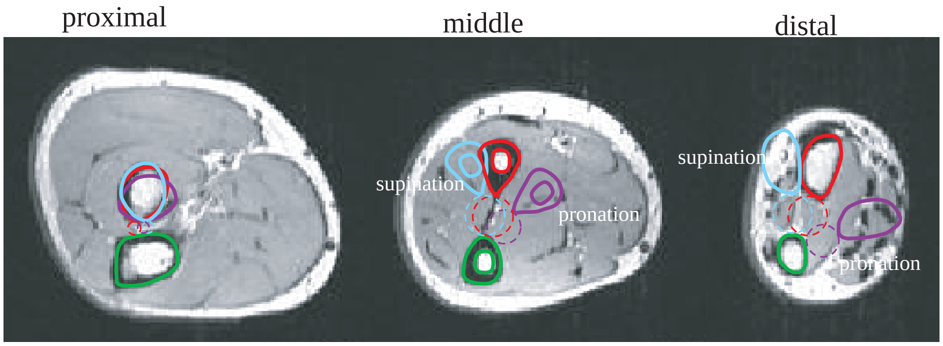

$d1 = 3.06mm$ $d1 = 14.48mm$ $d1 = 12.91mm$

$d2 = 3.17mm$ $d2 = 14.77mm$ $d2 = 13.13mm$

$d3 = 2.89mm$ $d3 = 12.26mm$ $d3 = 11.59mm$

Fig. 4.3: Distance change between two bone contours on the right arm (the dashed circle is the tangital circle to show the shortest distance between bone cross-sections).

the maximum rotational angle by forearm fractures. Therefore, some researches have been done work to address this problem [23], [3].

Weinberg et al. used a kinematic model with vectors to illustrate the bony axis, and a vector compensation system to depict the deformed bones [23]. Based on this kinematic model, Kasten developed a computer program that allows the simulation of forearm rotation and predicts impairment based on existent angular deformities [3]. In the program, the deformed bone was represented by two partial vectors that illustrate the mid-axis of the deformed bone proximally and distally, and the health bone was represented as a vector. The basic idea of predicting the influence of angulations on the range of forearm motion was to calculate the minimal distance between the two bones of the healthy forearm, which was in turn used as the minimum allowable distance of the angulated forearm. However, in his simulation, the real geometries of forearm bones were not considered. Since each of the forearm bones features a complex and irregular geometry, such a simplification could result in errors to some degree.

For clinical applications, it is a requisite to take the geometry of forearm bones into account. Therefore, in this work, the shape of the bone is considered by using the bone outer contour (obtained from MRI slice) as the database. Our study starts from the distance change between two healthy forearm bones, and then the method is extended to the angulated forearm. The former will be discussed in this chapter, and the latter will be detailed in Chapter **5**.

4.2 Generation of bone contour with a curved joint

As discussed above, the distance calculation between two forearm bones is based on the analysis on bone contours from cross-section images (MRI slices) taken at different forearm length levels. The calculation of the distance between each bone contour pair on one slice can be realized by using the algorithm proposed by Ma et al. [67], [68]. Along this way, the shortest distance between the two complete forearm bones can be regarded as the search for the minimum result among a series of MRI slices covering nearly the whole forearm length, i.e., the global minimum from the selected (candidate) pairs.

To calculate the minimum distance between each bone pair on one slice involves seven steps as following:

1. Identify the bone contours from corresponding MRI slices (point clouds) (Section **4.2.1**).
2. Approximate the bone contours with defined cubic B-spline curves $\mathcal{C}(u)$ (contour of ulna) and $\mathcal{C}(v)$ (contour of radius) (Section **4.2.2**).
3. Calculate the shortest distance ds_i between i^{th} bone contour pair $\mathcal{C}(u)_i$ $\mathcal{C}(v)_i$ by an algorithm [67] (Section **4.3**).
4. Create a series of bone body pairs by connecting each two adjacent bone contours $BP(u)^i$ (i^{th} bone body of ulna) and $BP(v)^i$ (i^{th} bone body of radius).
5. Calculate the shortest distance d_i between each bone body pair.
6. Search the global minimum distance d_{min} based on the results from the sequence of bone body pairs d_i of step 5 for one rotational angle.
7. Repeat step 6 for different rotational angles $d_i(\varphi)$ and search for the pro-/supination minimum $d_{min}(\varphi)$.

4.2.1 Bone contour recognization

As described in Section **3.2.1**, an automatic procedure was performed to segment the contours of bone radius and ulna by the image analysis. Some example binary images are shown in Fig. 4.4 to show the change of 2D bone contours from distal to proximal end. In the figure

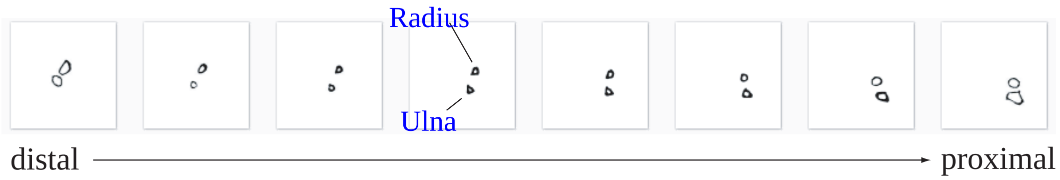

Fig. 4.4: Recognized bone contour from MRI slices.

the upper loop represents the contour of bone radius, and the lower one stands for that of bone ulna.

In the next step, the recognized binary images can be further processed to output point sets for the construction of the outer and inner bone contours for the corresponding 3D structure. Fig. 4.5 shows an example of the plotted bone contour. The left diagram shows the point sets in a XZ plane, which present the cross-section image on a MRI slice. After the Y coordinates of the points are derived from the axial positions of the slice, the 3D contour can be build up as shown in the right diagram. The inner contour points do not need to be considered during the minimum-distance calculation, due to the fact that the minimal distance between two forearm bones can only lie between the outer contour surfaces.

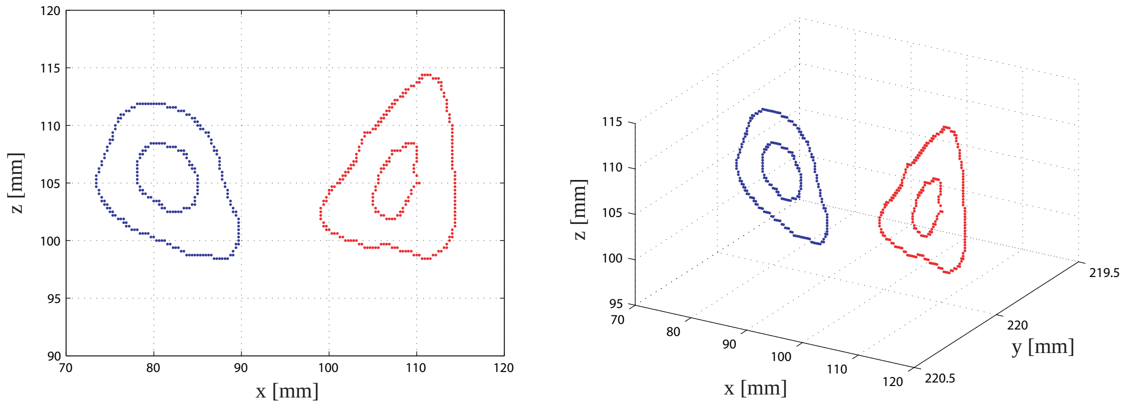

(a) segmented point sets of bone contour in 2D

(b) segmented point sets of bone contour in 3D

Fig. 4.5: Segmented bone contour points (red is for bone ulna, blue is for bone radius).

4.2.2 Bone contour integration

Parameterizing the trajectories of curves is most conveniently achieved by splines, which has become an established method in computer-aided geometric design (CAGD), in curve fitting and in finite element methods (FEM) [69], [70]. Bézier [71] and de Boor [72] firstly developed the conceptions of Bézier curve and B-splines, respectively. Afterwards, some other concepts were introduced, such as the general X-Spline by Blanc and Schlick [73], Pythagorean hodograph curves by Farouki et al. [74], etc. However, Bézier and B-spline are still the standard parameterization for curves and surfaces and are utilized the most.

In this work, the recognized bone contour is parameterized with a cubic B-spline curve by sampling the spline curve with a degree of 3 for equally spaced curve parameters u_k and approximating the obtained sample contour point sets (from MRI slice) using the Dierckx routine `concur` [75].

4.2.2.1 Bézier curve parameterization

The Bézier curve parameterization was developed in the 1960's by Pierre Bézier and Paul de Castlejau, with the first application in automobile design. Today it is widely used, e.g. in OpenGL [76]. A Bézier curve is a parametric curve, which is described by polynomials based on control points. Any number of control points can be used, but 3 or 4 are most common. A Bézier curve passes through its first and last control points, but, in general, not through others.

Given the set of control points, $P_0, P_1, P_2, ..., P_n$, a Bézier curve of degree n is defined by

$$P(u) = \sum_{i=0}^{n} P_i \, B_{i,n}(u) \tag{4.6}$$

where

$$B_{i,n}(u) = \begin{pmatrix} n \\ i \end{pmatrix} (1-u)^{n-i} \, u^i, \; i = 0, 1, \cdots, n \tag{4.7}$$

are the Bernstein polynomials of degree n, and u ranges between $0 \leq u \leq 1$.

A Bézier curve is characterized by:

1. P_0 and P_n are on the curve.
2. The curve is tangent to the control polygon at the endpoint.
3. The sum of base functions at a fixed u is 1 ("Partition of unity").

4. The curve lies completely within the convex hull of its control points ("Convex hull property").
5. No straight line/plane intersects a Bézier curve more times than it intersects the control polyline of the curve ("Variation diminishing property").

The Bézier curve defined over an arbitary parameter interval by $P_{a,b}(u)$ (4.8) is a modification of (4.6):

$$P_{a,b}(u) = \frac{\sum_{i=0}^{n} \left(\begin{array}{c} n \\ i \end{array}\right) (b-u)^{n-i}\,(u-a)^{i}\,P_i}{b-a} = \sum_{i=0}^{n} \left(\begin{array}{c} n \\ i \end{array}\right) \left(\frac{b-u}{b-a}\right)^{n-i} \left(\frac{u-a}{b-a}\right)^{i} P_i \quad (4.8)$$

4.2.2.2 B-spline parameterization

A piecewise collection of Bézier curves, connected end to end, can be called a spline curve. The B-spline is a more general type of polynomial curves, which overcomes the main problem of lacking of local control by the Bézier curve .

A B-spline is defined as

$$\Delta\underline{r}(u) = \sum_{j=1}^{n} \underline{c}_j \, N_{j,k+1}(u) \quad (4.9)$$

as a function of a curve parameter u with spline coefficients $\underline{c}_j \in \mathbb{R}^3$ and n basis splines $N_{j,k+1}$ of degree k. The coefficients of this spline curve are determined based on position control points $\Delta\underline{r}_i$ and fitted to these points by the Dierckx routine `concur` [75]. The basis splines $N_{j,k+1}(u)$ are defined over a set of knots or support points

$$\underline{\lambda} = \left[\lambda_1, \ldots, \lambda_{n+k+1}\right] , \quad (4.10)$$

which, together with the spline coefficients $\underline{c}_j$, are geometrical parameters of the spline curve. The domain of the spline curve is defined by the knots $\lambda_{k+1} = u_B$ and $\lambda_{n+1} = u_E$. To parameterize spatial trajectories, coincident knots are commonly used at the beginning and the end of the spline, because boundary conditions of coincident knots can be more easily prescribed. This leads to the knot vector

$$\underline{\lambda} = [\underbrace{\lambda_1, \lambda_2, \ldots, \lambda_{k+1}}_{\equiv u_B (k+1\ knots)}, \underbrace{\lambda_{k+2}, \lambda_{k+3}, \ldots \lambda_n}_{n-k-1\ internal\ knots}, \underbrace{\lambda_{n+1}, \ldots \lambda_{n+k+1}}_{\equiv u_E (k+1\ knots)}] \quad (4.11)$$

where u_B and u_E are the curve parameters at the beginning and the end of the spline curve, respectively.

The B-spline base functions are usually computed with given knots by employing the recursive scheme described by de Boor [72]

$$N_{j,\ell}(u) = \omega_{j,\ell}\, N_{j,\ell-1}(u) + (1-\omega_{j+1,\ell}) N_{j+1,\ell-1}(u) \tag{4.12}$$

where

$$N_{j,1}(u) \quad = \quad \begin{cases} 1 & \text{if } u \in [\lambda_j, \lambda_{j+1}] \\ 0 & \text{if } u \notin [\lambda_j, \lambda_{j+1}] \end{cases} \quad , \tag{4.13}$$

$$\omega_{j,\ell}(u) \quad = \quad \begin{cases} \frac{u-\lambda_j}{\lambda_{j+\ell-1}-\lambda_j} & \text{if } \lambda_j < \lambda_{j+\ell-1} \\ 0 & \text{otherwise} \end{cases} \quad . \tag{4.14}$$

This recursion follows the local support property of B-splines basis functions, which means that a modification of a control point $\underline{c}_j$ influences the curve only in the domain $[\lambda_j, \lambda_{j+k+1}]$

$$N_{j,k+1}(u) = \begin{cases} >\ 0 & \text{if } u \in [\lambda_j, \lambda_{j+k+1}] \\ \ 0 & \text{otherwise.} \end{cases} \tag{4.15}$$

The derivatives of the recursion can be computed as

$$\frac{d\, N_{j,\ell}}{du}(u) = (\ell - 1)\left(\omega_{j,\ell}^{[1]}\, N_{j,\ell-1}(u) - \omega_{j+1,\ell}^{[1]}\, N_{j+1,\ell-1}(u)\right), \tag{4.16}$$

where $\omega_{j,\ell}^{[1]}$ and $\omega_{j+1,\ell}^{[1]}$ are assumed to be constant. This equation shows that a B-spline of degree k can be at least $(k-1)$ times continously differentiated.

B-spline properties:

B-spline curves share many important properites with Bézier curves, since it is developed from the former. In addition, B-spline curves have more desired properties than Bézier curves. Some most important properties of B-spline curves are listed as following:

1. A B-spline curve $\mathcal{C}_u$ is a piecewise curve with each component curve of degree k.
2. A clamped B-spline curve $\mathcal{C}_u$ passes through the two control points P_0 and P_n at the

ends.

3. A B-spline curve is located in the convex hull of its control polyline ("Strong convex hull property").
4. Given a set of position control points $\Delta\underline{r}_i$, changing the position of a control point $\underline{c}_i$ only affects the curve $\mathcal{C}_u$ within the interval $[\lambda_i, \lambda_{i+k+1}]$ ("Local modification scheme").
5. $\mathcal{C}_u$ is $\mathcal{C}^{n-k}$ continuous at a knot of multiplicity k.
6. If the curve is in a plane, no straight line intersects a B-spline curve more times than it intersects the curve's control polyline ("Variation diminishing property").
7. Bézier Curves are special cases of B-spline curves. When $n = k$ (i.e., the degree k of a B-spline curve is equal to n, the number of control points minus 1), and there are $2(k+1) = 2(n+1)$ knots with $k+1$ of them clamped at each end, this B-spline curve is reduced to a Bézier curve.

The property 4, 5 and 7 will be further utilized in Section **4.3**.

4.2.2.3 Spline as a CurveJoint

The application of CurveJoint is as described in [77]. The bone contour curve is integrated in the basis library for multibody analyis MOBILE . Input frame $\mathcal{K}_1$ and the path coordinate u to the motion of a coordinate frame fixed on the moving body (Darboux/Frenet/Parallel transport frame) on the curve as output frame $\mathcal{K}_2$. In this context, the curved joint contour $\mathcal{C}$ is parameterized using B-splines as a function of a curve parameter u with spline coefficients $\underline{c}_j$ and n basis splines $N_{j,k+1}$ of degree k:

$$\Delta\underline{r}(u) = \sum_{j=1}^{n} \underline{c}_j \, N_{j,k+1}(u). \tag{4.17}$$

The spline coefficient vectors $\underline{c}_j \in \mathbb{R}^3$ are determined based on position control points $\Delta\underline{r}_i$ and fitted to these points by the Dierckx routine concur [75] with smoothing optimization over the complete length of the spline, and prescribed boundary conditions for positions, tangents and curvature. The curve is then parametrized by arc length, therefore one can substitute the curve parameter u with the path coordinate s. The rotation matrix $\Delta\mathbf{R}$ transforming coordinated from $\mathcal{K}_2$ to $\mathcal{K}_1$ is then $\Delta\mathbf{R} = [{}^1\underline{t}(s)\ {}^1\underline{n}(s)\ {}^1\underline{b}(s)]$, where $\underline{t}(s)$ is the tangent vector, $\underline{n}(s) = \Delta\underline{r}''(s)/\kappa(s)$ is the normal vector, $\kappa(s) = \left\|\Delta\underline{r}''(s)\right\|$ is the curvature and $\underline{b}(s) = \underline{t}(s) \times \underline{n}(s)$ is the binormal vector of curve $\mathcal{C}$. An additional rotation, the so-called banking, is introduced as a tangential revolute joint after $\mathcal{K}_2$ with angle $\beta(s)$ modelled as a one dimensional spline determined by angular control points β_m in the same sense as the position control points $\Delta\underline{r}_i$ determine $\mathcal{C}$. With that, the orientation of the output frame of the curved joint is defined by $\Delta\mathbf{R}' = \Delta\mathbf{R}(s) \circ Rot[x, \beta(s)]$.

In this Dierckx algorithm, the `FORTRAN` code `concur` generates splines of degree one, three, or five. Hereby, two types of optimizations are processed, the weighted least square and constrained smoothing spline optimization. Throughout this study, $k = 3$ is set due to its typification. As shown in Fig. 4.6, the smooth cubic curves presented as blue and red curve for contour of bone radius and ulna are the interpolated B-spline curves, which well approximates the measured point sets (dense green points) of the bone contour. The computed control points for contour of bone radius and bone ulna are different ones, shown here as pink and blue circles for their corresponding B-spline curves, which are then connected to form the control polygons.

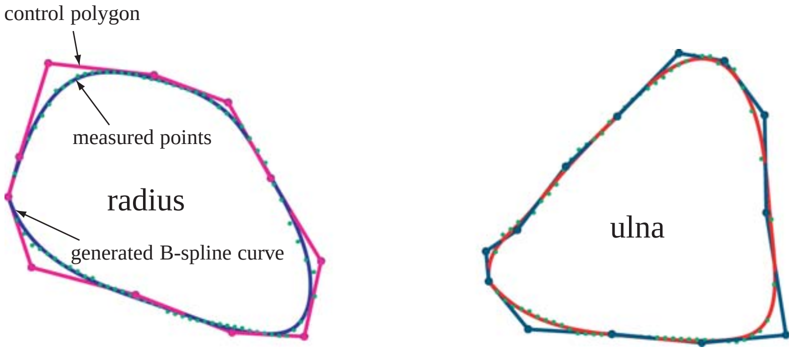

Fig. 4.6: Bone contour integrated with B-spline by Curvejoint and its control polygon.

4.3 Minimum distance between two bone contours

After the generation of bone contours, the next step is to find an effective method to calculate the minimum distance between them (outer contour of bone ulna and radius). Since the bone contour is traced as a cubic B-spline curve, the minimum distance is then calculated between these two B-spline curves.

In one example MRI slice (Fig. 4.7), the outer contours of bone ulna and radius are presented as $\mathcal{C}_u\,(u)$ and $\mathcal{C}_r\,(v)$ in three-dimensional Cartesian spaces. $\mathcal{K}_u$ and $\mathcal{K}_r$ are the moving frame along the B-spline, presenting as $\underline{r}_1\,(u)$ and $\underline{r}_2\,(v)$ relative to the base frame $\mathcal{K}_0$. $\underline{t}_1\,(u)$, $\underline{t}_2\,(v)$ are the tangent vectors at an arbitrary point on the curve. $\Delta\underline{r}(u, v)$ is the distance vector between these two bone contours, which depends on the path parameters u and v, where

$$\Delta\underline{r}(u, v) = |\underline{r}_1\,(u) - \underline{r}_2\,(v)| = |\mathcal{C}\,(u) - \mathcal{C}\,(v)| \tag{4.18}$$

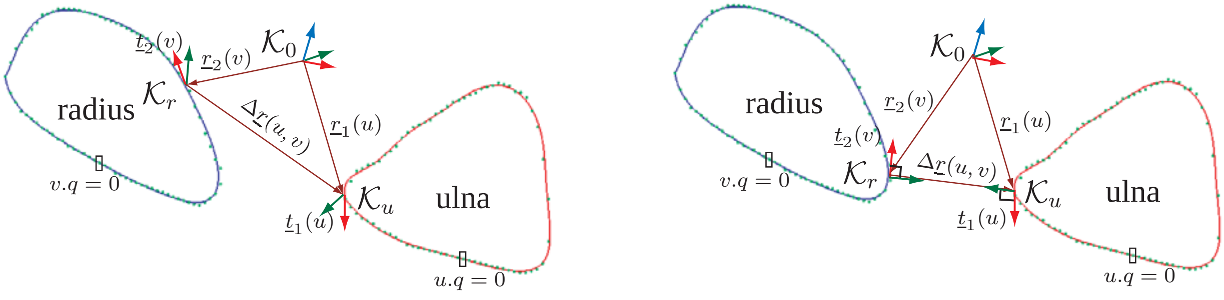

(a) (b)

Fig. 4.7: Distance calculation between two forearm curves. (a) distance between two arbitrary points along spline contours, (b) shortest distance between two spline contours.

The distance point pairs between the two contours for various u and v are a map from $\mathbb{R}^2$ to the set of non-negative real number, as plotted in Fig. 4.8.

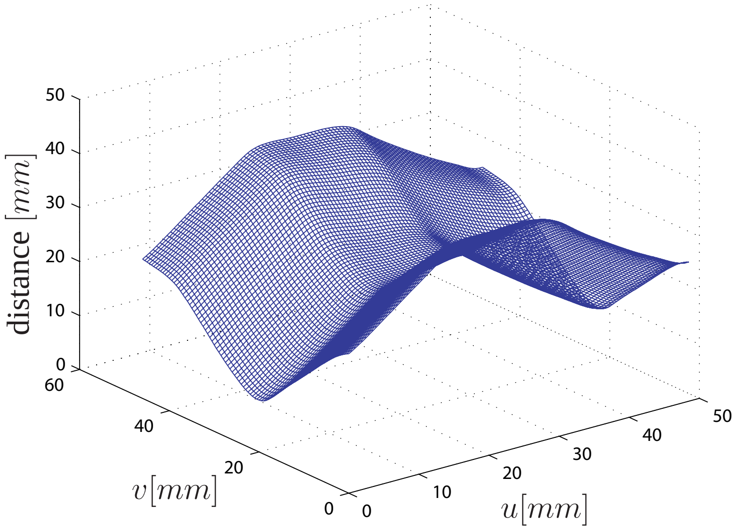

Fig. 4.8: Plot of distance changing between two B-spline curves with variables u and v.

To determine the minimum distance, the following two conditions $f_1(u, v)$ and $f_2(u, v)$ between these two B-spline curves need to be reached:

$$f_1(u,v) = \underline{t}_1(u) \cdot \Delta\underline{r}(u,v) = 0 \tag{4.19}$$

$$f_2(u,v) = \underline{t}_2(u) \cdot \Delta\underline{r}(u,v) = 0 \tag{4.20}$$

In these equations the conditions for the minimum distance are defined as a common perpendicular line of two curves. These systems of equations can be solved by the Newton-Raphson (NR) method, however, it is hard to predict good initial values in this method to achieve convergence to the correct result, due to the complexity of the curve's shape.

In this work, an alternative method is applied to compute the minimum distance between two 2D spline curves. Although the contours of the MRI cross-sectional scans are mostly closed convex curves, for which a special elementary solution is possible, we chose here, the more generalized approach of Ma et al. [67] in order to warrant a fully automated procedure even in the presence of non-convex cross-sectional profiles, as can appear at some locations of ulna and radius. This approach represents a fast, accurate and robust algorithm, which has been already used to find the minimum distance between general 2D and 3D NURBS (non-uniform rational B-spline) curves. Since the B-spline curve is a special form of NURBS, this method is principally applicable to the B-spline curve. This calculation is carried out by decomposing both of the Spline curves into their piecewise-Bézier forms. Then, candidate curve pairs for the minimum distance, as a subset of all possible pairs, are extracted by a two-level selection process. The first-level selection uses upper-lower bounds of Bézier subcurve to pre-filter pairs. The second-level selection is the test on the spatial relationship between a pair of Bézier curves. After candidate pairs are obtained, an iterative multi-dimensional Newton-Raphson method is applied on them to approximately calculate the local minimum distances. Finally, by comparing all these local minimum distances, we are able to find the global minimum distance. To improve the accuracy of the result, the multi-dimensional Newton-Raphson method is applied at last on the last candidate pair to get the final result.

4.3.1 Outline of the algorithm

As already mentioned above, there are two basic steps in the algorithm. In the pre-processing step, two B-spline curves are decomposed into their piecewise-Bézier forms, and the bounding spheres of these Bézier subcurves are determined. The next step comprises two-level selections to find candidate pairs and local minimum-distance calculations on them. A comparison among the local results can render the global minimum distance. The following shows more details.

Algorithm 1: Mini_Distance ($\mathcal{C}_u, \mathcal{C}_v$)

```
Input: $\mathcal{C}_u$ is the first B-spline curve. $\mathcal{C}_v$ is the second B-spline curve.
//first part: pre-processing
begin
  Decompose $\mathcal{C}_u$ into a set of Bézier subcurves A. (Section 4.3.2)
  Decompose $\mathcal{C}_v$ into a set of Bézier subcurves B. (Section 4.3.2)
  Test "valid" control polygon for both A and B. (Section 4.3.3)
  Calculate the bounding spheres for both A and B. (Section 4.3.4)
end
//second part: run-time computation
begin
  Use upper-lower bounds to remove pairs. (Section 4.3.5)
  Use the spatial relationship to continue to remove pairs. (Section 4.3.6)
  Use the multi-dimensional NR method to compute approximate local distances between a candidate pair. (Section 4.3.7)
  Find the global minimum distance by comparing all local minimum distances.
  Use the multi-dimensional NR method to increase the accuracy of global minimum distance.
end
return  the minimum distance
```

4.3.2 Pre-processing

Pre-processing involves decomposing B-spline curves into their piecewise-Bézier forms and then calculating the bounding spheres of these Bézier subcurves.

4.3.2.1 Decomposing the B-spline curve

The decomposition of B-spline curves into their Bézier subcurves is realized by the Boehm's knot insertion method [78]. The insertion of new knots into present knot systems by using the blossoming formula does not have influence on the curve shape. The insertion is a loop until the interior knots all have multiplicity of $k-1$. When the process is finished, the maximum number of obtained Bézier subcurves is $n-k$, where n is the number of control points and k is the degree of the B-spline curve.

Let us assume that the new knot u is located in the knot span $[\lambda_j, \lambda_{j+1}]$. Since a B-spline curve lies in the convex hull of its control polyline, the corresponding curve point P_u is also in the convex hull which is defined by control points $P_j, P_{j-1}, ..., P_{j-k}$, and all other basis functions are equal to zero. Hence, calculation of the knot insertion can be restricted on control points $P_j, P_{j-1}, ..., P_{j-k}$. The way of inserting u is to find k new control points Q_j on leg $P_{j-1}P_j$, Q_{j-1} on leg $P_{j-2}P_{j-1}$, ..., and Q_{j-k+1} on leg $P_{j-k}P_{j-k+1}$, so that the old polyline between P_{j-k} and P_j (Fig. 4.9 black line with square) is replaced by $P_{j-k}Q_{j-k+1}...Q_jP_j$

(Fig. 4.9 red line with circle) by cutting the corners at $P_{j-k+1}, ..., P_{j-1}$. Here, except that $k-1$ control points of the original control polyline are removed and replaced with p new control points, all other control points are unchanged. After inserting a new knot, the knot vector becomes λ_1, …, λ_j, u, λ_{j+1}, ..., and λ_{n+k+1}. If the new knot u is equal to λ_k, the multiplicity of λ_k is increased by one.

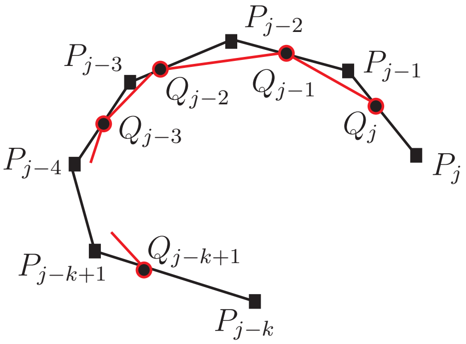

Fig. 4.9: Diagram of the original control points removed and replaced by inserting a new kont.

The formula for computing the new control point Q_j on leg $P_{j-1}P_j$ is the following:

$$Q_i = (1 - a_i)\, P_{j-1} + a_i\, P_i \tag{4.21}$$

where the ratio a_i is defined as below:

$$a_i = \frac{u - \lambda_i}{\lambda_{i+k} - \lambda_i}, \quad j - k + 1 \leq i \leq j \tag{4.22}$$

A B-spline curve is known as a composite Bézier curve if its interior knots all have multiplicity equal to $k-1$. Therefore, converting a B-spline curve into a composite Bézier curve is equivalent to repeatedly inserting the knots into the knot vector until all the interior knots have multiplicity equal to $k-1$.

4.3.3 Tests of "valid" control polygons

To test the validity of a polygon, i.e. whether it is convex, a convenient method is to inspect the dot product results of its two vectors. As shown in Fig. 4.10, a control polygon of a Bézier curve with degree p $(p > 2)$ has control points $P_0, P_1, \ldots, P_{n-1}, P_n$, where P_0 and P_n are at the two ends. The points V_1 and V_2 are projected from the vertex P_i and one of the endpoints, P_n $(i < (n/2))$ or P_0 $(i \geq (n/2))$, to the line segment $P_{i-1}P_{i+1}$, respectively. The sign of the dot product $R = \overline{V_1P_i} \cdot \overline{V_2P_n}$ $(i < (n/2))$ or $R = \overline{V_1P_i} \cdot \overline{V_2P_0}$ $(i \geq n/2))$ can be used to judge whether vertex P_i is in the "convex" direction or not. If the sign is positive, this vertex is in a "concave" direction, otherwise not. All the vertices except of the end points are checked one by one until one positive sign is obtained. If all the results are negative, the control polygon can be concluded as a 2D/3D convex polygon. Based on this, if both the first interior angle $\angle P_1P_0P_n$ and the last interior angle $\angle P_{n-1}P_nP_0$ are less than $90°$, this convex polygon is regarded as a "valid" polygon.

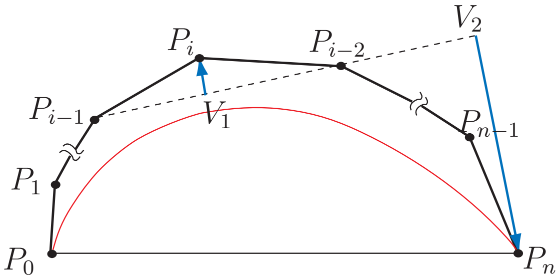

Fig. 4.10: A 2D "valid" polygon.

Algorithm 2: Is_Valid_Polygon

```
begin:
  for $i = 1$ to $i < n$ by $i++$ do
      if $i < (n/2)$ then
      $R = \overline{V_1P_i} \cdot \overline{V_2P_n}$;
      else
         $R = \overline{V_1P_i} \cdot \overline{V_2P_0}$;
      if $R > 0$ then
         return FALSE
      end
  end
  $R_1 = \overline{P_0P_1} \cdot \overline{P_0P_n}$;
  $R_2 = \overline{P_nP_{n-1}} \cdot \overline{P_nP_0}$;
  if $R_1 < 0$ or $R_2 < 0$ then
      return FALSE
  end
  // It is a valid polygon
  return TRUE
end
```

After the types of 2D/3D control polygons are classified, analyses are performed to determine the spatial relationship between two "valid" control polygons or between one "valid" control polygon and one "invalid" control polygon. Their spatial relationship is useful to judge the existence of a common perpendicular line between these two Bézier curves.

4.3.4 Search for bounding spheres of Bézier objects

To calculate the distance between bones during motion, it is better to use bounding spheres than bounding boxes, since global rotating transformations have no influence on the distance between two spheres. As it is known that a Bézier subcurve is located in the convex hull of its control polygon according to the strong convex hull property, the problem can be solved by searching for the bounding spheres of the control polygons of Bézier subcurves. Although this process does not yield the smallest bounding, it is efficient enough to remove a large percentage of candidates in the first-level selection described in Section **4.3.5**.

There are several steps towards finding the bounding sphere of a Bézier subcurve: (1) among all pairs of control points of the Bézier subcurve we find the longest edge; then the center of the longest edge is used as the center of the bounding sphere; (2) the distances from the center of the sphere to all control points is calculated; (3) if a distance is larger than the radius of the sphere, the radius is updated with this distance. When there are n control points, the total number of calculations is $n(n+1)/2$. Fig. 4.11 shows example bounding spheres of decomposed B-spline curves.

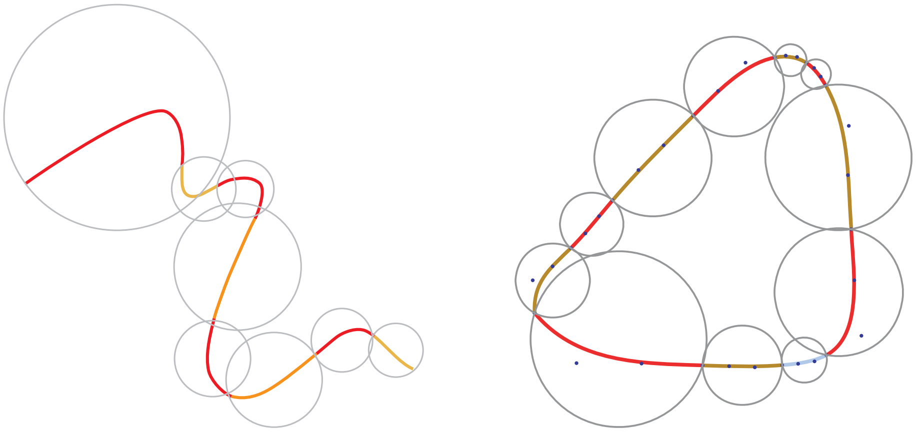

(a) A general decomposed B-spline

(b) closed B-spline of the bone contour

Fig. 4.11: Boundary spheres of a decomposed B-spline curve.

4.3.5 First-level selection

In the first-level selection, all possible pairs between two Bézier subcurves with each from one B-spline curve representing one forearm bone are analyzed. For each pair, the upper and lower bound distances between their bounding spheres are calculated as D_{max} and D_{min}, respectively, as illustrated in Fig. 4.12. The found minimum upper-bound distance among all pairs is used as the reference to remove any pair whose lower-bound distance is larger than this value.

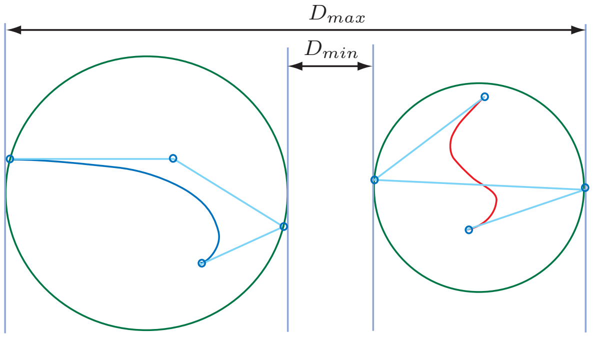

Fig. 4.12: Lower-bound distance D_{min} and upper-bound distance D_{max}.

4.3.6 Second-level selection

In the second-level selection, the spatial relationship is studied on the remaining pairs of Bézier subcurves after the previous step. If the test turns $TRUE$ (i.e. if there is a possible perpendicular between them), then it is a candidate pair, and vice versa.

There are three possible combinations of different types of control polygons:

1. two "valid" control polygons
2. one "valid" and one "invalid" control polygon
3. two "invalid" control polygons

Case 1 and case 2 can be carried out using the procedure described below. However, as the proof of the existence of a possible common perpendicular line between two "invalid" control polygons from a pair of Bézier curves (case 3) is impossible, we select them here as candiate pairs, since the percentage of the such case is quite low.

4.3.6.1 Two "valid" control polygons

A *four-dot condition* can be used to examine the spatial relationship between a point and a "valid" control polygon of a Bézier curve. As shown in Fig. 4.13(a), if a perpendicular line from a point towards the Bézier curve is to exist, the point must lie inside the area AP_0P_nB or the area CP_0P_nD. The location of this point can be determined by solving the four-dot condition: $R_1 = \underline{P_0P} \cdot \underline{P_0P_1}$, $R_2 = \underline{PP_n} \cdot \underline{P_{n-1}P_n}$, $R_3 = \underline{P_nP_0} \cdot \underline{P_nP}$, and $R_4 = \underline{P_nP_0} \cdot \underline{P_0P}$. If If $R_1 < 0$ or $R_2 < 0$ and $R_3 * R_4 > 0$, the point must be outside area AP_0P_nB and CP_0P_nD. Therefore, "$R_1 < 0$ or $R_2 < 0$ and $R_3 * R_4 > 0$" is used as the criteria (Fig. 4.13(b)) to judge whether there is a perpendicular line between the point and the curve.

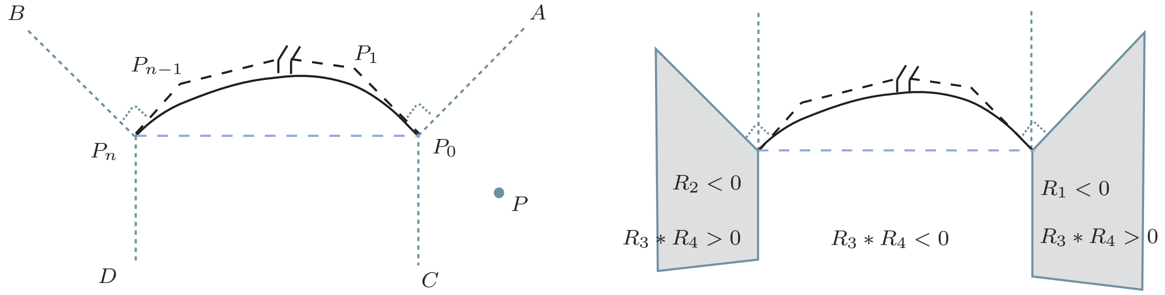

(a) The spatial relationship

(b) Four-dot condition

Fig. 4.13: Spatial relationship and four-dot conditions.

In Fig. 4.14(a), all control points of $\mathcal{C}_2(u)$ are inside the area AP_0C, therefore, the minimum distance is from P_0 to the closest point on $\mathcal{C}_2(u)$. It still needs one more condition to ensure all control points $(Q_0, \cdots, Q_m)$ are either inside the area AP_0C or inside the area BP_nD. It is to check the sign of the dot product R_1 for all control points. If the signs do not change, all control points are in one area, otherwise, they are distributed within two areas, and the conditions of minimum distance would be satisfied (Fig. 4.14(b)). If the "four-dot condition" is satisfied and all control points are on the same side, according to the convex hull property of B-spline curves, any point Q_c on the curve $\mathcal{C}_2(u)$ must also satisfy the "four-dot condition". Thus, the closest point on $\mathcal{C}_1(u)$ for Q_c must be one of the endpoints (P_0 or P_n) and the minimum distance between $\mathcal{C}_1(u)$ and $\mathcal{C}_2(u)$ is from one of them to the closest point on the other curve.

Along this way, the minimum distance between two control polygons can be categorized in two cases. If the sign of dot product R_1 for all control points $Q_0, \cdots, Q_m)$ do not change, the polygon has no points lying either in AP_0P_nB or in CP_0P_nD (Fig. 4.14(a)). As discussed above, there is no perpendicular line from any point at $\mathcal{C}_2(u)$ to $\mathcal{C}_1(u)$, and therefore the minimum distance is from one of the endpoints of $\mathcal{C}_1(u)$ to the closest point on $\mathcal{C}_2(u)$ (P_0 in Fig. 4.14(a)). If the signs change, the polygon contains point(s) in the two areas, and the "four-dot condition" described above can be satisfied (Fig. 4.14(b)). According to the convex hull property of B-spline curves, any point on the curve $\mathcal{C}_2(u)$ can satisfy the "four-dot condition". Thus, the minimum distance between $\mathcal{C}_1(u)$ and $\mathcal{C}_2(u)$ is from one point on one of them to the closest point on the other curve.

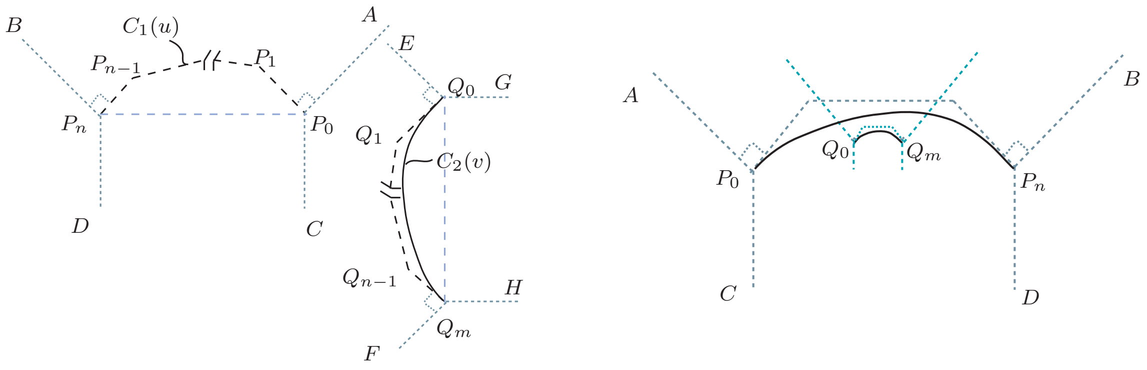

(a) Relationship test

(b) A special case

Fig. 4.14: Relationship test and a special case.

The details is seen in Algorithm 3.

Algorithm 3: Poly(P)_vs._Poly(Q)

```
Input:  $P$ is the first "valid" control polygon. $Q$ is the second "valid" control polygon.
Output: TRUE if there is a possible perpendicular between $P$ and $Q$,
        FALSE  otherwise.
begin
  Flag  = FALSE;
  for each control point on $P$ do
    test the four-dot condition;
    if a condition is not satisfied or sign of $R_1$ changed then
      Flag=TRUE;
      break;
    end
  end
  if Flag=FALSE then
    return FALSE
  end
  Flag=FALSE
  Repeat same procedure for the control polygon $Q$
  return Flag
end
```

4.3.6.2 One "invalid" control polygon and one "valid" control polygon

In this case it needs only to carry out tests on all control points of the "invalid" control polygon according to the "four-dot" condition, as shown in Algorithm 4.

Algorithm 4: InvalidPoly(P)_vs._ValidPoly(Q)

```
Input:   $P$ is an "invalid" control polygon. $Q$ is a "valid" control polygon.
Output:  TRUE  if there is a possible perpendicular between $P$ and $Q$,
         FALSE  otherwise.
begin
  Flag = FALSE;
  for each control point on $P$ do
    test the four-dot condition;
    if a condition is not satisfied or sign of $R_1$ changed then
      Flag=TRUE;
      break;
    end
  end
  retrun Flag
end
```

4.3.7 Multidimensional Newton-Raphson method

A multidimensional Newton-Raphson (NR) method is used to compute the minimum distance between a pair of Bézier subcurves. This method is well-known for solving non-linear equations in multidimensional spaces. With given approximate initial value, the NR method provides a new approximate solution based on the local linearization process about the current point by using the Jacobian matrix, which results in a linear system to be solved as:

$$X_{i+1} - X_i = -[J(X_i)]^{-1} F(X_i) \tag{4.23}$$

This process is repeated and a convergence can be achieved quadratically, if the initial guess is "near" to the solution. The conditions for determining the minimum distance between two curves are considered as two scalar functions described as following:

$$f(u,v) = (\mathcal{C}_1(u) - \mathcal{C}_2(v)) \cdot \mathcal{C}_1'(u) = 0 \tag{4.24}$$

$$g(u,v) = (\mathcal{C}_1(u) - \mathcal{C}_2(v)) \cdot \mathcal{C}_2'(v) = 0 \tag{4.25}$$

substituting $X_i = [u_i, v_i]^T$, $F(X_i) = [f, g]^T$, $J(X_i) = \begin{bmatrix} f_u & f_v \\ g_u & g_v \end{bmatrix}$ into Eq. (4.23) yields

$$\begin{bmatrix} u_{i+1} \\ v_{i+1} \end{bmatrix} - \begin{bmatrix} u_i \\ v_i \end{bmatrix} = \begin{bmatrix} A & B \\ C & D \end{bmatrix}^{-1} \begin{bmatrix} \mathcal{C}_1(u_i) \\ \mathcal{C}_2(v_i) \end{bmatrix}, \tag{4.26}$$

where $A = \mathcal{C}_1''(u_i) \cdot (\mathcal{C}_2(v_i) - \mathcal{C}_1(u_i)) - [\mathcal{C}_1'(u_i)]^2$, $B = \mathcal{C}_1'(u_i) \cdot \mathcal{C}_2'(v_i)$, $C = -\mathcal{C}_2'(v_i) \cdot \mathcal{C}_1'(u_i)$, $D = [\mathcal{C}_2'(v_i)]^2 + \mathcal{C}_2''(v_i) \cdot (\mathcal{C}_2(v_i) - \mathcal{C}_1(u_i))$.

With candidate pairs obtained after the second-level selection, the multidimensional NR method is conducted to compute the minimum distance for each pair. Hereby, $u = (u_0 + u_n)/2$ is set as the initial value for $\mathcal{C}_1(u)$, and $v = (v_0 + v_m)/2$ is set as the initial value for $\mathcal{C}_2(v)$, where n and m are the highest indices for the knots of $\mathcal{C}_1(u)$ and $\mathcal{C}_2(t)$, respectively. Because both curves are simple shapes and initially guessed values are actually quite close to optimal results, the iteration cycles of the multidimensional NR method is less than 2 or 3 until an accuracy of 0.01 is reached. Therefore, 5 iterations are set in the calculation to find the local approximately minimum distance. If the NR method fails to converge within the iteration limit, the minimum distance must be from the edge points of one curve to the other one as discussed above, and this pair is then abandoned. After comparing the local minimum values, the pair to give the global minimum distance can be found. In the following step, to improve the accuracy of the final solution, this pair is computed again by using the NR method with the previous result as the initial value and 3 or 4 iterations to ascertain a good accuracy. Finally, the distances between all the endpoint pairs with one from each of of the two curves are also calculated and considered so that the case when the minimum distance is between endpoints cannot be missed.

4.4 Performance analysis

Fig. 4.15 illustrates the process of the minimum-distance calculation between two B-spline curves which are integrated from the point sets of the contour of bone ulna and radius. (a) shows the decomposition of the B-spline curve into Bézier subcurves. Each subcurve is differentiated from each other by color difference and enclosed in their corresponding bounding spheres. (b) shows the remaining subcurves after the first-level selection. (c) shows the pairs left after the second-level selection. (d) shows the last pairs rendering the minimum distance (d=9.39mm). Another two examples have minimum distance of 11.15mm and 16.02mm respectively, as shown in Fig. 4.16.

Table 4.1 lists the number of candidate pairs during the process. Taking the case shown in

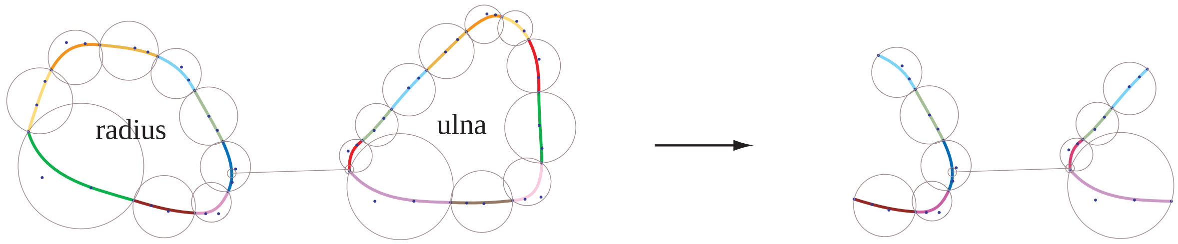

(a) Bézier subcurves with their boundary sphere

(b) after first level

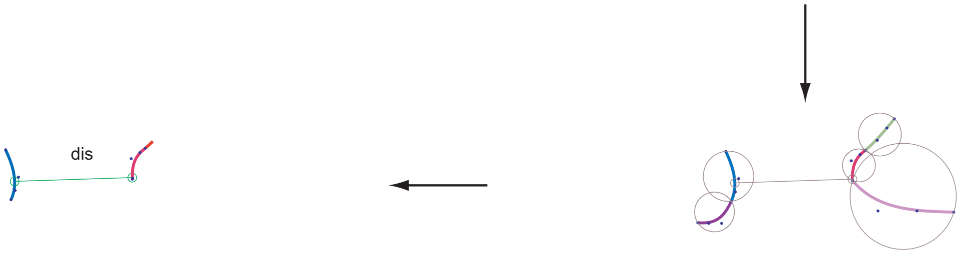

(d) minimum distance between two curves

(c) after second level

Fig. 4.15: Calculation process of the minimum distance.

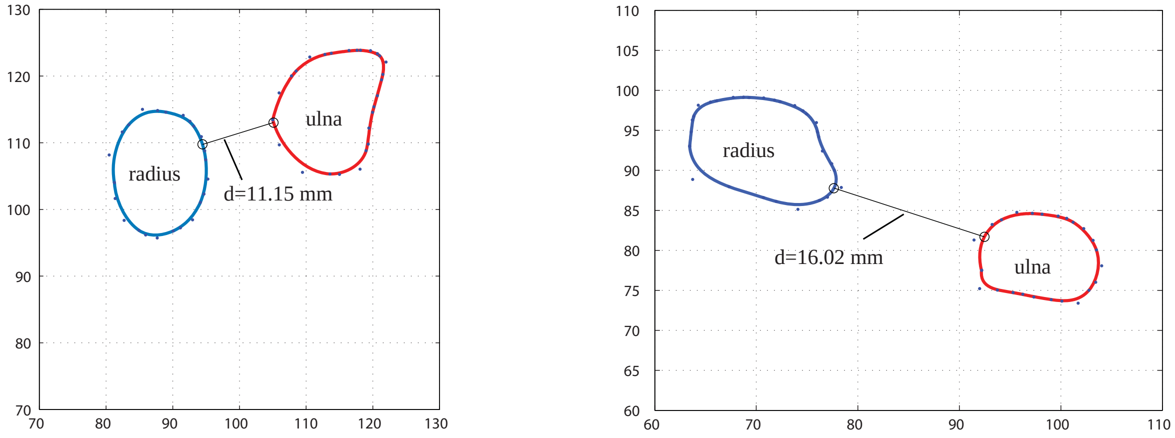

(a)

(b)

Fig. 4.16: Two examples of the minimum-distance calculation.

Fig. 4.15 as an example, the contour of bone ulna (object A) has 11 Bézier subcurves and that of bone radius (object B) has 9 Bézier subcurves, therefore the sum of possible pairs of Bézier subcurves are 99. After the determination of the bounding spheres of Bézier objects, bone ulna has 3 "valid" and 8 "invalid" control polygons, whereas bone radius has 5 "valid" and 4 "valid" ones. After the first-level selection the remaining "valid" pairs in total are 15, and this value goes down to 5 after the second-level selections. The finally left 5 candidate pairs are further processed with NR method.

Table 4.1: Data obtained during selections

Figure	Total pairs	Object A (ulna)		Object B (radius)		Remaining pairs after level 1	Remaining pairs after level 2
		"valid"	"invalid"	"valid"	"invalid"		
Fig. 4.15	99	3	8	5	4	15	5
Fig. 4.16 (a)	72	7	2	8	0	27	6
Fig. 4.16 (b)	80	6	2	5	5	25	13

Table 4.2 lists the corresponding total consumed time (based on 1.86GHz CPU and 1024 MB memory) and the individual time consumed in the pre-processing, selection levels and calculation with NR methods (including calculation of approximate local minimum distances and the final accurate global minimum distance). The last column shows the accuracy of the finally achieved results in 5 iterations.

Table 4.2: Consumed time and result accuracy

Figure	Total pairs (sec)	Pre-processing (sec)	Level 1 (sec)	Level 2 (sec)	Newton method (sec)	Accuracy
Fig. 4.15	0.518	0.286	0.006	0.073	0.153	6.9e-7
Fig. 4.16 (a)	0.593	0.305	0.004	0.152	0.131	1.3e-5
Fig. 4.16 (b)	0.613	0.332	0.004	0.095	0.181	6.2e-5

4.5 Distance between two forearm bones

With the algorithm described in Section **4.3**, a point pair between two B-spline curves can be found giving the shortest distance between two corresponding contours of bone ulna and radius recognized in one MRI slice. However, this distance calculation is limited to 2D slice pairs. Due to the complicated relative motion of bone radius rotating around bone ulna, the relative position between radius and ulna changes as a function of the pro-/supination angle φ, and thus also the value of shortest distance as well as its location varies with φ. To determine the shortest distance between the two relative rotating forearm bones (3D model), not only the minimum distance and its location need to be quantified, but also the change of the distance relative to the pro-/supination angles need to be clarified. Noting that the slices of ulna and radius remain almost coplanar during pro-/supination, this task can be achieved in the following steps:

1. Assuming that the MRI slices are close enough (in our application with a slice distance of $6-10$mm), the radius and ulna bones are divided in small cylindrical pieces whose

surface is approximated by a ruled surface with a pair of MRI slices as their ends and parallel edges in axial direction (Fig. 4.17).

2. Take point pairs with the shortest distance from the corresponding MRI slices (refer to Section **4.3.7**), and use their positions as initial values for the iteration in axial direction (step 3).

3. Calculate the shortest distance between each two corresponding segment pairs (one from bone ulna, one from bone radius), as well as between their adjacent segment pairs. For each pair of segment bodies, extend the search to its $\pm\ 5^\circ$ region along the spline curve, and compare the local shortest distances to get the point pair for the shortest distance within this region. Thereafter, update the point pair (Section **4.5.1**).

4. Repeat the same process for each pair and get the shortest distance between each bone pairs (green arrows in Fig. 4.17).

5. Compare the local shortest distances to get the shortest one, as shown by the red arrow in Fig. 4.17.

6. Repeat the procedure for each pro-/supination angle φ and keep the shortest distance of all.

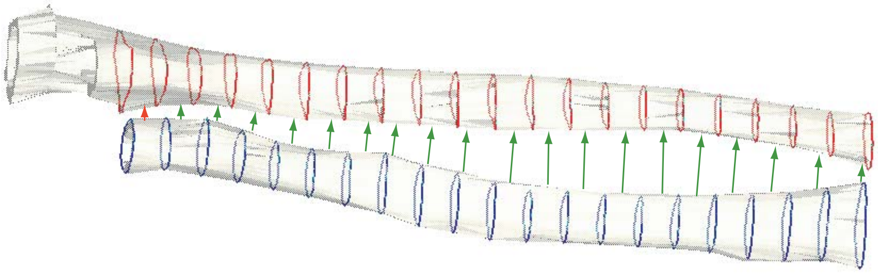

Fig. 4.17: Diagraph of the shortest distance calculation between forearm bones.

4.5.1 Distance between pairs of segmented bone bodies

In the present work, the surfaces of the forearm bones are simplified as ruled surfaces with line segments parallel to the axial direction, instead of curved surfaces on 2D slices, in order to reduce computational complexity. Here, one example will be explained to elucidate the process details (Fig. 4.18).

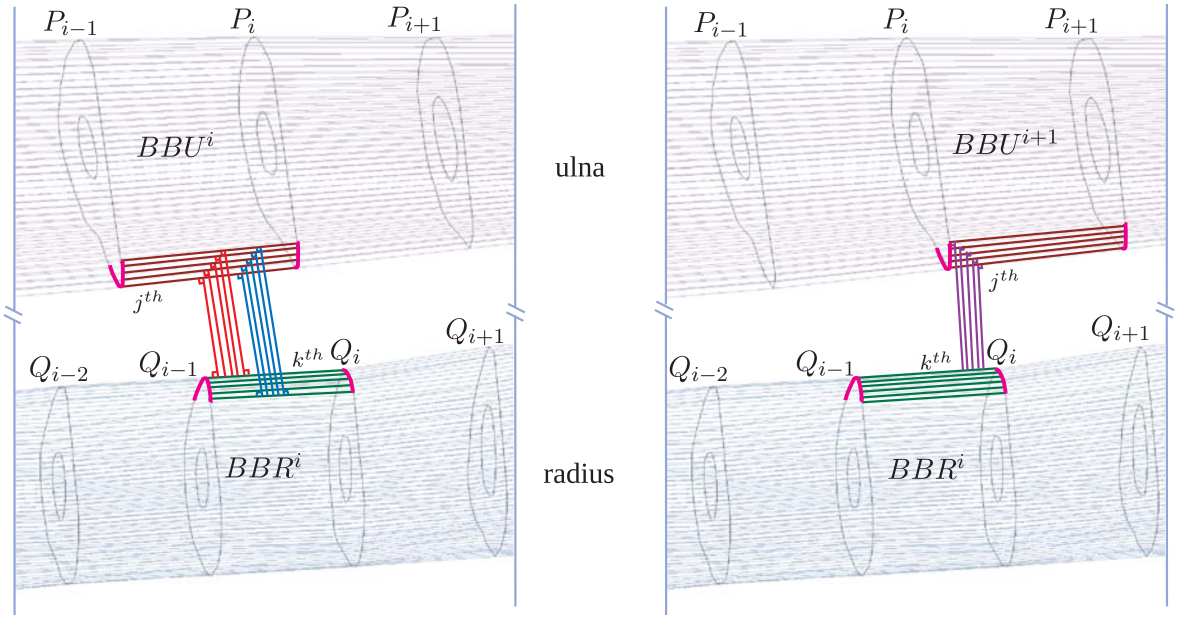

(a) distance between $P_{i-1}P_i$ and $Q_{i-1}Q_i$ (b) distance between P_iP_{i+1} and $Q_{i-1}Q_i$

Fig. 4.18: Distance calculation between two bone surfaces (violet: ulna, blue: radius), by simplifying bone surface as parallel segmented lines.

As shown in the figure, bone ulna is colored with violet, and bone radius is with light blue. P_{i-1}, P_i, P_{i+1} present the point sets of $(i-1)^{th}$, i^{th}, $(i+1)^{th}$ MRI cross-sections on bone ulna, and Q_{i-1}, Q_i, Q_{i+1} present the point sets of $(i-1)^{th}$, i^{th}, $(i+1)^{th}$ cross-sections on bone radius ($i = 1, 2, 3...L$, where L is the number of the cross-sections in fine MRI scans). The surfaces of bone ulna and radius are simplified as line arrays, presented by $P_{i-1}P_i$, P_iP_{i+1}, and $Q_{i-1}Q_i$, Q_iQ_{i+1} respectively, which connect the corresponding points on adjacent cross-sections. The i^{th}, $(i+1)^{th}$ segmented bone body of ulna is termed as BBU^i and BBU^{i+1}, and of radius as BBR^i and BBR^{i+1}, respectively.

Now the search for the shortest distance between bone body pairs, such as BBU^i and BBR^i, can be solved by calculating the shortest distance between line arrays $P_{i-1}P_i$ and $Q_{i-1}Q_i$, with steps as following:

1. Set u_{cur}^{i-1}, v_{cur}^{i-1}, u_{cur}^{i}, v_{cur}^{i}, u_{cur}^{i+1} and v_{cur}^{i+1} as the current path parameters of u (ulna) and v (radius) on $(i-1)^{th}$, i^{th}, $(i+1)^{th}$ MRI slices, where u_0^{i-1}, v_0^{i-1}, u_0^{i}, v_0^{i}, u_0^{i+1} and v_0^{i+1} are the initial point pairs calculated by the algorithm (Section **4.3**) for the shortest distance.

2. Use the initial values u_0^{i-1} and u_0^{i} for the path parameter u_{cur}^{i-1} and u_{cur}^{i} at beginning,

and then extend the path parameter within α=± 5° along an arc on the B-spline (highlighted with pink as shown in Fig. 4.18 and Fig. 4.19). Within the ± 5° arc region, $n_\alpha = 10$ points were taken at each contour curve which are evenly distributed on the curve. The point positions can be calculated based on their corresponding curve path parameter from the CurveJoint. Connecting the points which has the same increasing or decreasing path steps about the initial values u_0^{i-1} and u_0^i along the arc from the two adjacent slice contour, series corresponding line arrays between the two arcs can be obtained and form part of the surface of the bone ulna.

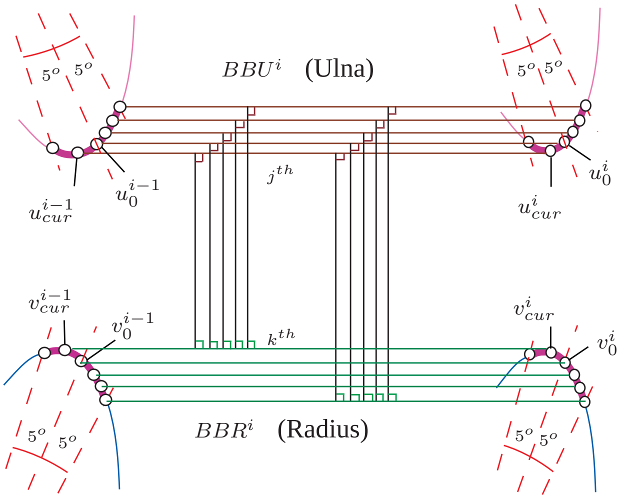

Fig. 4.19: Zoomed-in diagram of the distance calculation between two bone surfaces by simplifying bone surface as parallel segmented lines.

3. Repeat last step to v_{cur}^{i-1} and v_{cur}^i to form part of the surface of bone radius.

4. These two parts of bone surfaces are the regions of interest for studying the shortest distance between BBU^i and BBR^i. As the continuous bone surface is simplified as an array of discrete segment lines, the shortest distance between two bone surfaces is calculated by searching for the shortest distance between these series of segment lines, which can then be solved by a system of equations (see Eq. (4.27) to Eq. (4.33) further below).

5. For m segment lines BBU^i ($j = 1, 2, 3...m$) of the bone body and n segment lines BBR^i ($k = 1, 2, 3...n$) of the bone body, an order of $m * n$ calculations needs to be performed for the shortest distance between them, stored as $d_{cur}(i^{'})$. The calculation can be confined to the small region defined by the small ± 5° arcs about the initial values obtained on MRI slices.

6. Considering the relative motion between two bones, the shortest distance between a pair of the ulna segment body and the corresponding radius segment body, such as BBU^i and BBR^i, for example, could move to the adjacent pair of bone bodies such as BBU^{i+1} and BBR^i, as shown in Fig. 4.18(b). Therefore, one needs to calculate the shortest distance between BBU^{i+1} and BBR^i as well. The shortest distance is then stored as $d_{cur}(i^{''})$.

7. Take the shorter distance from $d_{cur}(i^{'})$ and $d_{cur}(i^{''})$, termed here as $d(i)$, to describe the distance between bone ulna to BBR^i.

8. Due to the relative motion between these two bones, the shortest distance of $d(i)$ can only exist between the pairs of BBU^i and BBR^i, BBU^{i+1} and BBR^i, but not between BBU^i and BBR^{i-1}, BBU^i and BBR^{i+1}. Therefore, the latter two pairs are not considered.

9. Rotating the bones to the next position, the obtained curve path parameters u_{cur}^{i-1}, u_{cur}^{i}, u_{cur}^{i+1}, v_{cur}^{i-1}, v_{cur}^{i} and v_{cur}^{i+1} from the previous position, are used to define the initial location for the calculation at this new position. The initial distance $d(i)$ is used as the reference for this step. Finding the shortest distance within $\pm$ 5° of the new region, and updating the new value and its location.

10. Repeat the whole processes for each pair of bone segments at each defined pro-/supination angle. A series of the shortest distance $d(i)$ between all available BBU^1, BBU^2 ...BBU^i ... BBU^L, and BBR^1, BBR^2 ...BBR^i ... BBR^L can be obtained, where L is the number of the cross-sections taken during fine MRI scans. The overall shortest distance d_{min} is then derived from this series.

4.5.2 Distance calculation between line segments

The distance calculation between two line segments is briefly discussed here. As shown in Fig. 4.20, if there are two lines defined as:

$$\textbf{Line 1} : P(u) = P_0 + u \cdot (P_1 - P_0) = P_0 + u \cdot \underline{s} \tag{4.27}$$

$$\textbf{Line 2} : Q(v) = Q_0 + v \cdot (Q_1 - Q_0) = Q_0 + v \cdot \underline{t} \tag{4.28}$$

the shortest distance between the two lines by taking the perpendicular vector $\underline{w}_c = \underline{w}(u_c, v_c)$

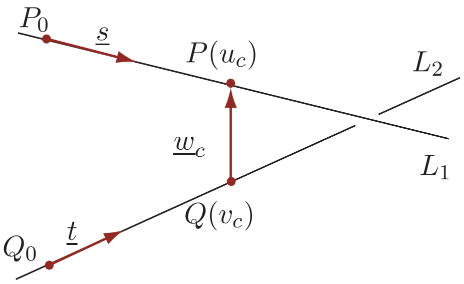

Fig. 4.20: Distance between two lines.

between the two line direction vectors $\underline{s}$ and $\underline{t}$, defined by:

$$\underline{s} \cdot \underline{w}_c = 0 \tag{4.29}$$

$$\underline{t} \cdot \underline{w}_c = 0 \tag{4.30}$$

and expressed by $P(u_c) - Q(v_c)$, and inserting this expression into (4.29)and (4.30), leading to

$$u_c = \frac{b \cdot e - c \cdot d}{a \cdot c - b \cdot b} \tag{4.31}$$

$$v_c = \frac{a \cdot e - b \cdot d}{a \cdot c - b \cdot b} \tag{4.32}$$

where $a = \underline{s} \cdot \underline{s}$, $b = \underline{s} \cdot \underline{t}$, $c = \underline{t} \cdot \underline{t}$, $d = \underline{s} \cdot \underline{w}_0$, $e = \underline{t} \cdot \underline{w}_0$, and $\underline{w}_0 = P_0 - Q_0$.

Then, the distance between them is:

$$d(L_1, L_2) = |P(u_c) - Q(v_c)| = \left| (P_0 - Q_0) + \frac{(b \cdot e - c \cdot d) \cdot u - (a \cdot e - b \cdot d) \cdot v}{a \cdot c - b^2} \right| . \tag{4.33}$$

It is to be noted here that the distance between line segments may not be equal to the distance between their extended lines, because the closest points for infinite lines could be outside the range of the segments. Therefore, after the determination of u_c and v_c for L_1 and L_2, the positions of the points need to be checked. If the points are inside the involved line segments, then they are the right answers for the two segment lines; if not, the minimum distance occurs at the endpoints of the segments [79].

4.6 Results of the minimum distance between forearm bones

As mentioned above, the location and value of the minimum distance between bones change during forearm rotation. Here, one example is analyzed in detail. Results of the shortest distance between two forearm bones at random rotational position are summarized.

Within the α=± 5° arcs along B-splines, n_α=10 points were taken at each contour curve which are evenly distributed on the curve. Taking more points can of course improve the calculation accuracy, but will require a longer processing time. 10 points were sufficient here for both good accuracy and efficiency.

As shown in Fig. 4.21, a list of the distances changing along bone axial direction at the rotational angle φ=82° is presented. Here, the green arrows represent the shortest distance between each bone pair BBU^i/BBU^{i+1} and BBR^i, and the red arrow, which exists only at the proximal portion, is the overall shortest distance at this pro-/supination angle (φ=82°). Other parameters, such as the rotational angle ($Ang\_phi[°]$), the calculation time ($time[sec]$), the shortest distance d_{min} (6.528mm) and the distance value d_i (i=1,2,...,20) between each bone pair, are also shown in the list. The plotted red and blue polygons are the boundary lines which are the trajectory of the shortest distance between two bones from proximal to distal portion.

Four more examples of the distance changing along axial direction at defined rotational angles are presented in Fig. 4.22. At sup45°, neutral, pro45°, pro70°, the shortest distance is 5.015mm, 3.125mm, 2.902mm and 2.061mm, respectively.

Fig. 4.23 plots the distance changing along the bone axial direction at five rotational angles, displayed with different colors. It can be observed that the distance changing is not regular, i.e. it has different profiles at different angles. In addition, the shortest distance exists always at the proximal portion. However, due to the limitation of the segmentation program and the resolution of MRI slices, the 3D bone model at the proximal and distal raidioulnar articulation are not complete, and therefore the distance at the articulation portion could not be exactly evaluated. The calculation was on the points which were actually very near to the articulation. Although there are some deviations due to this simplification, the results are actually quite close to the real anatomic parameters. In the future, a finer segmenting of the bone articulation would be of much interest.

Fig. 4.24 displays the shortest distance between two forearm bones during the rotational motion. The shortest distance achieves its minimal value at its maximal pronation position,

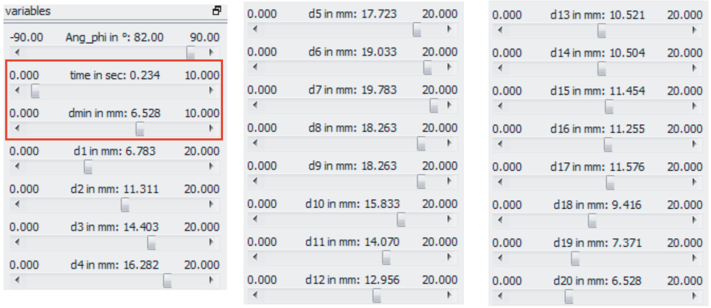

variables

-90.00 Ang_phi in °: 82.00 90.00

0.000 time in sec: 0.234 10.000

0.000 dmin in mm: 6.528 10.000

0.000 d1 in mm: 6.783 20.000

0.000 d2 in mm: 11.311 20.000

0.000 d3 in mm: 14.403 20.000

0.000 d4 in mm: 16.282 20.000

0.000 d5 in mm: 17.723 20.000

0.000 d6 in mm: 19.033 20.000

0.000 d7 in mm: 19.783 20.000

0.000 d8 in mm: 18.263 20.000

0.000 d9 in mm: 18.263 20.000

0.000 d10 in mm: 15.833 20.000

0.000 d11 in mm: 14.070 20.000

0.000 d12 in mm: 12.956 20.000

0.000 d13 in mm: 10.521 20.000

0.000 d14 in mm: 10.504 20.000

0.000 d15 in mm: 11.454 20.000

0.000 d16 in mm: 11.255 20.000

0.000 d17 in mm: 11.576 20.000

0.000 d18 in mm: 9.416 20.000

0.000 d19 in mm: 7.371 20.000

0.000 d20 in mm: 6.528 20.000

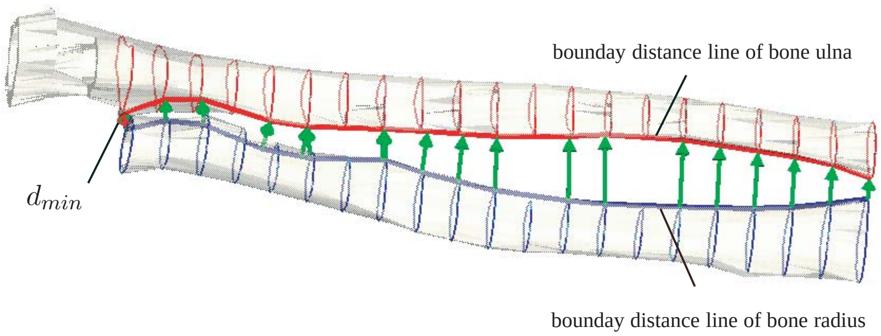

Fig. 4.21: Screenshot of the distance mapping between bone ulna and radius (green arrows are the distance between each bone pair, red arrow is the shortest one between bone ulna and bone radius at a rotation angle φ, here 82°).

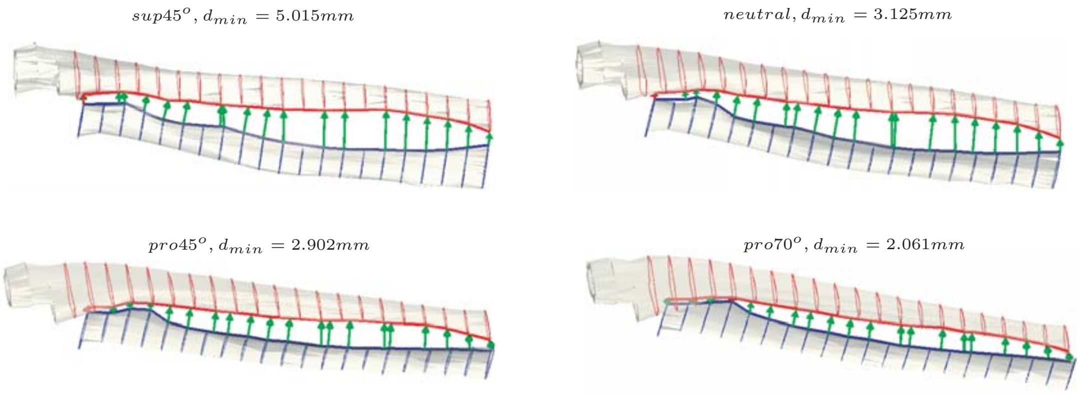

$sup45^o, d_{min} = 5.015mm$ $neutral, d_{min} = 3.125mm$

$pro45^o, d_{min} = 2.902mm$ $pro70^o, d_{min} = 2.061mm$

Fig. 4.22: Screen shot of the distance mapping between bone ulna and radius at defined rotational angles.

with a value of 1.281mm in this case. This figure includes additional five small screen shots above the red curve in order to give a clue of the location of the shotest distance more clearly. Starting from the supination 90°, the shortest distance between two bones exists at the radius proximal head, and after pronation 60° the shortest distance moves to the neck of the radius.

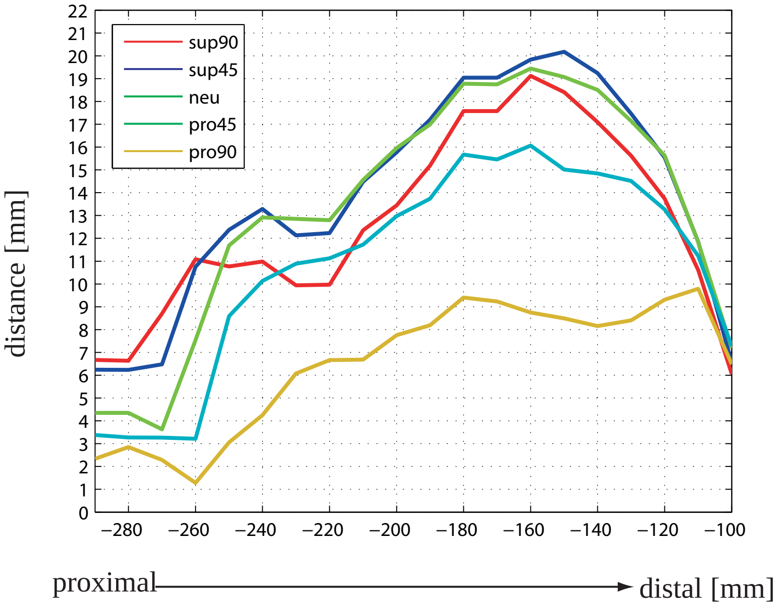

Fig. 4.23: Distance mapping between two forearm bones at five rotational positions.

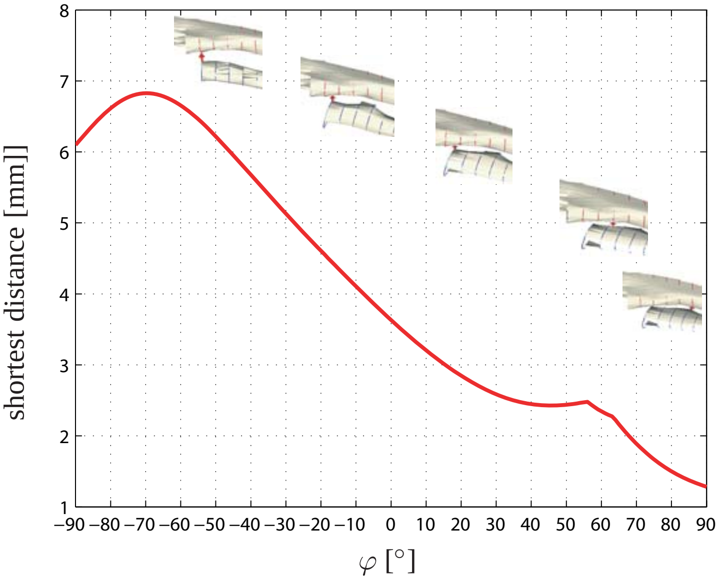

Fig. 4.24: Mapping of the shortest distance between bone ulna and radius during rotational motion.

Chapter 5

Angulated Forearm Bones

Forearm fractures are the most frequent fractures occuring at an extremity in the adult and the paediatric population [3]. Surgical treatments to bone fractures have risks: open reduction and internal fixation could end with non-union or failure of fixation, while closed reduction might leave malunion and functional deficits. These treatment failures can cause the impairment of the forearm rotational motion [5]. For example, in Fig. 5.1 a person who has impairment on the left forearm cannot achieve the same pronation rotational range as on the healthy side.

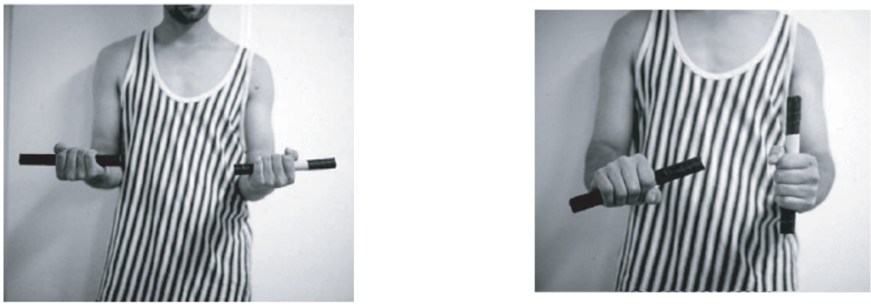

Fig. 5.1: Pronation on the impaired left forearm [3].

To understand the effect of the direction and magnitude of the angulation on forearm function, much cadaver and retrospective studies have been performed [3], [5], [80]. In this study, an agulated forearm kinematic model was developed based on the described 2DOF kinematic mechanism in order to evaluate how the angular deformities affect the impairment of rotational function. The 3D simulation is visualized by a GUI interface which allows one to predict the range of forearm motion's impairment and possible medical treatment.

As we did not have direct access to patients with forearm fractures, the geometrical data used in this chapter were taken from a literature [3]. We examined two examples by using this extended angulated kinematic model, and compared the predicted results with literature values.

5.1 Angulated forearm kinematic model

The present approach is based on the method of Weinberg et al., who presented a kinematic model with a vectorial compensation system to illustrate the deformed bones and developed a computing procedure to predict the impairment [3], [23]. In this work, the method of Weinberg et al. is extended by using the 2DOF kinematic mechanism described in Section **2** and inserting an additional vector for each angulation. Thus, each angulated bone is treated by two partial vectors and is embedded on the 2DOF surrogate mechanism motion. In the following, three cases are analyzed: angulated ulna, angulated radius and both angulated.

Fig. 5.2 shows the angulated forearm model, where the new vectors $\underline{r}_{11}$ and $\underline{r}_{12}$ relate to the angulated ulna, while the other two vectors $\underline{r}_{31}$ and $\underline{r}_{32}$ correspond to the angulated radius. The geometric parameters k_1^u, k_2^u, k_3^u, k_1^r, k_2^r, k_3^r are local components to present the location of the angulation, which characterize it in the axial, sagittal and frontal plane in the local coordinate of the fractured bone.

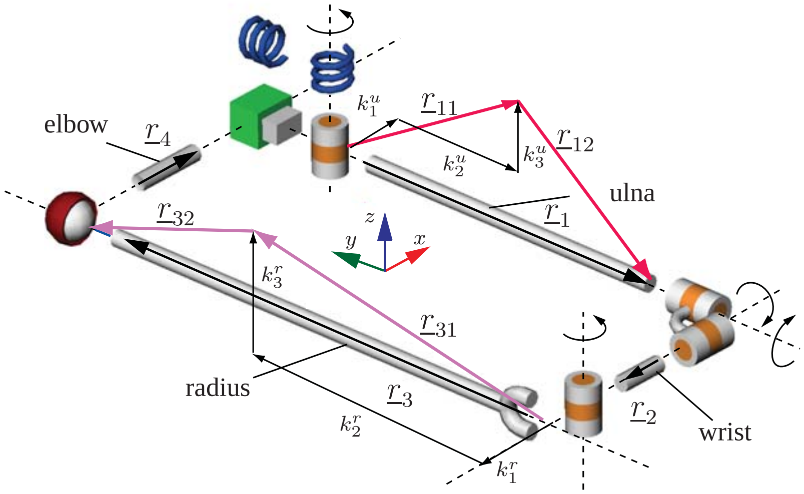

Fig. 5.2: Angulated forearm mechanism.

The vector coordinates of $\underline{r}_{11}$, $\underline{r}_{12}$, $\underline{r}_{31}$, $\underline{r}_{32}$ are in the home (supination) position:

$$\underline{r}_{11}^0 = \begin{bmatrix} k_1^u \\ -k_2^u \\ k_3^u \end{bmatrix} \; ; \; \underline{r}_{12}^0 = \begin{bmatrix} -k_1^u \\ l + k_2^u \\ -k_3^u \end{bmatrix} \; ; \; \underline{r}_{31}^0 = \begin{bmatrix} -k_1^r \\ k_2^r \\ k_3^r \end{bmatrix} \; ; \; \underline{r}_{32}^0 = \begin{bmatrix} k_1^r \\ l - k_2^r \\ -k_3^r \end{bmatrix} \; ; \tag{5.1}$$

where l is defined again as the distance from radial head to ulnar styloid. By rewriting the loop closure condition Eq. (2.8) using the angulated vectors $\underline{r}_{11}, \underline{r}_{12}, \underline{r}_{31}, \underline{r}_{32}$ instead of $\underline{r}_1$ and $\underline{r}_3$, the deformity of one or both bones can be integrated into the mathematical formulation described in Section **2.2.3**.

Fig. 5.3 shows as an example radiography of a deformed radius. The parameters $k_i^{u/r}$ are obtained directly from the X-ray picture, as well as the sagittal k_1^r in the lateral view and the frontal k_3^r in the a.p. view. The local y component k_2^r is taken as the distance from the radial head to the projection of point C at the length direction of bone radius, where point C is the crossing point of the two middle axes h and i of the deformed bone.

Fig. 5.3: Measured parameters of deformity on orthogonal radiographs [3].

5.2 Determination of maximal pronation angle

The maximal pronation angle can be determined via two different methods: (1) by calculating the minimal distance between the vectors that represent bone ulna and radius in the angulated kinematic model and stopping the motion when this distance is less than a given threshold value; or (2) by calculating the minimal distance between the two bone surfaces of ulna and radius in the model and applying the same stopping criterion as in (1).

5.2.1 Method 1: distance between vectors

The prediction of the influence of angulations on the range of forearm motion using vector polygons can be performed as follows:

1. Calculate the distance between the bones of the healthy forearm during its rotational process, that is the distance between vectors $\underline{r}_1$ and $\underline{r}_3$ representing bone ulna and radius in the kinematic model (Fig. 2.7). The resulting distance $d_{healthy}$ results as a function of the pronation angle φ.
2. Calculate the minimal distance d_{min} from $d_{healthy}(\varphi)$ at its maximal pronation position, and set this value equal to the minimum allowable distance for the angulated forearm. This assumption has been proved in a study [23] by taking the influence of the bending of the bones to the range of motion of forearm into consideration.
3. Calculate the minimal distance between the polygons of the angulated bone pairs (Fig. 5.2). In the case of one fractured bone, the distance calculation is between either the segment along $\underline{r}_{11}$ and $\underline{r}_{12}$ and the segment along $\underline{r}_3$ for angulated ulna, or between the segment along $\underline{r}_{31}$ and $\underline{r}_{32}$ and the segment along $\underline{r}_1$for angulated radius. The results are denoted by d_1 and d_2 as functions of φ. In the case of both angulated bones, the distance calculations need to examine four four segment pairs: between $\underline{r}_{11}$ to $\underline{r}_{31}$, $\underline{r}_{11}$ to $\underline{r}_{32}$, $\underline{r}_{12}$ to $\underline{r}_{31}$ and $\underline{r}_{12}$ to $\underline{r}_{32}$. The results are denoted by $d_1(\varphi)$, $d_2(\varphi)$, $d_3(\varphi)$, $d_4(\varphi)$, respectively.
4. Find the minimal distance $d_{deformed}(\varphi)$ from all the values obtained from step3.
5. When $d_{deformed}(\varphi)$ reaches the minimal distance of healthy bones d_{min}, the calculation stops. The corresponding φ is the seeked maximal pronation angle for the deformed forearm.

During the rotational process of radius with respect to ulna, the distances between the forearm bones is rendered as a function of the pro-/supination angle. The program will stop when the distance between the vectors reaches the minimal distance of the healthy arm.

Based on this angulated kinematic model, a simulation tool for the angulated forearm can be established, as shown in two examples. The program combines MATLAB and MOBILE [48], which are used to implement the user interface (Fig. 5.4 and Fig. 5.5) and to implement the mechanism model and simulate the forearm motion (Fig. 5.6), respectively.

As shown for the examples in Fig. 5.4 (both bones angulated) and Fig. 5.5 (one bone angulated), on the interface the input values include:

1. Choosing the deformed bones: ulna, radius or both;
2. Entering the geometric parameters of bone length and width;
3. Entering the maximal pronation angle of the healthy forearm;
4. Entering fracture parameters k_i extracted from the radiographs (refer to literautre [3]).

Output results include 3 diagrams:

1. Diagram 1 at the left bottom presents the vectorial compensation system illustrating the deformed bones.
2. Diagram 2 at the right upper plots the distance between bones as a function of the pro-/supination angle. The diagram contains the distance plots between:
   a) two healthy bones (red in Fig. 5.4 and Fig. 5.5)
   b) the angulated ulna proximal end and the angulated radius proxiaml end (blue in Fig. 5.4)
   c) the angulated ulna distal end and the angulated radius proximal end (green in Fig. 5.4)
   d) the angulated ulna proximal end and the angulated radius distal end (yellow in Fig. 5.4)
   e) the angulated ulna distal end and the angulated radius distal end (pink in Fig. 5.4)
   f) the angulated radius distal end and the healthy ulna (green in Fig. 5.5)
   g) the angulated radius proximal end and the healthy ulna (blue in Fig. 5.5)

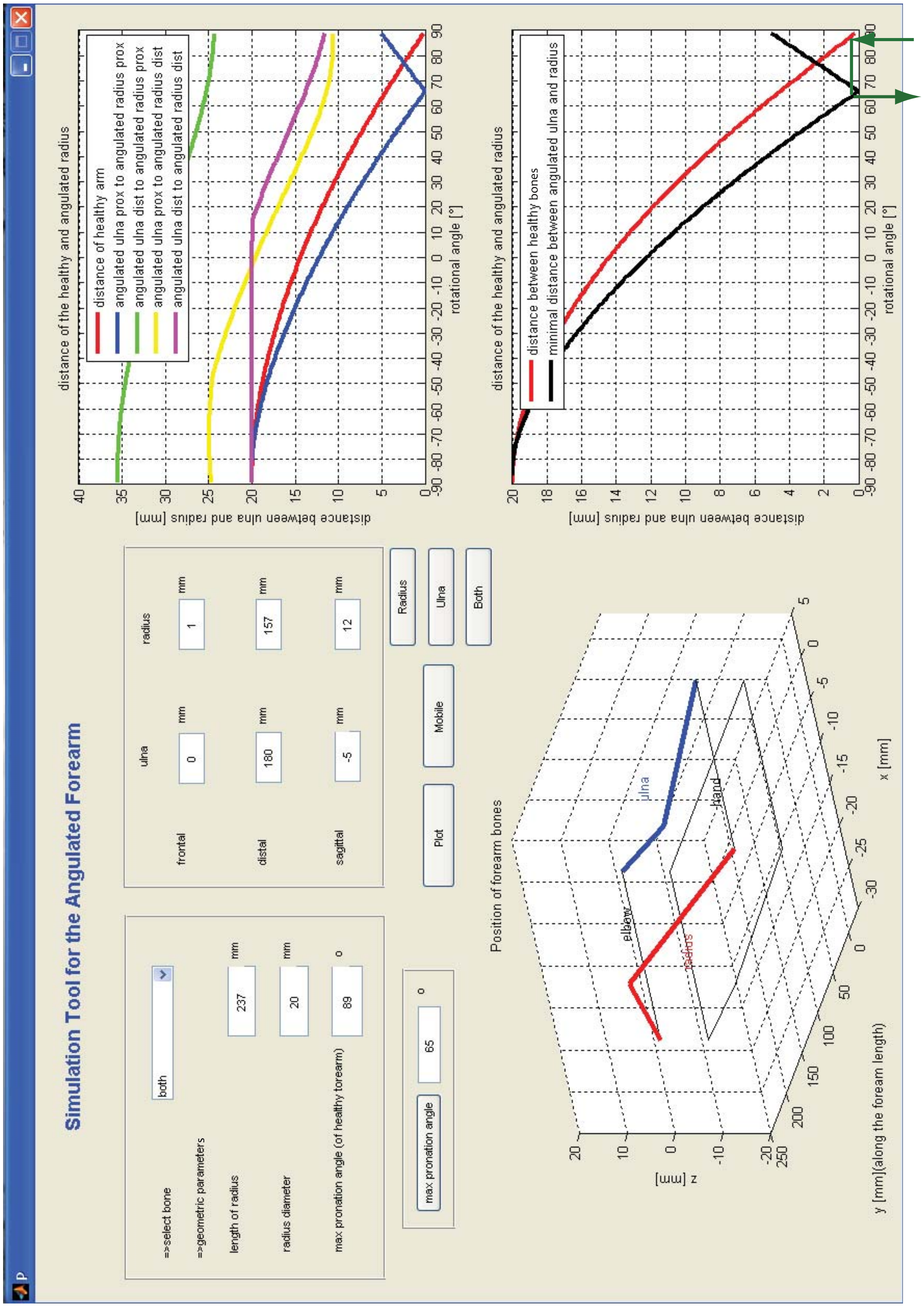

Simulation Tool for the Angulated Forearm

=>select bone: both

=>geometric parameters

length of radius: 237 mm

radius diameter: 20 mm

max pronation angle (of healthy forearm): 89 °

max pronation angle: 65 °

	ulna		radius	
frontal	0	mm	1	mm
distal	180	mm	157	mm
sagittal	-5	mm	12	mm

Fig. 5.4: User interface to calculate the distance between two angulated bones.

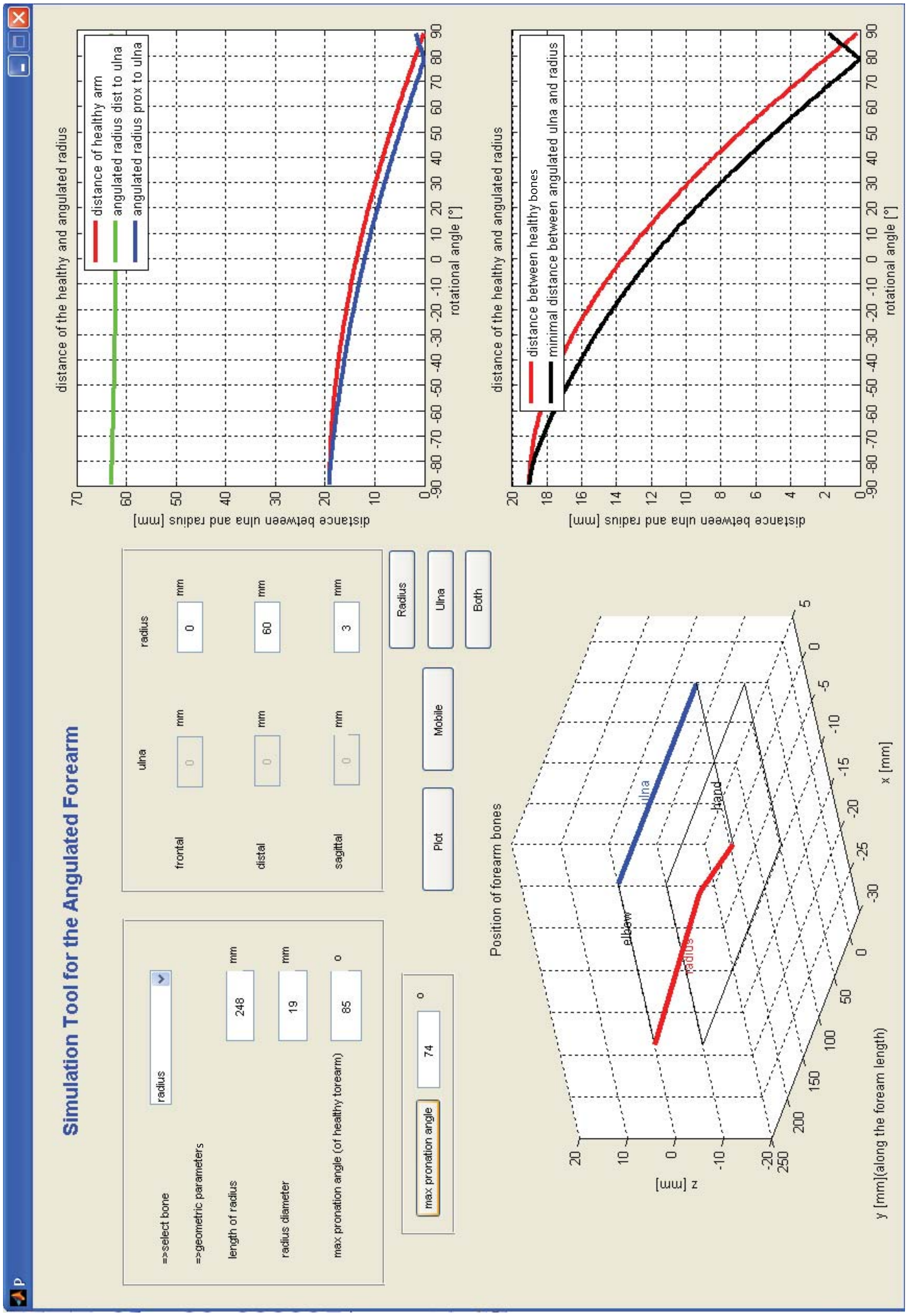

=>select bone: radius

=>geometric parameters

length of radius: 248 mm

radius diameter: 19 mm

max pronation angle (of healthy forearm): 85 o

max pronation angle: 74 o

	ulna		radius	
frontal	0	mm	0	mm
distal	0	mm	60	mm
sagittal	0	mm	3	mm

Fig. 5.5: User interface to calculate the distance between angulated radius and healthy ulna.

3. Diagram 3 on the right bottom plots the minimal distance between healthy bones $d_{healthy}(\varphi)$ (red) and angulated bones $d_{deformed}(\varphi)$ (black) along pro-/supination angles.

The procedure for determining the maximal pronation angle is illustrated in the following by the example of Fig. 5.4. First, the distance at maximal pronation angle of the healthy bone structure at 89° is defined as the minimal allowable distance. By choosing the option "max pronation angle", the distance at maximal pronation angle of healthy bones is shifted horizontally until it intersects the minimal distance curve of the deformed bones. Pulling down vertically this point until it intersects the x-axis and gives the sought result, in this example approximately 65°.

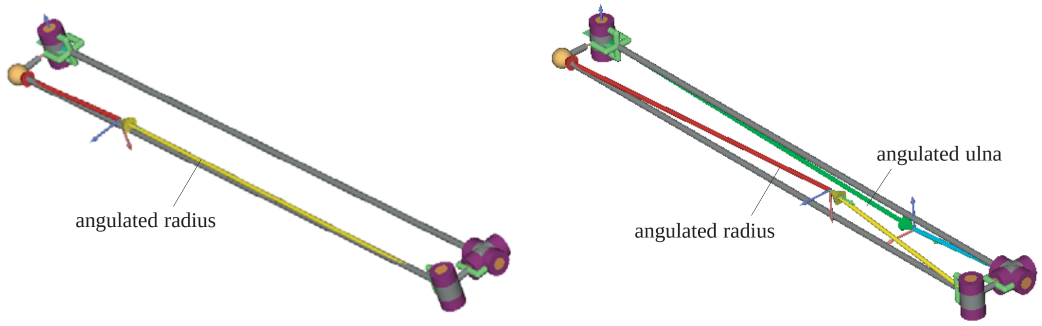

(a) radius with fracture

(b) both bones with fracture

Fig. 5.6: Simulated 3D model with the angulated vector.

Based on the program, the reference data of fractured bones obtained from a clinical report [3] were simulated. Data from 17 people having different ages and different impairment of bones were analyzed. Pronation and supination were measured clinically with a goniometer. The possible pronation of the healthy side was included as a value representing the minimal distance of both forearm bones on pronation. The results from the literature and by our simulation are compared in Table 5.1. This table contains: the bone length and width (column "Patient"); fractured bone(s) (column "Bone"); fractured parameters in the literature (columns "Radius" and "Ulna"); clinically measured maximal pronation angles of healthy and fractured bones (column "Measured angle"); simulated maximal pronation angle in the literature (column "Liter.data"); simulated maximal pronation angle using the 2DOF model with stiffness coefficient ratios derived from the correlation with bone length based on two measurements (column "Simulation").

All 17 samples were analyzed based on the angulated model and the predicted stiffness coefficient ratios, and results are summarized on Table 5.1. It is encouraging that the computed

Table 5.1: Clinical measurements and simulated results are compared.

	Patient		Bone	Radius			Ulna			Measured angle (°)		Liter. data	Simulation	
	l(mm)	b(mm)		k_1 (mm)	k_2 (mm)	k_3 (mm)	k_1 (mm)	k_2 (mm)	k_3 (mm)	α healthy	α deformed	α sim	Cυ/Cs	α sim
	237	20	Both	1	157	12	0	180	-5	89	65	62	172	65
	248	19	Radius	0	60	3				85	75	74	192	74
	269	25	Radius	5	195	3				90	85	81	231	80
	195	19	Ulna				5	95	3	62	20	23	95	25
	195	15	Both	2	50	2	5	50	0	85	70	65	95	66
	275	25	Both	0	130	4	1	130	0	60	33	40	242	39
	250	25	Both	-5	92	-5	5	100	12	90	70	67	196	66
	208	19	Ulna				0	80	4	65	45	46	119	48
	193	16	Radius	-15	62	3				85	65	65	92	65
	265	26	Radius	5	180	4				85	80	75	223	77
	230	17	Ulna				1	110	3	80	70	71	160	60
	235	21	Radius	5	120	-2				80	80	88	169	87
	235	21	Both	4	110	0	2	110	0	85	85	85	169	85
	218	19	Radius	3	70	8				85	55	46	138	49
	253	21	Radius	0	95	8				85	55	47	201	49
	185	15	Radius	3	95	7				85	75	76	77	75
	225	21	Radius	0	100	3				85	70	70	150	71
$\overline{X}$	233	21		1	109	4	3	107	3	80	65	65	166	65
S.D.	27	3		6	44	4	2	38	6	9	17	17	49	16

results are very well consistent with those measured in the clinical investigations and comparable to those in the literature. This indicates the potential applicability of the proposed angulated model in clinical application. The possible reasons for the small discrepancies between our simulated data and measured ones can result from the measurement noise, or the computational method, which could be extended to take account of the actual surface contacts of the involved joint interconnections.

Hereby, as the ratio of the stiffness coefficients c_s and c_ϑ is obtained from the correlation between the ratio and bone length based on two measurememts, its accuracy is to some degree limited, although the results show a good matching with the experimentally measured values, which shows their applicability. Further analysis with larger subject sets may confirm this empirical finding, which is a topic of future research outside of the scope of this thesis

5.2.2 Method 2: distance between bone surfaces

In method 1, the distance calculation was based on straight vectors without regard of the actual surface geometry of the bones. Therefore, in this section, a second method to determine the maximal pronation angle is described which takes into account the bone surface. In this method, the calculation stops when the shortest distance between the surfaces of bone ulna and radius reaches a minimal threshold, signalling a collision.

Input values in this method are, as in method 1:

1. Choosing the deformed bones: ulna, radius or both.
2. Entering the geometric parameters of bone length and width.
3. Entering the fracture parameters k_i extracted from the radiographs [3].

Two examples analyzed by using method 1 are computed here again.

Example1: angulated radius
Geometric parameters: length $l = 253mm$, width $b = 21mm$.
Fracture parameters of radius: $k_1^r = 0mm$, $k_2^r = 95mm$, $k_3^r = 8mm$.

In this case, bone ulna is healthy and bone radius is angulated at a given position into two parts: the proximal portion (pink) and the distal portion (blue) (Fig. 5.7). With the algorithm to calculate the minimal distance between two bone surfaces as described in Section **4**, the minimal distances between the healthy ulna and each of the two angulated radius parts can be calculated. The red arrow represents here the minimal distance between bone ulna and fractured radius at current position.

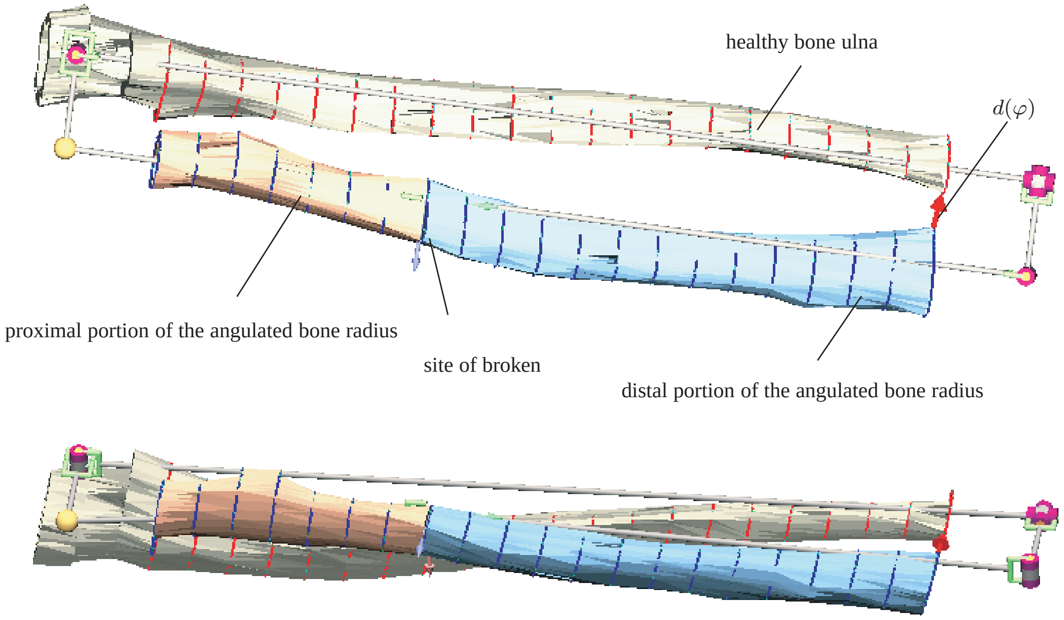

Fig. 5.7: Simulated angulated bone model for example 1 with bone surface in a.p.view and side view (radius in fracture).

The minimal distance as the function of the pro-/supination angle is plotted in Fig. 5.8. Clearly, at pronation 53° the bone radius crosses bone ulna, describing the position where the angulated bone radius achieves its maximal pronation relative to the healthy bone ulna.

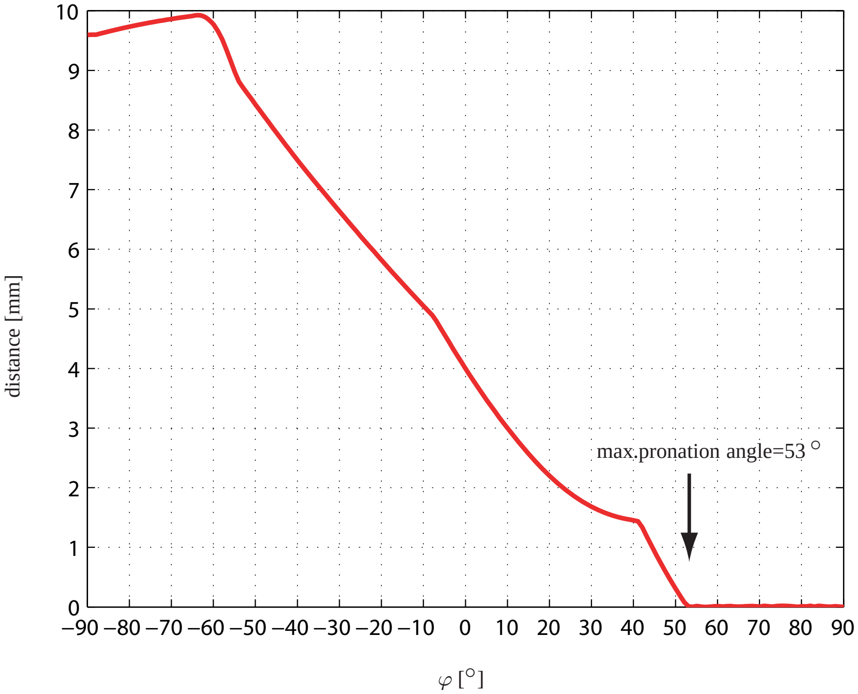

Fig. 5.8: Distance between forearm bones as a function of pro-/supination angle for example 1.

Example2: both radius and ulna angulated

Geometric parameters: length $l = 250mm$, width $b = 25mm$.

Fracture parameters of ulna: $k_1^u = 5mm$, $k_2^u = 100mm$, $k_3^u = 12mm$.

Fracture parameters of radius: $k_1^r = -5mm$, $k_2^r = 92mm$, $k_3^r = -5mm$.

In this case, both bones are angulated. With the same procedure as described in the first example, the minimal distance between two fractured bones is illustrated by the red arrow in Fig. 5.9. The minimal distance as a function of the pro-/supination angle is shown in Fig. 5.10. Here, at pronation 67°, bone radius crosses ulna, where the angulated bone radius achieves its maximal pronation with respect of bone ulna.

The two samples discussed above were analyzed using both methods 1 and 2. The results are compared with clinical values as shown in Table 5.2. Both simulations show a small deviation from anatomical data, and the 2^{nd} method seems comparatively better, which is

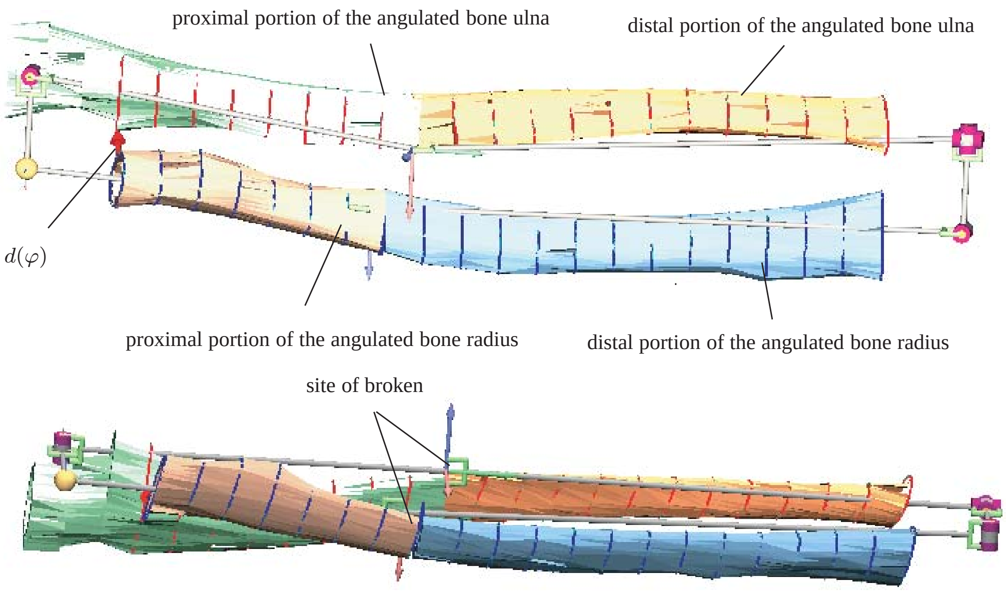

Fig. 5.9: Simulated angulated bone model for example 2 with bone surface in a.p.view and side view (both bone in fracture).

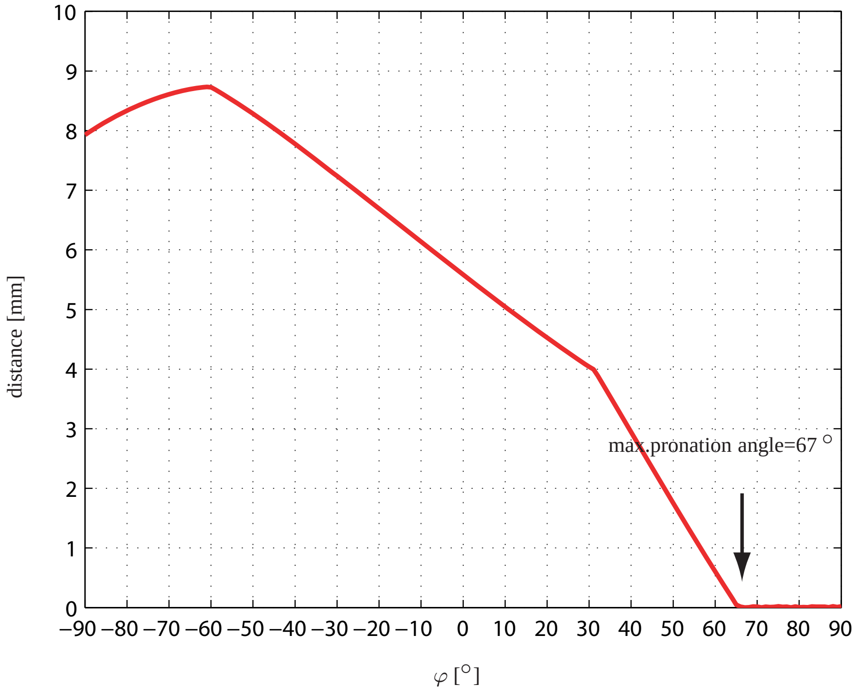

Fig. 5.10: Distance between two angulated forearm bones as a function of por-/supination angle for example 2.

reasonable since the irregular bone shape is considered in this method. As we do not have measuremements with subjects featuring fractures, the 3D angulated bone geometry is actually obtained by manually separating the bone structure from a fine MRI scan into two partial bones at a given position defined by the clinical parameters. It is believed that the accuracy could be improved if the analysis would be based on the true deformed forearm structures.

Table 5.2: Clinical measurements and simulated results are compared with method 1 and method 2.

Patient		**Bone**	**Radius**			**Ulna**			**Pronation angle (°)**		**Method 1 (°)**		**Method 2 (°)**	
l(mm)	b(mm)		k_1 (mm)	k_2(mm)	k_3(mm)	k_1 (mm)	k_2(mm)	k_3(mm)	α_{healthy}	α_{deformed}	α_{sim}	$\alpha_{\text{difference}}$	α_{sim}	$\alpha_{\text{difference}}$
253	21	Radius	0	95	8				85	55	50	5	53	2
250	25	Both	-5	92	-5	5	100	12	90	70	66	4	67	3

Chapter 6

Summary and Outlook

Recent years have seen the substantial increase of investigations on forearm pro-/supination motion. These studies are mainly motivated by three aspects: the desire for kinetostatically consistent replacement joints at the elbow, the need for biofidelic computer models and the clinical interest in comparing normal and pathological motion for better therapy planning. In this thesis, motivated by the potentially wide application possibilities of computer simulations in the clinical treatment of forearm, an in-vivo kinematic study of forearm rotation based on a 2DOF kinematic mechanism has been performed with data from magnetic resonance images. The main contributions of this work are:

1. Parameter fitting for a two-degrees-of-freedom surrogate mechanism for pro-/supination based on MRI scans.

The basis of this contribution is a special surrogate mechanism for human pro-/supination comprising two degrees of freedom proposed in [24]. The surrogate mechanism consists of a closed kinematic chain with four joints and two degrees of freedom. The prismatic and revolute joint lie on the proximal end of bone ulna, representing a small lateral swaying and a light dislocation of the ulna bone with respect to the humerus, respectively. The revolute joint at the distal end of bone radius describes the aperture between bone ulna and radius. The Hooke joint represents the real physical radio-ulnar joint at the distal end, consisting of the actual pro-/supination angle and the torsional angle. The spherical joint represents the radial head at the proximal end of bone radius. At the humero-ulnar joints, two degrees of freedom are bound by virtual springs with corresponding spring stiffnesses, which characterize the coupling elastic effects at these joints.

As a new contribution, model parameters were obtained automatically by a fitting process based on MRI images. At the beginning, two kinds of MRI measurements were performed: fine static scans and dynamic motion scans. Fine scans comprise numerous slices and were performed in order to determine a good approximation of the bone geometry for reference in the dynamic fitting. The motion scans record the forearm rotational motion under different torque conditions at a few rotational positions (maximum supination, 45° supination, neutral, 45° pronation and maximum pronation) and at a few (five or seven) cross-section positions along the forearm length at each rotational angle, allowing for quick scans.

The fitting of the model parameters (link lengths and spring coefficients) is conducted via an optimization loop by searching for the minimal square error between the simulated positions of the bone-marrow centers and those obtained from MRI measurements. In this process, the self-calibration feature of this model enabled the optimization of the absolute location of the surrogate mechanism with respect to the MRI reference frames, as well as the location of the bone marrow centerline with respect to the links.

The good coincidence of simulated results to the observed motion rendered an insight of the application of this model in the functional anatomy of the lower arm without surgical interventions. Furthermore, the results under various loading conditions demonstrated the applicability of this model under different torque conditions in reality. Finally, to make the model user-friendly, the simulation of the forearm motion was visualized in 3D effect at the interface of the object-oriented multibody program library MOBILE.

As shown, the 2DOF model yields more realistic results than the fixed-axis model. By comparing the relative pose of the radius with respect to ulna as a finite helical axis (FHA), results show that the motion of bone radius with respect to ulna does not correspond to a pure fixed-axis rotation, but that it also contains a translation along the screw axis.

2. Distance calculation between forearm bones during rotational motion.

The distance between two forearm bones during rotation varies at different axial positions as well as at different pro-/supination angles. When it is zero (e.g. in angulated bones) the bones touch each other and the pro-/supination motion is stopped. The investigation of the distance change during the rotational motion thus is valuable to evaluate the effect of angular deformities on forearm kinematics, and to predict the maximal rotational angle by forearm fractures. In this research, the distance calculation was firstly performed in cross-sectional plane, and then this result was employed for distance computation in the full 3D model.

In the cross-sectional plane, the shapes of real bones were considered, and the corresponding outer contours (obtained from MRI slices) were represented by closed B-spline curves, and the minimum distance between two 2D spline curves was computed by using a fast and robust method described in [67]. This algorithm was carried out firstly by decomposing both of the spline curves into a number of their piecewise-Bézier subsets. Candidate pairs from the subsets were extracted based on a two-level selection process. The first-level selection used upper-lower bounds of the Bézier subcurves to do the filtration. The second-level selection was based on the spatial relationship between a pair of Bézier curves. After obtaining the candidate pairs, an iterative multidimensional Newton-Raphson method was applied on them in order to approximately calculate the corresponding locally minimal distance. In the last step, all local minimal distances were compared to provide the overall minimal distance.

In order to obtain the shortest distance between the 3D model of the two rotating forearm bones, the surfaces were simplified as chains of small ruled-surface cylinders parallel to the bone axis with thickness equal to the distance between two fine scans and end faces with boundaries equal to the outer contours of the cross-sectional scans where the density of the axially parallel lines is chosen by a discretization of the contour plots. Starting with the result obtained in the 2D model as the initial position, an arc of $\pm\alpha$ (in our case $\alpha = 5°$) about the minimal distance footpoint of each cylinder was chosen and the minimal distance of all pairs of such selected axial lines was determined, from which the shortest distance between any neighboring pair of cylinders and thus the overall minimal distance between the bones could be determined. Based on this minimal distance and the allowed threshold before the bones touch each other, the maximal pronation angle can be determined.

3. Distance calculation for deformed forearm bones.

Forearm fractures are common in both adult and paediatric population. The prediction of the range of motion due to forearm impairment is thus highly valuable for the medical training or surgical treatment. The aforementioned 2DOF kinematic mechanism was extended to consider also malunited forearm bones after fracture, and a computer program was developed to simulate the maximal pronation angle for given angular deformities and their positions within radius and ulna.

The maximal pronation angle was determined via two different methods: (1) by calculating the minimal distance between vector segments representing bone ulna and radius in an angulated kinematic model; (2) by calculating the minimal distance between the surfaces of bone ulna and radius with the 3D surface segmentation by MRI scans. As we had no test subjects with fractured bones available for this work, the second method was tested by virtually separating a healthy bone structure from a fine MRI scan into two misaligned bone segments.

Seventeen examples were analyzed by using the first method, and two of them were checked with the second method. Both results show a very small deviation from anatomical data. The second method seemed comparatively better than the other one, which is reasonable since the irregular bone shape gives a better notion of collision.

Altogether, this work has developed a method to automatically determine the model parameters as well the relative location of the bone geometry with respect to the links of an elasto-kinematic 2DOF surrogate model for forearm pro-/supination. The methodology has proved to be suitable to describe the in-vivo forearm kinematics with a good accuracy and reliability. Moreover, the minimal distance between ulna and radius during forearm motion was determined for both the cases of healthy and fractured forearm bones. A fractured forearm model was developed based on the 2DOF mechanism, which can be used to predict the range of motion of forearm impairment in several examples. To facilitate the application of the model in the mechanical training and surgical treatments, a 3D user-friendly visualisation interface was developed with the multibody programming library MOBILE [48].

Outlook

The present work validates the theoretical derivations on a single subject only. Future studies could assess a larger subject pool in order to further validate the present preliminary results.

In this study, only a geometrical database for healthy forearm bones was utilized. The investigation on fractured bones was by manually separating a healthy forearm and locating them at a relative deformed angle. Future studies could consider real malaligned MRI scans to prove the applicability of the model in clinical treatment.

Finally, the bone motion interpolation method using a 2DOF surrogate mechanism could be validated using dynamic MRI scans or fluoroscopy recordings.

Bibliography

[1] D. J. Fuller and C. J. McChullogh. Malunited fractures in children. *Journal of Bone and Joint Surgery*, 33:364–367, (2000).

[2] J. Oskam, J. Kingma, and H. J. Klasen. Fracture of the distal forearm: Epidemiological developments in the period 1971-1995. *Injury*, 29(5):353–355, (1998).

[3] P. Kasten, M. Krefft, J. Hesselbach, and A. M. Weinberg. Computer simulation of forearm rotation in angular deformities: A new therapeutic approach. *Injury*, 33:807–813, (2002).

[4] H. J. Kim, J. H. Yi, J. W. Jung., D. W. Cho, R. V. Riet, and I. H. Jeon. Influence of forearm rotation on proximal radioulnar joint congruency and translational motion using computed tomography and computer-aided design technologies. *Journal of Hand Srugery.*, 36(5):811–815, (2011).

[5] R. R. Tarr, A. I. Garfinkel, and A. Sarmiento. The effects of angular and rotational deformities of both bones of the forearm: An in vitro study. *The Journal of Bone and Joint Surgery*, 66:65–70, (1984).

[6] N. Ladislav, J. Linas, and D. E. Charles. Correction of forearm malunion guided by the preoperative complaint. *Clin Orthop Relat Res*, 466:1419–1428, (2008).

[7] R. R. Bindra, R. J. Cole, K. Yamaguchi, B. A. Evanoff, T. K. Pilgram, L. A. Gilula, and R. H. Gelberman. Quantification of the radial torsion angle with computerized tomography in cadaver specimens. *Journal of Bone and Joint Surgery*, 79(6):833–837, (1997).

[8] C. E. Dumont, L. Nagy, D. Zieglera, and C. W. Pfirrman. Fluoroscopic and magnetic resonance cross-sectional imaging assessments of radial and ulnar torsion profiles in volunteers. *Journal of Hand Surgery*, 32(4):501–509, (2007).

[9] L. Nagy, L. Jankauskas, and C. Dumon. Correction of forearm malunion guided by the preoperative complaint. *Clin Orthop Relat Res*, 466(6):1419–1428, June 2008.

[10] P. Boileau and G. Walch. The three-dimensional geometry of the proximal humerus - implications for surgical technique and prosthetic design. *Journal of Bone and Joint Surgery*, 79:857–865, (1997).

[11] R. Fick. *Handbuch der Anatomie und der Mechanik unter Berücksichtigung der bewegenden Muskeln*. Fischer Verlag, Jena, (1904).

[12] H. Gellman A. M. Hollister and R. L. Waters. The relationship of the interosseous membrane to the axis of rotation of the forearm. *Clinical Orthopaedics and Related Research*, 298:272–276, (1994).

[13] J. P. Adams J. B. Christensen, K. O. Cho, and L. Miller. A study of the interosseous distance between the radius and ulna during rotation of the forearm. *The Anatomical Record*, 160(2):261–271, (1968).

[14] Y. Youm, R. F. Dryer, K. Thambyrajah, A. E. Flatt, and B. L. Sprague. Biomechanical analyses of forearm pronation-supination and elbow flexion-extension. *Journal of Biomechanics*, 12(4):245–255, (1979).

[15] K. J. Fischer, T. T. Manson, H. J. Pfaeffle, M. M. Tomaino, and S. L. Woo. A method for measuring joint kinematics designed for accurate registration of kinematic data to models constructed from CT data. *J. Biomech.*, 34:377–383, (2001).

[16] C. G. Hagert. The distal radioulnar joint in relation to the whole forearm. *Clinical Orthopaedics and Related Research*, 275:56–64, (1992).

[17] M. L. Robbin, K. N. An, R. L. Linscheid, and E. L. Ritman. Anatomic and kinematic analysis of the human forearm using high-speed computed tomography. *Med. Biol. Eng. Comput.*, 24(2):164–168, (1986).

[18] F. J. Valero-Cuevas and C. F. Small. Load dependence in carpal kinematics during wrist flexion in vivo. *Clinical Biomechanics (Bristol, Avon)*, 12(3):154–159, (1997).

[19] I. A. Kapandji. *Funktionelle Anatomie der Gelenke*, volume 1. Enke, Stuttgart, (1999).

[20] T. T. Nakamura, Y. Yabe, Y. Horiuchi, and N. Yamazaki. In vivo motion analysis of forearm rotation utilizing magnetic resonance imaging. *Clin.Biomech.*, 14:315–320, (1999).

[21] T. Nakamura, Y. Yabe, and Y. Horiuchi. A biomechanical analysis of pronation-supination of the forearm using magnetic resonance imaging: changes of the interosseous membrane of the forearm during pronation-supination. *Nippon-Seikeigeka-Gakkai-Zasshi*, 68:14–25, (1994).

[22] A. M. Weinberg. *Biomechanische Modellierung der normalen und funktionsgestörten Umwendbewegung des Unterarmes. Habilitationsschrift*. Medizinische Hochschule Hannover. Unfallchirurgische Klinik, (2000).

[23] A. M. Weinberg, I. T. Pietsch, M. B. Helm, J. Hesselbach, and H. Tscherne. A new kinematic model of pro- and supination of the human forearm. *J. Biomechanics*, 33:487–491, (2000).

[24] A. Kecskeméthy and A. Weinberg. An improved elasto-kinematic model of the human forearm for biofidelic medical diagnosis. *Multibody System Dynamics*, 14:1–21, (2005).

[25] K. Nojiri, N. Matsunaga, and S. Kawaji. Modeling of pro-supination for forearm skeleton based on MRI. *Proceedings of the 17th Word Conference, the International Federation of Automatic Control, Seoul(Korea)*, July (6-11):14767–14772, (2008).

[26] S. Miyaguchi, K. Nojiri, N. Matsunaga, and S. Kawaji. Impedance control of pro-supination based on the skeleton model of upper limbs. *International Conference on Control, Automation and Systems*, Oct. (17-20):968–973, (2007).

[27] J. Xu, P. Kasten, A. M. Weinberg, and A. Kecskeméthy. Automated fitting of an elastokinematic surrogate mechanism for forearm motion from MRI measurements. *Advances in Robot Kinematics:Motion in Man and Machine*, 6:349–358, (2010).

[28] P. Furnstahl, A. Schweizer, L. Nagy, G. Szekely, and M. Harders. A morphological approach to the simulation of forearm motion. *Conf proc IEEE Eng Med Biol Soc*, pages 7168–7171, (2009).

[29] S. Miyaguchi, N. Matsunaga, and S. Kawaji. Trajectory generation of CPM device for upper limbs considering constraint caused by joint disorder. *Journal of Robotics and Mechatronics*, 22(2):239–247, (2010).

[30] S. Miyaguchi, N. Matsunaga, and S. Kawaji. Trajectory generation of CPM device for the elbow joint considering constraint caused by joint disorder. *Journal of Robotics and Mechatronics*, 22(2):4283–4288, (2010).

[31] S. Balasubramanian, J. Klein, and E. Burdet. Robot-assisted rehabilitation of hand function. *Current Opinion in Neurology*, 23(6):661–670, (2010).

[32] J. Klein, S. Spencer, J. Allington, J. E. Bobrow, and D. J. Reinkensmeyer. Optimization of a parallel shoulder mechanism to achieve a high-force, low-mass, robotic-arm exoskeleton. *Robotics*, 26(4):710–715, (2010).

[33] K. Holzbaur, W. Murray, and S. Delp. A model of the upper extremity for simulating musculoskeletal surgery and analyzing neuromuscular control. *Ann Biomed Eng*, 33 (6):829–840, (2005).

[34] D. Blana, E. K. Chadwick J. G. Hincapie, and R. F. Kirsch. A musculoskeletal model of the upper extremity for use in the development of neuroprosthetic systems. *J. Biomech.*, 41(8):1714–1721, (2008).

[35] V. Burdin, Ch. Roux, and Ch. Lefevre. Study of 3D human movements: Influence of the forearm bone morphology on the magnitude of the pronosupination motion. *IEEE Workshop on Motion of Non-Rigid and Articulated Objects*, Austin, TX:219–231 vii, (1994).

[36] S. C. Tay, R. A. Berger, K. Tomita, E. T. Tan, K. K. Amrami, and K. N. An. In vivo three dimensional displacement of the distal radioulnar joint during resisted forearm. *Hand Surg.*, 32A:450–458, (2007).

[37] T. E. Fu, G. Li, J. S. Souer, S. Lozano-Calderon, J. H. Herndon, and J. B. Jupiter. Elbow position affects distal radioulnar joint kinematics. *Journal of Hand Srugery.*, 34A:1261–1268, (2009).

[38] H. Moritomo, K. Noda, A. Goto, T. Murase, H. Yoshikawa, and K. Sugamoto. Interosseous membrane of the forearm: Length change of ligaments during forearm rotation. *Journal of Hand Surgery*, 34(4):685–691, (2009).

[39] G. E. Marai, D. H. Laidlaw, C. Demiralp, S. Andrews, C. M. Grimm, and J. J. Crisco. Estimating joint contact areas and ligaments lengths from bone kinematics and surfaces. *IEEE Transactions on Biomedical Engineering*, 51(5):790–799, (2004).

[40] T. Yasutomi, Y. Nakatsuchi, H. Koike, and S. Uchiyama. Mechanism of limitation of pronation/supination of the forearm in geometric models of deformities of the forearm bones. *Chlinical Biomechanics*, 17:456–463, (2002).

[41] http://www-wikipedia.org .

[42] B. F. Morrey, L. J. Askew, and E. Y. Chao. A biomechanical study of normal functional elbow motion. *Journal of Bone and Joint Surgery*, 61(5):872–877, (1981).

[43] B. D. C. Boone and S. P. Azen. Normal range of motion of joints in male subjects. *Journal of Bone and Joint Surgery*, 63(6):756–759, (1979).

[44] W. T. Dempster. *Space requirements of the seated operator : Geometrical, kinematic, and mechanical aspects of the body, with special reference to the limbs*. Air Research and Development Command, U.S. Air Force, (1995).

[45] O. Bottema and B. Roth. *Theoretical kinematics*. Applied Mathematics and Mechanics 24. North-Holland Publishing Company, Oxford, New York, (1970).

[46] A. Kecskeméthy and M. Hiller. Automatic closed-form kinematics-solutions for recursive single-loop chains. *Proceedings of the 22nd Biennal ASME-Mechanisms Conference on Flexible Mechanisms, Dynamics, and Analysis. Scottsdale (USA)*, pages 387–393, (1992).

[47] A. Kecskeméthy. Object-oriented modelling of mechanical systems. In *Kinematics and Dynamics of Multi-Body Systems*, number 360 in CISM Courses and Lectures, pages 217–276, Wien, New York, (1995). Springer-Verlag.

[48] A. Kecskeméthy. M☐BILE 1.3 *User's Guide*. Lehrstuhl für Mechanik, Universität Duisburg-Essen, (1999).

[49] P. C. Lauterbur. Image formation by induced local interactions: Examples of employing nuclear magnetic resonance. *Nature*, 242:190–191, (1973).

[50] The Inventor Mentor: Programming Object-Oriented 3D Graphics with Open Inventor, Release 2. *http://www-evasion.imag.fr*.

[51] Z. Y. Tang, J. Pauli, and A. Kecskeméthy. Automatic identifcation of functional kinematic bone features from MRT segmentation for gait analysis. *Mat.-wiss.u.Werkstofftech*, 40:826–731, (2009).

[52] A. M. Weinberg, I. T. Pietsch, M. Krefft, H. C. Pape, M. van Griensven, M. B. Helm, H. Reilmann, and H. Tscherne. Die Pro- und Supination des Unterarms. *Unfallchirurg*, 104:404–409, (2001).

[53] G. L. Kinzel, A. S. Hall Jr, and B. M. Hillberry. Measurement of the total motion between two body segments I: Analytical development. *Journal of Biomechanics*, 5(1):93–105, (1972).

[54] S. C. Tay, R. V. Riet, T. Kazunari, T. Kazunari, K. K. Amrami, K. N. An, and R. A. Berger. A method for in-vivo kinematic analysis of the forearm. *Biomechanics*, 41:56–62, (2008).

[55] S. C. Tay, R. V. Riet, T. Kazunari, K. K. Amrami, K. N. An, and R. A. Berger. In-vivo kinematic analysis of forearm rotation using helical axis analysis. *Clinical Biomechanics*, 25:655–659, (2010).

[56] D. C. Moore, K. A. Hogan, J. J. Crisco, E. Akelman, M. F. Dasilva, and A. P. Weiss. Three-dimensional in vivo kinematics of the distal radioulnar joint in malunited distal radius fractures. *Journal of Hand Surgery*, 27(2):233–242, (2002).

[57] J. P. Baeyens, F. V. Glabbeek, M. Goossens, J. Gielen, P. V. Roy, and J. P. Clarys. In vivo 3D arthrokinematics of the proximal and distal radioulnar joints during active pronation and supination. *Clinical Biomechanics*, 21:S9–S12, (2006).

[58] M. Lin. *Efficient Collision Detection for Animation and Robotics*. PhD thesis, Universtiy of California, (1993).

[59] M. Lin, D. Manocha, and J. Canny. Fast contact determination in dynamic environments. IEEE Intl. Conf. Robotics & Automation, Los Alamitos, CA: IEEE Press, pages 602–608, (1994).

[60] S. Ho, S. Sarma, and Y. Adachi. Real-time interference analysis between a tool and an environment. *Computer Aided Design*, 33:935–947, (2001).

[61] D. Johnson and E. Cohen. A framework for efficient minimum distance computation. *in Proceeding of IEEE International Conference on Robotics and Automation*, pages 3678–3684, (1998).

[62] J. M. Zhou, E. C. Sherbrooke, and N. Patrikalakis. Computation of stationary points of distance functions. *Engineering with Computers*, 9:231–246, (1993).

[63] A. Limaiem and F. Trochu. Geometric algorithms for the intersection of curves and surfaces. *Computer and Graphics*, 19:391–403, (1995).

[64] M. Lin and D. Manocha. Fast interference detection between geometric models. *The Visual Computer*, 11:542–561, (1995).

[65] L. Piegel and W. Tiller. Parameterization for surface fitting in reverse engineering. *Computer-Aided Geometric Design*, 33:593–603, (2001).

[66] N. Patrikalakis and T. Maekawa. *Shape interrogation for computer aided design and manufacturing*. New York, (2001).

[67] Y. L. Ma, W. T. Hewitt, and M. Turner. A high-performance method for calculating the minimum distance between two 2D and 3D nurbs curves. *Journal of Graphics Tools*, 11(1):37–50, (2006).

[68] P. He, C. Zhang, J. B. Zhou, and Y. L. Ma. Calculating the minimum distance between two nurbs curves. *Computer-Aided Industrial Design & Conceptual Design. IEEE 10th International Conference*, pages 643–648, (2009).

[69] J. Pan, L. J. Zhang, and D. Manocha. Collision-free and smooth trajectory computation in cluttered environments. *Robotics Research*, 31(10):1155–1175, (2012).

[70] K. Höllig. *Finite Element Methods with B-Splines*. Frontiers in Applied Mathematics, Universität Stuttgart, Germany, (2003).

[71] G. E. Farin, P. Bézier, and W. Boehm. *Curves and surfaces for computer-aided geometric design*. 4^{th} edition. Academic Press, San Diego, (1997).

[72] C. de Boor. *A Practical Guide to Splines*. Springer-Verlag, New York, (1997).

[73] C. Blanc and C. Schlick. A spline model designed for the end-user. *ACM Transactions on Graphics*, (1995).

[74] R. T. Farouki, C. Manni, and A. Sestini. A spatial C^2 PH quintic splines. *Curve and Surface Design*, pages 147–156, (2002).

[75] P. Diercks. *Curve and Surface Fitting with Splines*. Clarendon Press, Oxford, (1993).

[76] S. R. Buss. *3D Computer Graphics: A Mathematical Introduction with OpenGL*. Cambridge University Press, (2003).

[77] M. Tändl. *Dynamic Simulation and Design of Roller Coaster Motion*. PhD Thesis, Fortschritt-Berichte VDI, (2009).

[78] W. Boehm. Inserting new knots into B-spline curves. *Computer-Aided Design 12*, pages 199–201, (1980).

[79] http://softsurfer.com/archive/algorithm_0106/algorithm_0106.htm.

[80] A. Sarmiento, E. Ebramzadeh, D. Brys, and R. Tarr. Angular deformities and forearm function. *J. Orthop.*, 10:121–133, (1992).

Der Lebenslauf ist in der Online-Version aus Gründen des Datenschutzes nicht enthalten.